An exploration of isolated vortex collisions

by

Jia Cheng Hu

A thesis
presented to the University of Waterloo
in fulfillment of the
thesis requirement for the degree of
Doctor of Philosophy
in
Mechanical and Mechatronics Engineering

Waterloo, Ontario, Canada, 2021

Examining Committee Membership

The following served on the Examining Committee for this thesis. The decision of the Examining Committee is by majority vote.

External Examiner:	David E. Rival Associate Professor, Dept. of Mechanical and Materials Engineering Queen's University
Supervisor(s):	Sean D. Peterson Professor, Dept. of Mechanical and Mechatronics Engineering University of Waterloo
Internal Member:	Serhiy Yarusevych Professor, Dept. of Mechanical and Mechatronics Engineering University of Waterloo
Internal Member:	Carolyn Ren Professor, Dept. of Mechanical and Mechatronics Engineering University of Waterloo
Internal Member:	Bruce MacVicar Associate Professor, Dept. of Civil and Environmental Engineering University of Waterloo

Author's Declaration

I hereby declare that I am the sole author of this thesis. This is a true copy of the thesis, including any required final revisions, as accepted by my examiners.

I understand that my thesis may be made electronically available to the public.

Abstract

Vortices are ubiquitous in fluid dynamics, and their interactions are critical in various natural and engineering phenomena, such as the turbulence cascade and unsteady fluid loading on structures. This thesis focuses on the collision of isolated vortices to gain insights into the dynamics of vortex-structure and vortex-vortex interactions. Vortex rings are employed as the canonical vortex element in this study, and three main studies were conducted to address different aspect of the isolated vortex collision.

First, the dynamics of a vortex ring advecting towards and interacting with a solid wall with a coaxial aperture is explored. The aperture is an axisymmetric surrogate of a thin plate tip to investigate the partial vortex-structure interaction. When the aperture radius is approximately equal to that of the ring, however, an interesting phenomenon is observed, wherein the hydrodynamic impulse of the vortex ring is enhanced up to an additional 11% at the highest considered Reynolds number when comparing with a free vortex ring that experiences no collision (herein termed the "vortex nozzle" effect). Detailed investigation of the "vortex nozzle" illustrates that the impulse enhancement is a consequence of two complementary effects: (*i*) fluid originating along the impact side of the wall is entrained into the ring, increasing its radius and volume; and (*ii*) the circulation loss during the interaction with the aperture tip is minimized due to the vortex core enveloping the aperture tip.

Second, the mechanism of viscous vortex reconnection is revisited by considering the collision of vortex rings over a range of initial collision angles and Reynolds numbers. While the overall reconnection process is similar to anti-parallel vortex reconnection, we find that collision angle exerts significant influence over the process, altering the evolution of various global and local quantities. The collision angle primarily manipulates the "pyramid" process, but it is short-lived for viscous vortices. The present work shows that the "pyramid" process is arrested by parallelization of the colliding vortices, wherein contact of the colliding vortices halts their motion towards each other at the pyramid apex, allowing the rest of the vortex tube to "catch up", breaking the pyramid structure. Parallelization marks the transition to a second phase of stretching, where the colliding vortices remain parallel. Vorticity amplification from pyramid stretching is significantly stronger than its parallel counterpart and is thus the dominant factor determining reconnection properties. Critically, the Reynolds number scaling for the reconnection rate differs depending on the collision angle, which challenges the conjecture of universal Reynolds number scaling in the literature.

Lastly, the evolution of a strained dipole is explored to under the deformation of vortex cores during the collision of anti-parallel vortices, which is a topic of recent debate in litera-

ture, and contribute to the understand of the turbulent cascade mechanism and possibility of finite-time singularity during anti-parallel vortex collision in inviscid flow. The results have shown that under an imposed strain flow, which mimics the strain experiences during anti-parallel vortex collision, a dipole can not maintain their compactness. Furthermore, the deformation of the vortex cores actually enhances the attract between the cores, which is absent in the theoretical modeling of anti-parallel vortex collision (the "pyramid" process), and supports the idea that parallelization is the primary mechanism that ends the 'pyramid" process.

Acknowledgements

I would like to sincerely acknowledge my advisors, colleagues, faculty members, technicians, and support staff at University of Waterloo. I would also like to deeply thank the committee members for reviewing this thesis work.

Table of Contents

List of Figures

List of Tables

Nomenclature

$\mathcal{A}$ Anti-symmetric rotation-rate tensor. 13

A Area. 23

C_{am} Constant added mass correction. 11, 56

C_v A control volume C_v. 10, 43

E_1^i Initial kinetic energy of the incoming vortex ring. 24

E_1 Hydrodynamic impulse of the incoming vortex ring. 33, 35, 36

E_2 Hydrodynamic impulse of the post-impact outgoing vortex ring from the aperture. 33, 36

E_f Final kinetic energy of the passing vortex ring. 54, 55

E_∞ Kinetic energy of the baseline vortex ring, where the vortex ring advecting through the domain in absence of a wall. 54, 55

$\mathcal{I}$ The complete elliptic integral of the second kind. 135, 136

E_s Total kinetic energy in the system. 36

E Kinetic energy. 10, 21, 23, 33, 54

F_a Reaction force from the aperture wall. xviii, 59–63

$\mathcal{F}$ The incomplete elliptic integral of the first kind. 136, 137

F_{ptp} Peak-to-peak value of the reaction force from the aperture wall. xviii, 63

Γ_1^i Initial circulation of the incoming vortex ring. 24, 25, 33

Γ_1 Circulation of the incoming vortex ring. 33, 35, 36, 38, 135, 136

Γ_2 Circulation of the post-impact outgoing vortex ring from the aperture. 33, 38

Γ_f Final circulation of the passing vortex ring. xvii, xviii, 54, 55, 63, 67

Γ_∞ Circulation of the baseline vortex ring, where the vortex ring advecting through the domain in absence of a wall. 54, 55

Γ_i Initial circulation of the incoming vortex ring. xvi–xviii, 44–46, 48, 49, 51–53, 55–57, 60, 61, 65

$\dot{\Gamma}_m$ Rate of change for circulation on the reconnection plane. xix, 80, 82

Γ_n Negative circulation in the $x < 0$ half-plane. xvii, 49, 50

Γ_o Circulation for vortex core initialization. 45

Γ_p Positive circulation in the $x < 0$ half-plane. xvii, 49, 50

$\dot{\Gamma}_{xy}$ Rate of change for circulation on the cutting plane. 79

Γ_{xy} Circulation on the cutting plane. 79

$\dot{\Gamma}_{xz}$ Rate of change for circulation on the reconnection plane. 80

Γ_{zy} Circulation on the reconnection plane. 79, 80

Γ Circulation. xvii, xviii, xxiii, 10, 21, 23, 24, 33, 43, 54, 58, 62, 66, 67, 71, 75, 92

$\mathcal{H}$ The incomplete elliptic integral of the second kind. 136, 137

I_1^i Initial hydrodynamic impulse of the incoming vortex ring. 24

I_1 Hydrodynamic impulse of the incoming vortex ring. 33

I_2 Hydrodynamic impulse of the post-impact outgoing vortex ring from the aperture. 33, 38

I_a Hydrodynamic impulse applied to the fluid by the aperture. xviii, 61, 62

I_f Final hydrodynamic impulse of the passing vortex ring. xvii, xviii, 53–55, 61, 67

I_∞ Impulse of the baseline vortex ring, where the vortex ring advecting through the domain in absence of a wall. 53–55

I_i Initial hydrodynamic impulse of the vortex ring. 61

I_s Hydrodynamic impulse of the secondary vortices. 61

I Hydrodynamic impulse. 10, 11, 21, 23, 33, 43, 53, 54, 56, 62

J_0 The Bessel function of order one. 135

J_1 The Bessel function of order two. 135

J_m The Bessel function of order m. 135

$\mathcal{K}$ The complete elliptic integral of the first kind. 135, 136

N_r Number of symmetrical aligned vortex rings. 71, 73

Ψ Stokes' stream-function. 23

Q_m Max volumetric flow rate though the aperture. xvii, 59

Q Volumetric flow rate though the aperture. 21, 23, 29, 35, 36, 38, 43, 59

R_1^i Initial radius of the incoming vortex ring. 24, 25, 31, 33, 34

R_1 Radius of the incoming vortex ring. 35, 36, 39, 135–137

R_2 Radius of the post-impact outgoing vortex ring from the aperture. 31, 33

R_a Distance from the aperture wall to the vortex ring. xvi–xviii, 21, 24, 33–36, 38, 39, 42–45, 47–67, 135, 136

R_{c1}^i Initial core radius of the incoming vortex ring. 24

R_{c1} Core radius of the incoming vortex ring. 34–36

R_c Core radius of a vortex ring. xx, 10, 21, 45, 54, 71, 73, 91–93

Re Circulation based Reynolds number. xvi–xxi, xxiii, 24, 44–68, 71, 73, 75, 76, 78–87, 89, 90, 93–95, 140

R_f Final radius of the passing vortex ring. xvii, xviii, 54, 55, 67

R_∞ Radius of the baseline vortex ring, where the vortex ring advecting through the domain in absence of a wall. 54

R_i Initial radius of the incoming vortex ring. xvi–xviii, 44–67

R_o Radial position for vortex core initialization. 45

R Radius of a vortex ring. xvii, xviii, xxiii, 10, 21, 43, 54, 58, 62, 66, 67, 71, 73–75

$\mathcal{S}$ Symmetric strain-rate tensor. 13

U_1 Total advection velocity (x-component) of the incoming vortex ring. 35

U_a Aperture induced advection velocity (x-component) of the incoming vortex ring. 35, 136

U_f Final convective velocity of the passing vortex ring. 56

U_∞ Convective velocity of the baseline vortex ring, where the vortex ring advecting through the domain in absence of a wall. 56

U_s The self-induced velocity of a vortex ring. 10, 11, 35, 56

U_w Wall induced advection velocity (x-component) of the incoming vortex ring. 35, 135

V_1 Total Radial advection velocity (r-component) of the incoming vortex ring. 35

V_a Aperture induced radial advection velocity (r-component) of the incoming vortex ring. 35, 136

$\mathcal{V}_f$ Final volume of the passing vortex ring. xvii, 56

$\mathcal{V}$ Volume of the vortex ring. 11, 55, 56

V_w Wall induced radial advection velocity (r-component) of the incoming vortex ring. 35, 135

α_{lim} Limiting dimensionless energy of a vortex ring. 33, 34, 37, 38

α Dimensionless energy of a vortex ring. 33, 37, 38

θ Collision angle between the approach vortex rings. xviii–xx, 71–81, 83–87, 89–91, 93–95

Δp The pressure difference across the wall. 43, 61

Ω Enstrophy (Chapter 4). 77

Ω_p Cutting plane Peak enstrophy value (Chapter 4). xix, 77, 78

$\mathcal{E}_p$ Peak enstrophy value (Chapter 3). xviii, 64

Ω_p Total enstrophy (Chapter 4). xix, 77, 78

$\mathcal{E}$ Enstrophy (Chapter 3). 64

η A variable used for the analytical model of the ring-aperture interaction. 135, 136

k_{xz} Curvature of the peak vorticity line projected on to the reconnection plane. 85, 86

k_{yz} Curvature of the peak vorticity line projected on to the top plane. 85, 86

k Peak vorticity line curvature. xx, 83, 90

λ_2 A criterion for vortex identification. 13, 22

l Peak vorticity arc length. xx, 83, 84, 90

$|\boldsymbol{\omega}|$ Peak vorticity magnitude. xx, 90

$|\boldsymbol{\omega}|$ Vorticity vector magnitudes. xviii–xxi, 73, 76, 81, 85, 87, 95, 140

μ A variable used for the analytical model of the ring-aperture interaction. 136, 137

ν Kinematic viscosity. 9, 13, 14, 24, 44, 71, 74, 77

∂C_v Boundary of a control volume C_v. 10, 43

ϕ_- The potential field in the $x < 0$ half-space (in front of the aperture). 34, 35

ϕ_a The potential field of the aperture opening. 34, 135

ϕ_v The potential field of the incoming vortex ring. 34, 135

ϕ_w The potential field of the aperture wall. 34, 135

PIV Particle image velocimetry. 22–24, 29, 31

ψ Stream-function. 23

p Pressure. 9, 13, 14, 45

ρ Fluid density. 9–11, 13, 14, 23, 25, 33

σ A variable used for the analytical model of the ring-aperture interaction. 35, 136

s Separation distance between the vortex cores. xviii–xx, 72, 73, 89, 91, 92

t_f The time of which the final properties of the vortex rings are given. xvii, 44, 56, 57, 61

$\widetilde{u}$ Averaged aperture velocity profile. 23

u Velocity component (x) of either cylindrical or Cartesian coordinate systems. 22, 23

$\boldsymbol{k}$ Spectral space vectors. 14, 15, 74

γ Peak vorticity line position vectors. 83

$\boldsymbol{n}$ Boundary normal unit vectors. 10, 43

$\boldsymbol{u}$ Velocity vectors. 9, 10, 14, 15, 17, 42, 43, 45, 74

$\boldsymbol{\omega}$ Vorticity vectors. 9, 10, 14, 15, 43, 74, 77, 79

$\boldsymbol{x}$ Position vectors. 10, 14, 17, 43, 77

ω_θ Azimuthal vorticity field. 22, 23, 43, 45, 49, 64, 91, 92

ω_p Peak vorticity value at the center of the vortex core. 91, 92

ω Vorticity. 77

v Velocity component of either cylindrical (r) or Cartesian coordinate (y) systems. 22

x^+ Vertical plane located immediately downstream of the aperture. 23

x^- Vertical plane located immediately upstream of the aperture. 23

ξ Distance from the aperture wall to the incoming vortex ring. 35, 36

ξ Distance from the aperture wall to the vortex ring. 21, 35, 135–137

x_o Horizontal position for vortex core initialization. 45

x_p Peak vorticity position within a vortex core. xix, xx, 87, 90, 93, 94

Chapter 1

Introduction

Vortices, as described by Prof. Küchemann, are the "sinews and muscles of fluid motion" [50]. Their interactions arise in various fundamental and applied fluid phenomena, including the turbulent cascade, locomotion of aquatic animals, and unsteady structural loading to name a few. With the aid of modern investigation techniques such as particle imaging velocimetry and high performance computing, the field of vortex dynamics is evolving at a rapid pace. In this thesis, the dynamics of vortex collisions are considered to gain fundamental insights into the processes involved in vortex-structure and vortex-vortex interactions.

The interactions of vortices with solid surfaces have been explored extensively using vortex rings. The collision of a vortex ring with a surface is a dynamically rich canonical flow that has been used in a variety of vortex dynamics investigations. Walker *et al.* [101] examined a vortex ring impinging normally on a flat wall as a controlled laboratory experiment to investigate the bursting mechanism of turbulent boundary layers, wherein eruptions transfer near-wall vorticity to the outer layer. They found that the boundary layer, induced by the approaching ring, separates at the outer extent of the colliding vortex ring due to the resulting adverse pressure gradient. The separated shear layer rolls into a secondary ring, which couples with the colliding ring to rebound away from the wall, moving the boundary layer vorticity into the outer flow. By analogy, Walker *et al.*[101] proposed the sequence of unsteady separation and vortex rebound as a plausible physical mechanism behind turbulent boundary layer bursting phenomena.

Swearingen *et al.* [95] performed spectral simulations and stability analysis on the vortex ring-wall interaction. They determined that the secondary vortex ring ejected from the boundary layer is unstable under the strain field of the primary vortex ring, which

leads to turbulent transition. Verzicco and Orlandi [99] examined the collision of a vortex ring with an inclined flat wall to investigate the role of differential stretching, finding that a high-pressure region forms in the leeward side of the ring due to high strain from stretching, which creates a pressure gradient that drives vorticity to the windward side. Recently, New *et al.* [72] investigated the head-on collision of a vortex ring with a V-wall, and observed that the additional constraints imposed by the V-wall introduces complex three-dimensional vortex dynamics in comparison to a single inclined plane. New and Zhang [73] examined the head-on collision of a vortex ring with a cylinder to elucidate the vortex dynamics near arbitrarily contoured boundaries, noting that the strong interactions between the primary and secondary vortex rings due to the curvature lead to the ejection of smaller ringlets. In addition to the aforementioned studies with solid boundaries, vortex interactions with other interfaces, including free surfaces [4], granular surfaces [52], porous surfaces [69, 105], and stratified interfaces [78, 79] have been explored.

The dynamics of a vortex impacting the edge of a finite length plate are further complicated by vorticity generated and shed from the plate tip. Potential flow analysis of point vortices interacting with a finite length plate predicts very high (singular) bounded vorticity at the plate tip, which sharply influences local vortex trajectories [82, 1, 75]. Peterson and Porfiri [83] examined a vortex dipole colliding with a thin semi-infinite plate in a viscous fluid, wherein the dipole axis of symmetry aligned directly with the plate tip. They found in this configuration that the dipole splits in two upon impact with the plate, with the two dipole halves then coupling with secondary boundary layer vorticity and vorticity shed from the plate tip to form two new secondary dipoles that followed curved trajectories away from the plate. Zivkov *et al.* [112] replaced the semi-infinite plate with a flexible plate and detailed the resulting changes in shed vorticity, which impacted the secondary dipole trajectories. In these studies, the vortex cores remained relatively undisturbed during the plate interaction by virtue of the initial vortex/plate alignment. The dynamics of a direct collision of a viscous vortex core with a thin plate edge, however, remains relatively unexplored.

In the case of vortex-vortex interactions, the collision of vortices in a viscous fluid can result in vortex reconnection, which is the only known mechanism in incompressible flow that alters the topology of vortices. It also plays a critical role in turbulence [39], including the energy cascade [106] and noise generation [21]. Hence, there is vast literature on the topic of viscous vortex reconnection under various conditions, including anti-parallel vortex tubes [42, 39, 53], orthogonal vortex tubes [111, 7], vortex rings [47, 46], and anti-parallel vortex tubes with axial flow [54].

Vortex stretching is part of the vortex reconnection; it amplifies vorticity within the colliding vortices, resulting in steeper gradients that accelerate viscous cross-diffusion for

reconnection. Recently, Moffatt and Kimura theoretically predicted a "pyramid" stretching mechanism for the inviscid interaction of anti-parallel vortices [62, 63] (see Figure 1.1). Pyramid stretching, as the name implies, is based on the formation of a pyramid structure

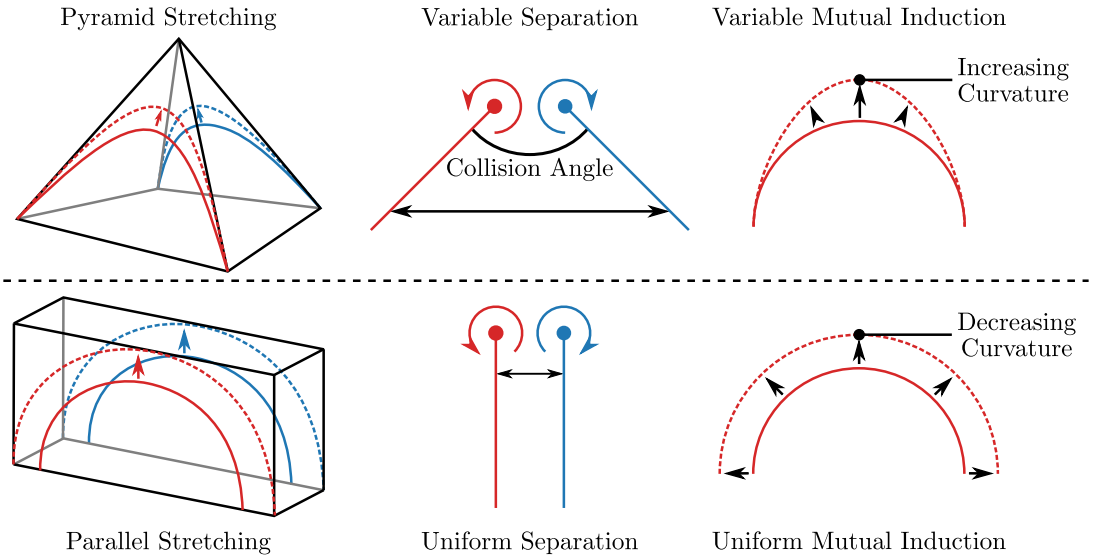

Figure 1.1: Summary of the pyramid (top) and parallel (bottom) stretching.

during the interaction, which is well known from vortex filament (Biot-Savart) studies of vortex collisions in ideal and quantum fluids [22]. Pyramid formation is driven by non-uniformity in the mutual induction between filaments (proportional to separation distance), which disproportionately draws together the colliding vortices in the middle, forming the pyramid shape. Moffatt and Kimura revisited the pyramid process by incorporating vortex stretching into the Biot-Savart model [62, 63]. They discovered that the pyramid formation produces localized stretching at the apex, which increases both the curvature and vorticity. The onset of pyramid stretching in a viscous fluid was subsequently confirmed by numerical simulations [107], where the signatures of pyramid stretching (vorticity amplification coupled with curvature gain) were clearly observed, but very short-lived.

Both the analytical models [62, 63] and numerical simulations [107] employed slender vortex cores, where the core radius is orders of magnitude smaller than the local spanwise curvature, such that vortex motions are governed by the Biot-Savart law. However, for moderate Reynolds numbers, the slender core assumption becomes strained, as viscous diffusion will rapidly expand the core radii during their approach. The difference in the separation scaling during the approach between slender [107, 108] and thick [39] core vortex

reconnection raises the question of whether the pyramid stretching still exists for thick-core vortices.

There is also the question of the influence of collision angle on the reconnection process. Considering the limiting case of zero collision angle where the colliding vortices are parallel to each other (see Figure 1.1, the uniform mutual induction moves the vortices radially outward, producing an overall spanwise stretching that decreases the curvature [18]. The behavior of this "parallel" stretching is in stark contrast with the pyramid stretching (local vs. overall stretching, increase vs. decrease in curvature). Varying collision angle essentially modifies the uniformity of the mutual induction (proportional to separation distance) between the vortices (see Figure 1.1), creating a spectrum of vortex stretching conditions. At high angles, strong pyramid stretching and a weak parallel stretching is expected, and vise versa for low angles. Hence, a shift in the stretching characteristics is expected as collision angle varies, which may lead to changes in vorticity amplification, and thus the reconnection process.

To the best of our knowledge, the only numerical study that examined the role of the collision angle by means of colliding two vortex rings together at various angles was Kida *et al.* [46]. They reported a change in the reconnection completeness, and attributed it to the influence of secondary motions from the rest of the vortex ring; however, the change in stretching characteristics was not considered. There is no relevant discussion on the pyramid stretching, because it was yet to be discovered at the time. The maximum vorticity evolution from the same study shows no major changes with respect to the collision angle. However, the computational capabilities at the time (64^3 collection points) were limited in comparison with modern computers. The grid size was only about half of the initial core radius, which is unlikely to resolve the stretched vortices upon collision, and thus potentially masking the details.

A particular assumption in the analytical model of Moffatt and Kimura [62, 63] has been a source of controversy recently. The conjecture states that colliding vortex cores remain compact if the core size is sufficiently small, and this conjecture is based on the analysis of vortex monopole.

The vortex monopole/column is the fundamental element of vortex dynamics. It has been studied extensively to elucidate the behaviours of coherent vortices in turbulence, such as the famous Burgers vortex problem that highlights the underlying mechanism of vortex stretching in turbulent flows [12]. An extension to Burgers vortex is the deformation of a vortex core in a non-axisymmetrical strain flow. The problem was first investigated by Kida [43] with a planar irrotational strain field, where the principal strain axes were perpendicular to the vortex axis. The vortex motion was found to bifurcate into two

categories depending on the strain-to-vorticity ratio. Weak strain results in an elliptical vortex that nutates around its center, while strong strain simply flattens the vortex into a sheet. A follow up study by Neu [70] incorporated axial stretching into the analytical model. He found that the added stretching component does not change the general bifurcation behaviour, but only delays the critical bifurcation point to a higher strain-to-vorticity ratio. That is, strong axial stretching would prevent flattening of the vortex core in an irrotational strain field. Subsequently, Moffatt and Kimura [61] generalized the motion of a vortex column in an uniform non-axisymmetric irrotational strain using large Reynolds number asymptotic theory. They showed that strained vortices under stretching can survive for a long time, consistent with the observed persistence of vortex filaments in turbulent flows.

While the analysis of a single strain vortex column provided compelling theories on the vortex dynamics of turbulent flows, recent surveys of turbulence have shown the tendency of forming anti-parallel vortex pairs [32, 68]. McKeown *et al.* [55] experimentally observed the iterative process of a colliding anti-parallel vortices, where the vortices are flattened into thin vortex sheets, then re-rolled into smaller anti-parallel vortices under instability, which in turn, collide again. Based on their observation, they have proposed that the turbulent cascade is achieved though such an iterative flattening process between the vortex pairs. An elemental analysis of the iterative flattening process by Brenner *et al.* [8] suggested the possibility of finite-time singularity for inviscid flow. However, a subsequent theoretical analysis by Moffatt and Kimura [62] have found that the mutually-induced strain from the pairing vortices is insufficient to flatten the cores. Their model, based on the vortex monopole model with the strain field from the pairing vortices extracted using Biot-Savart law, have shown that if the vortex is sufficiently small, the cores will maintain their compactness. As such, the finite-time singularity can not be achieved by the iterative flattening process. Rather, they proposed that the pyramid process (see Chapter 5) is the potential path towards finite-time singularity in inviscid flow, since the cores are able to maintain compactness at small scales. However, a follow-up numerical simulation by Yao and Hussain [107], disputed the claim of Moffatt and Kimura [62], as they still observed core flattening in an analogous collision of anti-parallel vortices within the core size limit suggested by Moffatt and Kimura [62]. But then, a similar follow-up numerical study by McKeown *et al.* [56] found no core flattening between vortex pairs.

Clearly, there is a disconnect between the applied and theoretical understanding of the core flattening process of an anti-parallel vortex pair, with the experimental [55] and the numerical [107] studies show a clear sign of core flattening, but the theoretical model [62] and a different simulation [56] found compact vortex cores. Is there any compelling theory to explain the flattening process between colliding anti-parallel vortices and bridge

the gaps between these studies? Herein it is proposed that there are two components that were overlooked, namely, the curvature induced strain, and the applicability of the strained vortex monopole model to the anti-parallel vortex pairs.

The curvature-induced strain between a pair of anti-parallel vortices is only briefly documented once in the literature in the late 80s. Pumir and Kerr [86] found that the flattening of the vortex cores, which they refereed as ribbons, only occurs if the anti-parallel vortex tubes are curved. This explains the differences between the two numerical simulations, where Yao and Hussain [107] employed curved tubes, while McKeown *et al.* [56] employed straight tubes. This additional component of strain was neglected in the theoretical analysis by Brenner *et al.* [8], and Moffatt and Kimura [62]. While the strain from the pairing vortex is insufficient to flatten a vortex core at small scales, the effect of the curvature induced strain have yet to be considered.

With regards to the applicability of the vortex monopole model to the anti-parallel vortex pairs, the collision of anti-parallel vortices are known to produced the so-called head-tail structure, which consists of a leading vortex dipole followed by a vorticity tail [45, 39]. While the tail can be viewed as a partially flattened vortex core, it is actually the result of the external strain field forcing the leading dipole to eject vorticity into its wake [46, 98]. That is, the behaviour of a strain vortex dipole does not fall into either maintain compactness nor flattening category, but somewhere in between. The drastic differences in the behaviours suggest a fundamental change in the dynamics as a result of the coupling between the pairing vortices, hence the employment of the vortex monopole model in the interpolation of the behaviours are questionable. Is the flattening observed in the experimental study of McKeown *et al.* [55] merely the formation of head-tail structure? Could an anti-parallel vortex pair be truly flattened like a monopole?

The evolution of a strained vortex dipole is a relatively unexplored topic in the literature, with only three relevant articles found during a rigorous literature review. Evidence of the head-tail formation for a strained dipole is first reported by Buntine and Pullin [11]. Subsequently, Kida *et al.* [46] improved the initial conditions of the simulations by employing a Lamb dipole, and tested a small range of strain-to-vorticity ratios. They observed that the relative size of the head and tail strongly depends on this ratio. [98] is an experimental study that validated the simulation results. These studies are limited to low Reynolds numbers, where the dynamics are dominated by viscous effects, which is well known to produce the same head-tail structure [46, 23]. As such, the present understanding of the role of strain flow on vortex dipole dynamics is heavily obscured by viscous effects, and unsuitable for the analysis of high Reynolds number turbulent flows and the finite-time singularity of Euler's equation. Furthermore, the range of strain-to-vorticity ratio, as well as the type of strain (planar only), are limited is these studies, which lack any scenarios

that includes the axial stretching.

1.1 Objectives

Though isolated vortices are less common in nature than, say, the wide range of coherent structures evident in turbulent flows, studying such idealized vortex dynamics allows the systematic probing of phenomenon that can inform the role of a particular vortex motion as part of a larger and more complex flow evolution. Examples of such investigations include the recent experimentation with twisted and knotted vortex rings to examine the effects of vortex reconnection on the conservation of various topological quantities in real fluids [49]. This approach provides a controlled and simplified way to study vortex dynamics. Therefore, herein we opt to examine the interaction of isolated vortices to explore relevant fundamental questions in vortex-vortex and vortex-solid interactions. Particularly, vortex rings are employed extensively as the idealized medium for our studies.

The objectives of this thesis are:

- Investigate the collision between a vortex ring and co-axial aperture to determine the optimal placement of the structural tip with respect to the colliding vortices to maximize the unsteady fluid loading exerted on the structure. The aperture emulates the tip of flat plate, and the co-axial alignment eliminates any undesirable three-dimensional effects to examine the fundamental dynamics of the interaction.

- Examine the role of collision angle over the performance vortex reconnection. The collision angle is hypothesized that the collision angle between vortices is a determining factor that controls the "pyramid" process, which has the potential to accelerate the viscous diffusion process during reconnection.

- Test Moffatt and Kimura's assumption of compact vortex cores during an inviscid vortex collision by investigating the evolution of a vortex dipole in an inviscid fluid subject to an independent irrotational strain field.

This thesis comprises three main studies to address the listed objectives. The first study, associated with Objective 1, explores the interaction of a vortex with the thin plate tip. In Chapter 3, preliminary experimental results, including flow visualization and particle image velocimetry, are presented. Chapter 4 explores the problem further via a two-dimensional numerical study for a greater range of aperture tip positions relative to the vortex core. The second study, addressing Objective 2, employs a high performance pseudo-spectral code

to examine the role of collision angle during viscous vortex reconnection in Chapter 5. The final study, addressing Objective 3, examines the evolution of a strain vortex dipole analogous to the vortex evolution at the apex of the pyramid during anti-parallel vortex collision, with contour dynamics.

Chapter 2

Background

This chapter includes and introduction to vortex dynamics and relevant quantitative assessment metrics, as well as background on the analysis tools employed in the numerical studies.

2.1 Vorticity transport equation

Vorticity ($\boldsymbol{\omega}$) is the spin vector of the local fluid parcel. Mathematically, vorticity can be obtained from the curl of the velocity as $\boldsymbol{\omega} = \nabla \times \boldsymbol{u}$. By taking the curl the incompressible Navier-Stokes equations

$$\frac{\mathrm{D}\boldsymbol{u}}{\mathrm{D}t} = -\frac{1}{\rho}\nabla p + \nu\nabla^2\boldsymbol{u} \tag{2.1a}$$

$$0 = \nabla \cdot \boldsymbol{u} \tag{2.1b}$$

we obtain the incompressible vorticity transport equation,

$$\frac{\mathrm{D}\boldsymbol{\omega}}{\mathrm{D}t} = (\boldsymbol{\omega} \cdot \nabla)\boldsymbol{u} + \nu\nabla^2\boldsymbol{\omega} \tag{2.2}$$

which governs the motion of vorticity. Note, $\mathrm{D}/\mathrm{D}t$, p, ρ and ν are the material derivative, density, pressure and viscosity, respectively. The first term on the right side is the vortex stretching term, and the second term is the diffusion term. The latter is responsible for vortex reconnection by cross-diffusion, as well as the production of vorticity at the boundary.

2.2 Hydrodynamic impulse

The momentum of vortices is difficult to compute direction from a velocity field, because the induced velocity from the vortices extend to infinity and overlap each other. Hence, an alternative formulation is required for the estimation of the momentum of vortices. The alternative formulation can be derived by taking the derivative moment transformation of the momentum integral [104], which yields

$$\int_{C_v} \boldsymbol{u} \, \mathrm{d}V = \frac{1}{2} \int_{C_v} \boldsymbol{x} \times \boldsymbol{\omega} \, \mathrm{d}V - \frac{1}{2} \int_{\partial C_v} \boldsymbol{x} \times (\boldsymbol{n} \times \boldsymbol{u}) \, \mathrm{d}S \tag{2.3}$$

where $\boldsymbol{x}$ and $\boldsymbol{n}$ are position and boundary normal unit vectors , and ∂C_v is the boundary of the control volume C_v. The first term of the right hand side is known as the hydrodynamic impulse, which is equivalent to the momentum of the vortices, while the second term is the boundary flux, which also captures the irrotational effect (add mass).

2.3 Vortex rings

Vortex rings are common phenomena where the vortex lines form a circular closed loop. It is easy to generate and model, and hence is chosen as the primary target of investigation of this thesis. Its properties can be estimated with the following expressions (first order accurate, valid for small cores)

$$I = \pi \rho \Gamma R^2 \tag{2.4a}$$

$$E = \frac{1}{2} \rho \Gamma^2 R \left(\ln \frac{8R}{R_c} - \alpha \right) \tag{2.4b}$$

where Γ, R, and R_c are the circulation, ring radius and core radius of the vortex ring. The core parameter α is determined by the choice of vortex core model (i.e. $\alpha = 2.04$ for viscous core and $\alpha = 1.615$ for quantized core) [94]. The self-induced velocity of the vortex ring can be obtained by Hamilton's equation

$$U_s = \frac{\partial E}{\partial I} = \frac{\Gamma}{4\pi R} \left(\ln \frac{8R}{R_c} - \alpha + 1 \right). \tag{2.4c}$$

The impulse and energy of the vortex ring is directly associated with the entrained fluid within the vortex ring, which can be seen in the cross-sectional view in Figure 2.1,

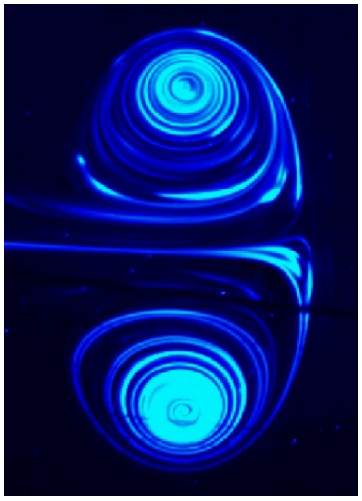

Figure 2.1: Cross-sectional flow visualization of a vortex ring.

where dye is collected within the elliptical-like vortex "bubble". As such, the impulse of the vortex ring can be rewritten as $I = \rho(1+C_{am})\mathcal{V}\, U_s$, where $\mathcal{V}$ is the volume of the vortex "bubble". Attention is needed for the added mass correction parameter C_{am} [19, 94, 96]. For a submerged solid structure, the added mass is the added inertia from surrounding fluid that is displaced by the body motion, and it can be estimated from the second term of the Equation (2.3). The same applies for fluid vortices, as the entrained fluid within the vortex "bubble" also displaces ambient fluid as it travels. As such, the added mass correction must be consider, which for vortex ring, the value is approximately $C_{am} \approx 0.72$.

2.4 Pyramid model of anti-parallel collision

This section briefly reviews the analytical model developed by Moffatt and Kimura [62] for the collision of anti-parallel vortices in inviscid flow. It has been well-known that colliding vortex filaments under Biot-Savart induction form a "pyramid" as shown in Figure 2.2 regardless of initial condition [22]. The dynamical model of Moffatt and Kimura [62] is based on such "pyramid" formation during the collision of two vortex rings.

A plethora of assumptions are made in order to derive the analytical expression. They assumed that the interaction is predominately local, such that behaviour is primarily dominated by the separation $s(t)$, curvature $\kappa(t)$, and core size $\delta(t)$ at the pyramid apex. They also assumed that the "circle-of-curvature" applies to both self- and mutually induced ve-

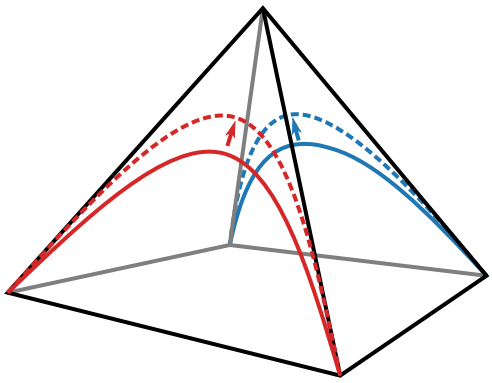

Figure 2.2: Schematics of the pyramid formation of anti-parallel colliding vortex filaments.

locity. This means that the mutually induced velocity can be approximated by the induced velocity of a circular vortex ring as the pyramid formation is localized. It also means that the apex of the pyramid is circular, such that the self-induced velocity can be approximated by the vortex ring velocity shown in Equation (2.4c) with minor correction (this is a common approach to desingularize the Biot-Savart integral). Another assumption is the compactness of the vortex core, where it remains circular at all times (we challenge the validity of this assumption in Chapter 6 since it is based on vortex monopole analysis). Then, further asymptotic analysis revealed the following third-order dynamical system to describe the tip motion of the pyramid

$$\frac{\mathrm{d}s}{\mathrm{d}t} = -\frac{\kappa\cos\theta}{4\pi}\left[\ln\left(\frac{s}{\delta}\right) + \beta\right] \tag{2.5a}$$

$$\frac{\mathrm{d}\kappa}{\mathrm{d}t} = \frac{\kappa\cos\theta\sin\theta}{4\pi s^2} \tag{2.5b}$$

$$\frac{\mathrm{d}\delta^2}{\mathrm{d}t} = -\frac{\kappa\cos\theta}{4\pi s} \tag{2.5c}$$

where $\theta = \pi/4$ is the collision angle. The system of equations describe a positive feedback system, where the curvature-induced self-convective drives the colliding vortices together (Equation (2.5b)), while the decrease in separation distance amplifies the curvature due to the upward motion of the pyramid apex (Equation (2.5b)). The last differential equation captures the core size, which decreases due to stretching, further aiding the self-induced motion that bring the colliding vortices together.

The analytical model is significant for two reasons. First, the numerical results of the model exhibits Leray-scaling, hinting the possibility of Biot–Savart finite-time singularity

of such interaction. Second, the incorporation of the stretching mechanism discovered a violent localized vorticity amplification, and its impact in viscous fluid for vortex reconnection is explored in Chapter 5.

2.5 Vortex identification

Coherent vortices are distinct features in a fluid flow and a major focus of this thesis. However, the definition of a vortex is not simple nor unique. In this section, we will briefly discuss how vortices are identified. Specifically, we will discuss the λ_2 vortex criterion, which we employ in Chapter 3 to track the kinematics of vortices.

Loosely speaking, a vortex is a concentrated region of vorticity where the fluid parcels revolve around a common center. While the definition appears to be similar to vorticity, a region of vorticity is not necessarily a vortex; for example, a shear layer is a distinct region of vorticity that is qualitatively different from a vortex. Therefore, the criteria of vorticity is insufficient for vortex identification.

The λ_2 vortex criterion, proposed by Jeong and Hussain [41], is a popular quantitative vortex identification method. It is based on the assumption that a vortex has a pressure minimum in its center to maintain the orbits of the fluid parcels. To obtain the information on the pressure minimum, the pressure Hessian, a square matrix of second-order partial derivatives of the pressure field, is employed. The pressure Hessian can be directly obtained by taking the symmetrical component of the gradient of the Naiver-Stokes equations (also known as the strain-rate transport equation) as follows,

$$\frac{1}{\rho}\frac{\partial^2 p}{\partial x_i \partial x_j} = \frac{\mathrm{D}\mathcal{S}_{ij}}{\mathrm{D}t} - \nu\frac{\partial^2 \mathcal{S}_{ij}}{\partial x_k^2} + \mathcal{S}_{ik}\mathcal{S}_{kj} + \mathcal{A}_{ik}\mathcal{A}_{kj} \tag{2.6}$$

where $\mathcal{S}$ and $\mathcal{A}$ are the symmetrical and anti-symmetrical components of the velocity gradient tensor. Furthermore, the first and second terms in the above strain-rate transport equation are the effects of the unsteady irrotational strain and viscous diffusion, which are unrelated to the motion of vortices. Thus, they can be safely removed, resulting in the simplified pressure Hessian as $\mathcal{S}^2 + \mathcal{A}^2$. The λ_2 vortex criterion assumes that the cross-section of a vortex has a convex pressure field, hence requiring at least two negative eigenvalues from the Hessian matrix. This is equivalent to requiring the second eigenvalue, λ_2 ($\lambda_1 \geq \lambda_2 \geq \lambda_3$), to be negative, hence the name λ_2 vortex criterion.

The λ_2 vortex criterion is not perfect, hence the existence of over thirty alternative methods in the literature [26]. The primary shortcoming is the fundamentally flawed

assumption of the pressure minimum in the vortex core, which does not consider the longitudinal pressure variation over a vortex tube. As such, it does not provide much useful information in some situations, such as homogeneous turbulence [44]. However, for the its application in Chapter 3, it is more than sufficient due to the near axis-symmetrical nature of the flow, which lacks pressure variation along the vortices.

2.6 Pseudo-spectral method

In this section, the pseudo-spectral method employed for the direct numerical simulation of the Navier-Stokes equation is briefly reviewed. Spectral methods [15, 97, 66] are global methods, wherein computed values at any point in the domain are obtained from information from the entire domain; as such, the solution convergence is exponential. Furthermore, it is free of numerical diffusion and dispersion, making it an attractive numerical method for vortex dynamics, particularly vortex reconnection studies, which often require long-time high-resolution simulations.

To obtain the expression of Naiver-Stokes equation employed for the pseudo-spectral method [66], we first define a smooth velocity vector field in a triple periodic domain as $\boldsymbol{u}(\boldsymbol{x}, t)$, where $\boldsymbol{x}$ is the physical mesh. The velocity vector fields can be transferred between the physical and spectral domains via the discrete Fourier transform as $\boldsymbol{u}_{\boldsymbol{k}}(t) = \mathcal{F}[\boldsymbol{u}(\boldsymbol{x}, t)]$, where $\boldsymbol{u}_{\boldsymbol{k}}$ is the Fourier coefficient at wave-number $\boldsymbol{k}$. The entire Navier-Stokes equations in Equation (2.1) can be Fourier transformed into the spectral domain as

$$\frac{\mathrm{d}\boldsymbol{u}_{\boldsymbol{k}}}{\mathrm{d}t} - (\boldsymbol{u} \times \boldsymbol{\omega})_{\boldsymbol{k}} = -i\boldsymbol{k}P_{\boldsymbol{k}} - \nu|\boldsymbol{k}|^2 \tag{2.7a}$$

$$i\boldsymbol{k} \cdot \boldsymbol{u}_{\boldsymbol{k}} = 0 \tag{2.7b}$$

where $P = p/\rho + \boldsymbol{u} \cdot \boldsymbol{u}/2$ is the modified pressure in the physical space, and $i = \sqrt{-1}$.

The pressure term can be eliminated by the pressure Poisson equation, which is obtained by taking the divergence of the Navier-Stokes equation. In spectral space, the incompressible pressure Poisson equation is

$$P_{\boldsymbol{k}} = -\frac{i\boldsymbol{k} \cdot (\boldsymbol{u} \times \boldsymbol{\omega})_{\boldsymbol{k}}}{|\boldsymbol{k}|^2}. \tag{2.8}$$

By substituting the above pressure Poisson equation into the spectral Navier-Stokes equation, the final expression employed for the pseudo-spectral method is obtained,

$$\frac{\mathrm{d}\boldsymbol{u}_{\boldsymbol{k}}}{\mathrm{d}t} = (\boldsymbol{u} \times \boldsymbol{\omega})_{\boldsymbol{k}} - \nu|\boldsymbol{k}|^2\boldsymbol{u}_{\boldsymbol{k}} - \boldsymbol{k}\frac{\boldsymbol{k} \cdot (\boldsymbol{u} \times \boldsymbol{\omega})_{\boldsymbol{k}}}{|\boldsymbol{k}|^2}. \tag{2.9}$$

The right hand side of Equation (2.9) is easy to compute as it contains only rudimentary arithmetics, except for the non-linear term $(\boldsymbol{u} \times \boldsymbol{\omega})_{\boldsymbol{k}}$, which involves a convolution, a computationally expensive procedure ($O(N^2)$, where N is the number of grid points). Therefore, it is much cheaper to perform an inverse discrete Fourier transform ($O(N \log N)$ with the fast Fourier transform algorithm) and compute the cross product in the physical space then transfer back to spectral space, hence the label "pseudo".

Regards to the implementation of the codes, rudimentary arithmetics are optimized and multi-threaded with the LLVM Just-in-time compiler using the library `numba`, while the parallel fast Fourier transform is computed using `MPI FFTW`. The compact third-order Runge-Kutta scheme is implemented for time integration due to its efficient memory usage [102].

2.7 Contour dynamics

Contour dynamics is a Lagrangian computational method for the two-dimensional motion of vortex boundaries in an incompressible and inviscid fluid, which we employed for the strain dipole investigation in Chapter 6. In this section, the derivation and implementation of the contour dynamics [110] is briefly reviewed.

Consider a vortex patch with total area $\mathcal{A}$ bounded by contour $\mathcal{C}$, which contains a collection of discrete vortices at locations (x_i, y_i) with vorticity ω_i, where i is the number of each discrete vortex, as shown in Figure 2.3. The velocity at any point can be obtained by summing all contribution of the discrete vortices as

$$u(x,y) = -\frac{1}{2\pi} \sum_{i=1}^{N} \frac{y - y_i}{(x - x_i)^2 + (y - y_i)^2} \, \omega_i \, \delta A_i \tag{2.10a}$$

$$v(x,y) = +\frac{1}{2\pi} \sum_{i=1}^{N} \frac{x - x_i}{(x - x_i)^2 + (y - y_i)^2} \, \omega_i \, \delta A_i \tag{2.10b}$$

where δA_i is the infinitesimal area of vortex i. As the number of parcels, N, tends to infinity, the sums reduce to area integrals, yielding the integral representation of the velocity as

$$u(x,y) = -\frac{1}{2\pi} \iint_{\mathcal{A}} \frac{y - y'}{r^2} \, \omega_z(x', y') \, \mathrm{d}A' \tag{2.11a}$$

$$v(x,y) = +\frac{1}{2\pi} \iint_{\mathcal{A}} \frac{x - x'}{r^2} \, \omega_z(x', y') \, \mathrm{d}A' \tag{2.11b}$$

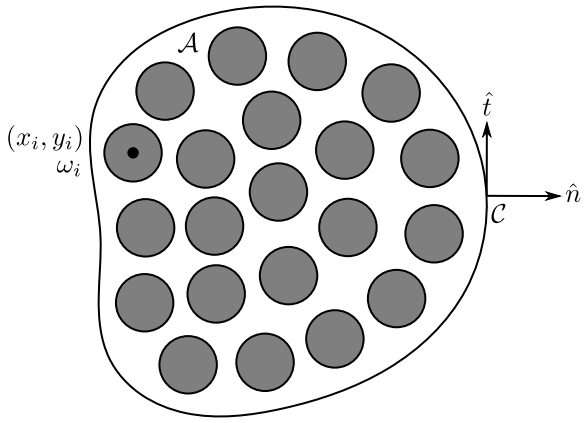

Figure 2.3: Schematic of a vortex patch with area $\mathcal{A}$ bounded by contour $\mathcal{C}$, which contains a collection of discrete vortices located at x_i, y_i with a vorticity of ω_i. The unit vector $\hat{n}$ and $\hat{t}$ are the boundary normal and tangential vectors, respectively.

where $r^2 = (x-x')^2+(y-y')^2$. When considering a compact vortex with uniform vorticity Ω, the above expressions become

$$u(x,y) = -\frac{\Omega}{2\pi}\iint_{\mathcal{A}} \frac{y-y'}{r^2}\,\mathrm{d}A' \tag{2.12a}$$

$$v(x,y) = +\frac{\Omega}{2\pi}\iint_{\mathcal{A}} \frac{x-x'}{r^2}\,\mathrm{d}A' \tag{2.12b}$$

Additionally, since

$$-\frac{1}{2}\frac{\partial}{\partial x'}\ln\left(r^2\right) = \frac{x-x'}{r^2} \tag{2.13a}$$

$$-\frac{1}{2}\frac{\partial}{\partial y'}\ln\left(r^2\right) = \frac{y-y'}{r^2} \tag{2.13b}$$

we can rewrite Equation (2.12) as

$$u(x,y) = +\frac{\Omega}{4\pi}\iint_{\mathcal{A}} \frac{\partial}{\partial y'}\ln\left(r^2\right)\,\mathrm{d}A' \tag{2.14a}$$

$$v(x,y) = -\frac{\Omega}{4\pi}\iint_{\mathcal{A}} \frac{\partial}{\partial x'}\ln\left(r^2\right)\,\mathrm{d}A' \tag{2.14b}$$

For further simplification, let $\vec{G} = [0, 0, \ln(r^2)]$ then

$$\nabla' \times \vec{G} = \left[\frac{\partial}{\partial y'}\ln\left(r^2\right), -\frac{\partial}{\partial x'}\ln\left(r^2\right)\right] \tag{2.15}$$

which allows the rewrite of Equation (2.14) in the vector form as

$$\boldsymbol{u}(\boldsymbol{x}) = \frac{\Omega}{4\pi} \iint_{\mathcal{A}} \nabla' \times \vec{G} \, \mathrm{d}A' \tag{2.16}$$

Applying Stokes' theorem, we arrive at the governing equation of contour dynamics

$$\boldsymbol{u}(\boldsymbol{x}) = -\frac{\Omega}{4\pi} \oint_{\mathcal{C}} \ln\left(r^2\right) \, \mathrm{d}\boldsymbol{l} \tag{2.17}$$

Note, the negative sign is a result of counter-clockwise integration path and $\boldsymbol{l}$ is infinitesimal vector element tangent to the patch boundary.

Regards to the implementation, the integral in Equation (2.17) can be solved exactly as

$$\int \ln\left(r^2\right) = r[\ln(r^2) - 2]. \tag{2.18}$$

Hence, the velocity at each boundary point can be easily computed by discritizing the contour into a collection of linear segments, compute the exact value of the integral over each linear segment using Equation (2.18), then sum for total contribution.

Chapter 3

Experimental investigation of a vortex ring impingement on a wall with a co-axial aperture[1]

This chapter presents the results of an experimental investigation of a vortex ring impinging on a wall with a co-axial aperture. It is organized as the following: the experimental setup is described in Section 3.1; experimental results and discussion are presented in Section 3.2; the semi-analytical model is introduced and compared with experimental results in Section 3.3; and Section 3.4 concludes this chapter.

3.1 Problem definition

Herein, we explore the problem of a vortex ring impinging on a rigid wall with a co-axially aligned aperture in an otherwise quiescent fluid (see Figure 3.1). In this figure, the vortex ring on the left is the incoming vortex ring, while the one on the right is the post-impact vortex, which is generated during the collision. A cylindrical coordinate system (x, r) is defined at the center of the aperture (see Figure 3.1), wherein r is the radial coordinate and r is the azimuthal coordinate, which is orthogonal to the aperture plane and pointing away from the incoming vortex ring. Properties associated with the incoming vortex ring are

[1]This work has been published on Physical Review Fluids [37] with me and my Ph.D. advisor Sean D. Peterson as co-authors. I was responsible for performing the experiment, analyzing the results and writing of the manuscript. Professor Peterson provided guidance for the study and edits for the manuscript.

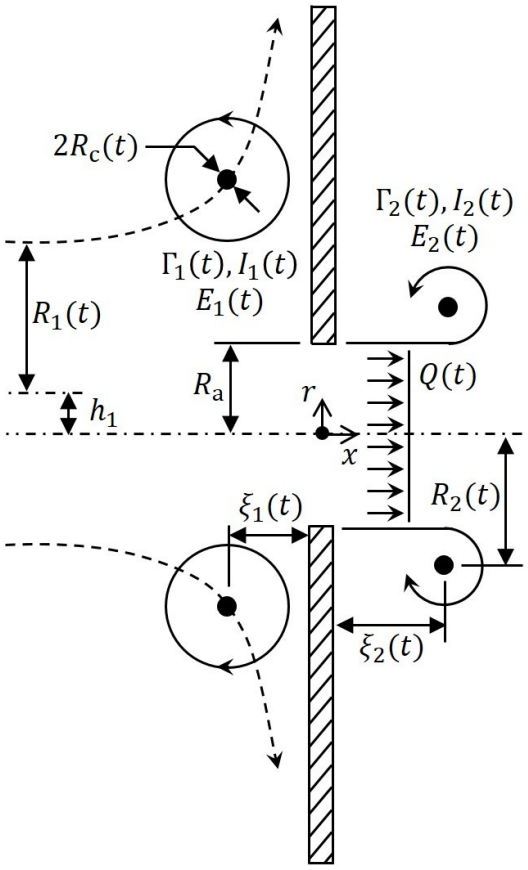

Figure 3.1: Schematic of a vortex ring impinging on a rigid with with a co-axially aligned aperture. The vortex ring on the right is the incoming vortex ring, while the vortex ring at the left is the post-impact vortex ring.

indicated with the subscript "1", while properties of the post-impact vortex ring behind the aperture are identified with the subscript "2". Each vortex ring is characterized by its radius R, core radius R_c, circulation Γ, impulse I, and energy E. The distance of a given ring from the wall is indicated by ξ. The vortex ring-induced flow across the aperture has a volumetric flow rate of Q, and the aperture has a radius of R_a.

3.1.1 Experiment setup

The vortex ring/wall interaction is explored experimentally using a custom vortex ring facility shown in Figure 3.2. The working fluid is water, which is contained in an acrylic

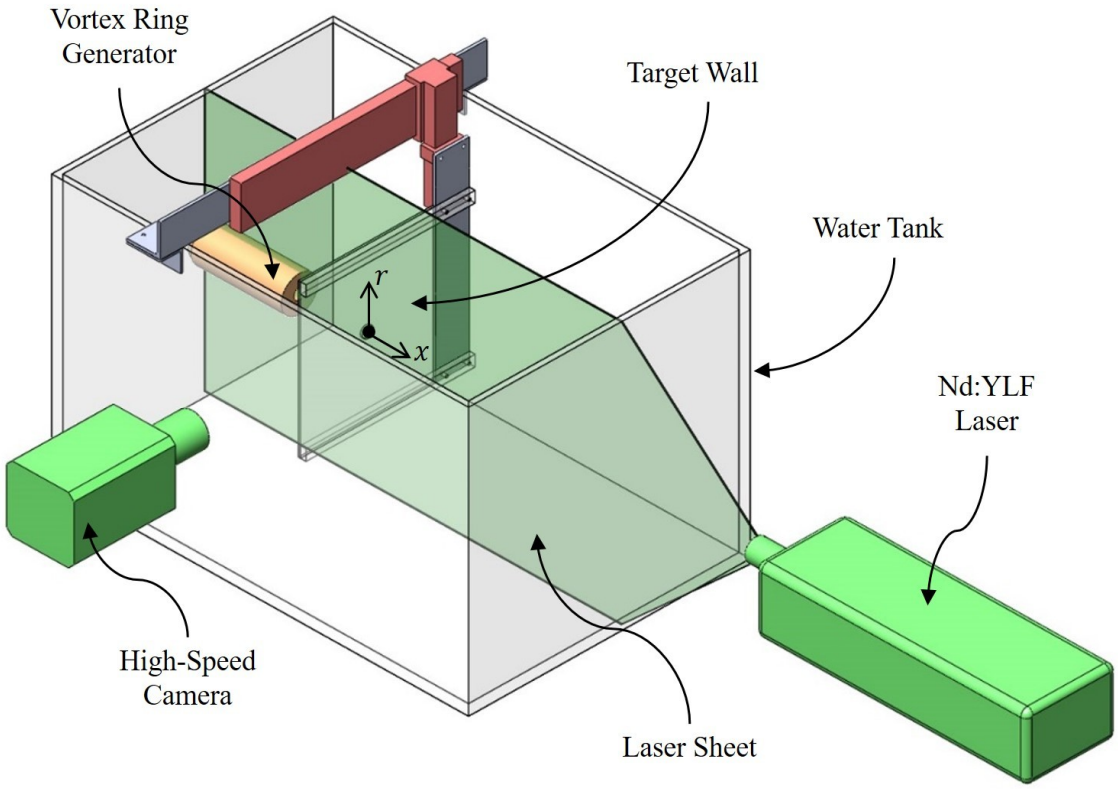

Figure 3.2: Experimental setup.

tank with a wall thickness of 12.7 mm and interior dimensions of $914 \times 610 \times 610\,\mathrm{mm}^3$. The target wall is a 4.5 mm thick Lexan sheet (SABIC Innnovative Plastics) with dimensions

$356 \times 305\,\mathrm{mm}^2$. Support bars are located at the top and bottom of the plate along the back side. The target wall is suspended on a L-bracket bridge that is placed across the width of the tank and is located at $98.9 \pm 1.0\,\mathrm{mm}$ away from the vortex ring generator outlet. The target wall is removable to accommodate plates with different aperture sizes.

The vortex ring generator is a piston/cylinder configuration with a $25.4 \pm 0.05\,\mathrm{mm}$ diameter sharp edged orifice outlet. The piston is located in a primary cylinder that has a diameter of $101.6 \pm 0.05\,\mathrm{mm}$. The piston is powered by a 1 HP DC motor (Boston Gear PM9100ATF-1) through a chain drive and a lead screw. The piston is controlled using a custom National Instrument LabVIEW VI through a NI DAQ PCIe-6323 card and a servo motor controller (Electro-Craft DC-35L). Image recording is triggered by the software one second before generator actuation in order to verify the quasi-static fluid assumption.

The fluid velocity field in a vertical plane passing through the vortex ring (and aperture) axis is measured via a particle image velocimetry (PIV) system (LaVision GmbH). The water is seeded with silver coated hollow glass particles (Potters Industries) with an average diameter of $13\,\mu$m and density $1.6\,\mathrm{g/cm}^3$. The light source is a 20 mJ/pulse Nd:YLF laser (Photonics Industries DM20-527D/R). Images are recorded with a Photron FASTCAM SA4 (500K-M1) high speed camera at full resolution (1024×1024 pixels) with frequencies of 100, 200, and 240 Hz for low Reynolds number PIV, high Reynolds number PIV, and flow visualization experiments, respectively. The field of view of the camera is $146 \times 146\,\mathrm{mm}^2$. The PIV recording are post-processed using a multi-pass interrogation scheme in DaVis 8.1.6 with a 32×32 pixel final investigation window size with 50% overlap. For the flow visualization studies, fluorescent dye is formulated by mixing water and fluorescent sodium salt (Sigma-Aldrich F6377).

3.1.2 PIV vector fields post processing

The azimuthal vorticity field ω_θ is computed from the velocity vector field at each time instant by Equation (3.1) using a fourth order central difference scheme [27, 87], where u and v denote the x and r velocity components, respectively.

$$\omega_\theta = \frac{\partial v}{\partial x} - \frac{\partial u}{\partial r} \tag{3.1}$$

Vortices are identified using the λ_2 criterion [100, 87], which is computed using a least squares differentiation scheme [87] with a threshold of $\lambda_2 < -5$. The selected threshold is small in comparison with the maximum value in the vortex ring core, thus enabling core identification throughout the interaction, but is sufficient to eliminate the background noise.

The positions of the vortex ring cores in the measurement plane are identified by the centers of their vorticity patches, while the core radii are estimated by fitting the vorticity patches to Gaussian distributions and computing a distances of one standard deviation from each peak [89, 94]. The circulation, impulse, and energy of each vortex ring, assuming them to be axisymmetric, are computed as

$$\Gamma = \int_A \omega_\theta \, \mathrm{d}A \tag{3.2a}$$

$$I = \pi\rho \int_A \omega_\theta \, r^2 \, \mathrm{d}A \tag{3.2b}$$

$$E = \pi\rho \int_A \omega_\theta \Psi \, \mathrm{d}A \tag{3.2c}$$

where ρ is the fluid density, $\mathrm{d}A$ is a unit area element, and Ψ is Stokes' stream-function, which is obtained by multiplying the traditional stream-function ψ by r [71]. The integrals in Equation (3.2) are numerically approximated using the trapezoid rule. The streamfunction ψ is acquired by solving Poisson's equation with ω_θ as the source term [87],

$$\frac{\partial^2 \psi}{\partial x^2} + \frac{\partial^2 \psi}{\partial r^2} = \omega_\theta \tag{3.3}$$

To compute ψ, Equation (3.3) is discretized using a 5 point second order differencing scheme [5] with $\psi = 0$ set as the boundary conditions in the far-field and along the wall. All vortex ring properties are estimated as the average of the values computed for the top and bottom vortex cores in the planar slice through the ring.

Accurately estimating the volumetric flow rate through the aperture, Q, from the PIV data is hindered by imprecision in locating the aperture boundaries and the relatively small number of vectors spanning it. To mitigate these issues, a multi-step process is employed to estimate Q. First, the center of the aperture is determined by locating its edges in the 2D PIV images. This provides the location of the coordinate system defined in Figure 3.2 in the experimental data. The velocity through the aperture is assumed to be axisymmetric. The radial velocity profile in the aperture is estimated by first averaging the velocity in two planes on either side of the wall, $\widetilde{u}(r, 0, t) \approx [u(r, x^-, t) + u(r, x^+, t)]/2$, where x^- and x^+ denote planes located immediately upstream and immediately downstream of the wall, respectively. Lastly, since the PIV measurement plane contains two radial velocity profiles (one above the hole centerline, one below, see Figure 3.2), these two profiles are also averaged to give $\widetilde{u}$. The volumetric flow rate is finally obtained by integrating $\widetilde{u}$ from $r = 0$ to the end of the field of view

$$Q(t) \approx 2\pi \int_0^\infty \widetilde{u}(r, 0, t) r \, \mathrm{d}r \tag{3.4}$$

3.1.3 Experimental parameters

To examine the effects of varying the Reynolds number (defined as $\mathrm{Re} = \Gamma_1^i/\nu$, where ν is the kinematic viscosity and the superscript "i" denotes vortex ring properties measured when the ring is approximately 3 ring radii from the wall) and aperture-to-ring-radius ratio (R_a/R_1^i) on the interaction process, a total of 6 different cases are examined. Specifically, we consider two Reynolds numbers and three aperture radii, as summarized in Tables 3.1 and 3.2. Each experiment is repeated 5 times, and the results are averaged. The uncer-

	Small Aperture	Medium Aperture	Large Aperture
R_a [mm]	6.26 ± 0.05	12.78 ± 0.05	19.35 ± 0.05
R_1^i [mm]	14.13 ± 0.38	14.00 ± 0.26	14.05 ± 0.51
R_{c1}^i [mm]	2.78 ± 0.15	2.88 ± 0.15	2.79 ± 0.16
Γ_1^i [mm^2/s]	1785.65 ± 39.96	1854.35 ± 50.49	1929.77 ± 61.26
E_1^i [μNs]	48.85 ± 2.63	51.24 ± 2.44	56.34 ± 4.40
I_1^i [μJ]	1126.66 ± 49.63	1162.13 ± 41.21	1208.20 ± 96.97

Table 3.1: Experimental parameter values and uncertainties for the low ($\mathrm{Re} \approx 1850$) Reynolds number cases.

	Small Aperture	Medium Aperture	Large Aperture
R_a [mm]	6.26 ± 0.05	12.78 ± 0.05	19.35 ± 0.05
R_1^i [mm]	16.57 ± 0.42	16.66 ± 0.37	16.73 ± 0.21
R_{c1}^i [mm]	2.93 ± 0.22	2.83 ± 0.22	2.79 ± 0.09
Γ_1^i [mm^2/s]	4743.75 ± 146.51	4432.89 ± 214.64	4545.33 ± 128.30
E_1^i [μNs]	430.37 ± 24.51	378.38 ± 19.04	398.01 ± 23.46
I_1^i [μJ]	4152.82 ± 138.08	3902.71 ± 147.11	4020.49 ± 112.63

Table 3.2: Experimental parameter values and uncertainties for the high ($\mathrm{Re} \approx 4600$) Reynolds number cases.

tainty in each parameter is estimated as the standard deviation of the measurements across the 5 repeated trials. The Reynolds number for the low and high Re cases are approximately 1850 and 4600, respectively, with some variability from experiment to experiment, as evidenced by the uncertainty in Γ in Tables 3.1 and 3.2. All post-processed data are filtered using a 10^{th} order low-pass Bessel filter with the cut-off frequency at 10% of the PIV sampling Nyquist frequency. We note that the low Reynolds number vortex rings

are generated by applying a shorter stoke length to the piston, which leads to premature formation, resulting in smaller ring radii [24].

The experimental results are non-dimensionalized using the initial ring radius R_1^i as the length scale, $(R_1^i)^2/\Gamma_1^i$ as the time scale, and $\rho(R_1^i)^3$ as the mass scale, where ρ is the fluid density and assumed to be 1000kg/m^3. For the remainder of the article, all variables shown are dimensionless unless otherwise noted. Lastly, in the following sections, $t = 0$ corresponds to one second after the piston actuation begins, which is when data collection (image capture) commences.

3.2 Results

3.2.1 Flow visualization

Flow visualization results of the interaction of a vortex ring with a planar wall with a coaxial aperture for the three aperture sizes are presented in Figure 3.3 for the high Reynolds number case. Three distinctive behaviors are observed between the three aperture sizes. In Figure 3.3(a), a laminar vortex ring approaches the small aperture. Upon impact in Figure 3.3(b), the vortex core deforms into an elliptical shape, while a column of fluid is induced though the aperture. The front of the fluid column diverges outward as the boundary layer separates from the aperture tip and begins to roll up. This is the same process as the vortex ring formation out of a piston/cylinder configuration described by Didden [24]. A short time later in Figure 3.3(c), the incoming vortex ring has merged with fluid ejected from the induced boundary layer along the wall to form of a pair of conjoined rings; these appear as two mushroom shaped dipoles in Figure 3.3(c). This ejection and interaction process is very reminiscent of the interaction of a vortex ring impacting a solid wall, see for example [101]. Walker *et al.* [101] observed a tertiary vortex ring at a similar Reynolds number for a vortex ring/full wall impact, which is not observed here. We note that the near wall fluid is not marked, so the full picture is not necessarily elucidated. Also observed in Figure 3.3(c) is a post-impact vortex ring formed from the fluid forced through the aperture. The presence of a trailing jet in the wake of this new ring indicates that the pinch off process has already occurred [31].

For the medium aperture case, shown in the second row of Figure 3.3, the core of the ring is also slightly deformed during impact with the wall, and a much larger column of fluid is pushed though the aperture. In this case, part of the incoming vortex ring core advects though the aperture, carrying some vorticity through, that joins with the vorticity rolling

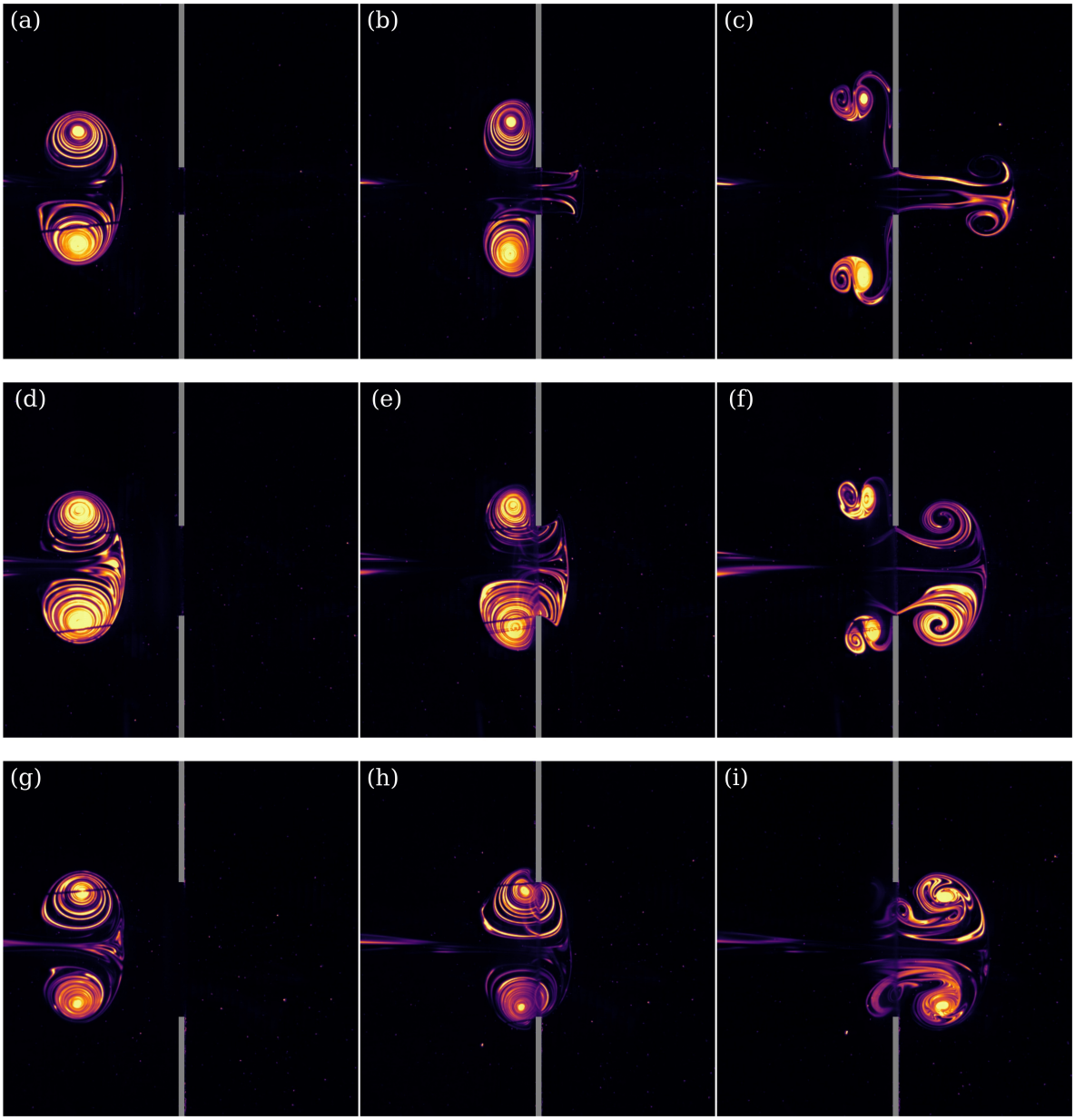

Figure 3.3: Flow visualization snapshots for the high Reynolds number case. Small, medium, and large aperture cases are shown in (a)-(c), (d)-(f), and (g)-(i), respectively. Snapshots at dimensional time $t = 3.33$s, $t = 3.75$s, and $t = 4.08$s are shown in each column from left to right, respectively.

up at the aperture edge. In Figure 3.3(f), we note that the interaction of the incoming vortex ring with the ejected wall boundary fluid (on the left side of the wall in the image) is similar to the small aperture case. However, the size and trajectory of the conjoined rings are slightly smaller, implying that more energy is transfered to the post-impact vortex ring.

In the large aperture case, shown in the last row of Figure 3.3, the aperture radius is greater than the ring radius; thus, the vortex core of the incoming ring does not interact appreciably with induced vorticity along the wall. In fact, the majority of the advecting vortex ring fluid appears to pass through the aperture, as shown in Figure 3.3(i), though the aperture tip does causes significant disturbance to the vortex ring. As such, some energy is expected to be lost from the vortex ring in comparison with a free vortex ring traveling the same distance.

3.2.2 Vorticity fields

To gain quantitative insights into the vortex dynamics, we examine the vorticity fields of the interaction, again using the high Reynolds number case as the exemplar. The vorticity fields corresponding to approximately the same time points as in Figure 3.3 are presented in Figure 3.4. We first note that there is a small vortex ring convecting out of the aperture for the small aperture case (see Figure 3.4(a)). This is produced by a structural vibration during piston actuation and has very weak circulation in comparison to the pre-impact vortex ring; as such, we presume its influence to be negligible.

The vorticity field of the small aperture case is shown in the first row of Figure 3.4. Upon impact (Figure 3.4(b)), the roll up of boundary layer vorticity on the left side of the wall (facing the incoming vortex ring) can be seen. Furthermore, vorticity associated with the newly formed post-impact vortex ring is observed to the right of the plate. The post-impact vortex ring induces weak opposite signed vorticity near the aperture tip. This is in agreement with the piston/cylinder vortex ring formation reported by Didden [24]. This patch of vorticity leads to post-impact vortex ring circulation loss due to opposite sign vorticity cancellation [24, 67]. In Figure 3.4(c), the post-impact vortex ring, as well as the ring pair ejected from the left side of the wall (also seen in Figure 3.3), are clearly visible. Also visible is the shear layer of the jet exiting the aperture caused by the initial pre-impact vortex ring. There is a clear separation between the post-impact vortex ring and the trailing jet shear layer, indicating that the "pinch off" [31] has already occurred.

Upon impact of the incoming vortex ring with the medium aperture (Figure 3.4(e)), we see that the induced vorticity on the left wall is weaker than in the small aperture case. In Figure 3.4(f), it is apparent that the ejected vortex ring pair (comprising the initial

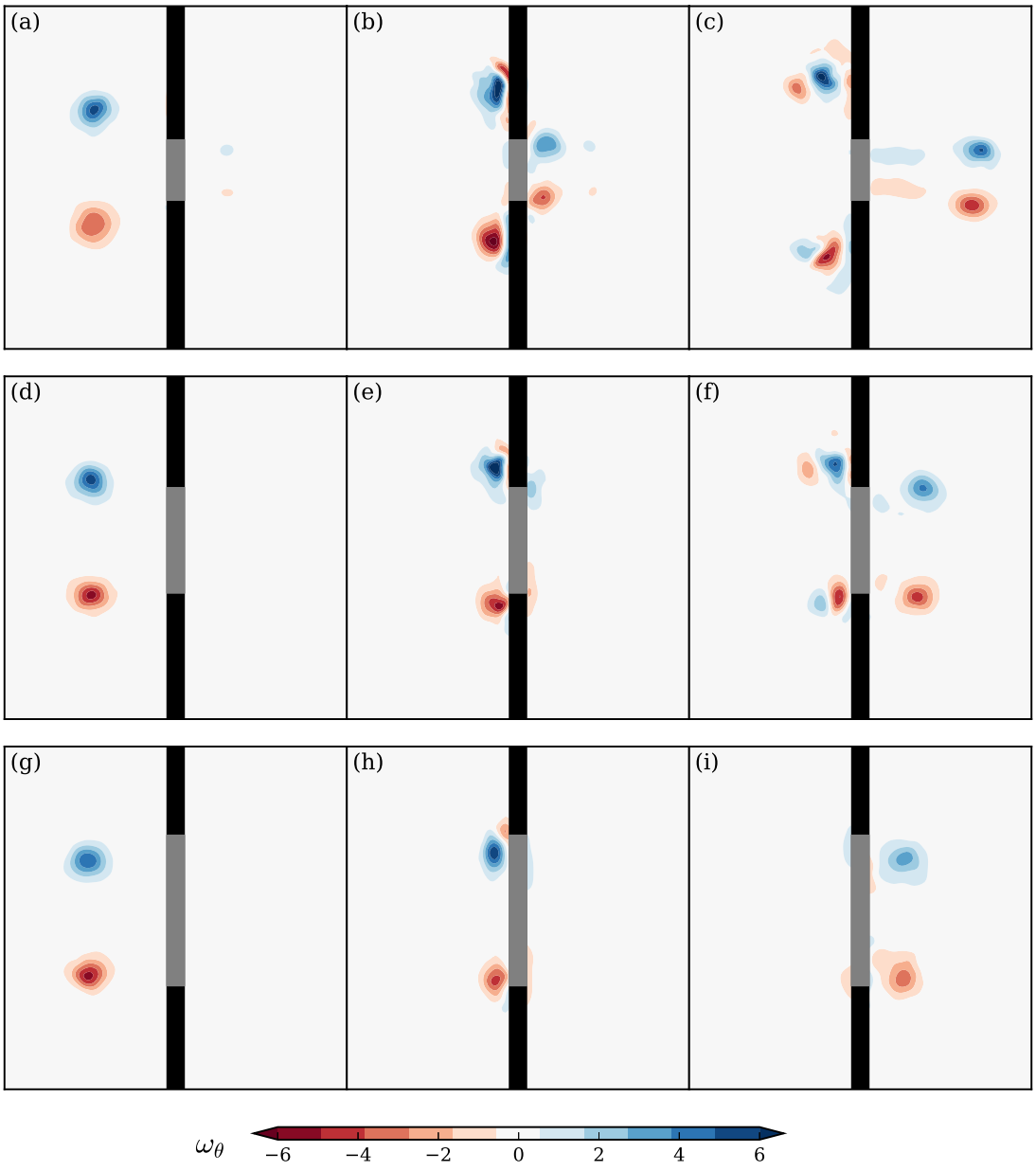

Figure 3.4: Vorticity field snapshots of the high Reynolds number case. Small, medium, and large aperture cases are shown (a)-(c), (d)-(f), and (g)-(i), respectively. Snapshots of $t = 15$, $t = 20$ and $t = 25$ are shown in each column from left to right, respectively. Grey and black areas are masked regions for the aperture and the wall, respectively.

vortex ring and the induced boundary layer vorticity) have weaker strength and size in comparison to the small aperture case. This suggests that some of the initial vortex ring's core vorticity passes through the hole. The absence of trailing jet vorticity in Figure 3.4(f) further suggests that the formation of the post-impact vortex ring is not terminated by the "pinch off" process [31]; rather, formation terminates when the incoming vortex ring ceases feeding fluid through the aperture, resulting in sub-maximal vorticity in the post-impact ring.

Lastly, in the large aperture case (third row of Figure 3.4), the approaching vortex ring simply passes though the aperture, though it does lose significant circulation in the process due to vorticity cancellation with the induced vorticity on the left side of the wall.

3.2.3 Temporal variation of relevant properties

Time traces of relevant properties, including both the pre- and post-impact vortex ring properties and the volumetric flow rate though the aperture Q, are presented in Figure 3.5. Recording of the incoming vortex ring properties commences once it fully enters the field of view, and ends when the vortex detection algorithm, described in Section 3.1.2, is no longer able to adequately discern the ring vortices (that is, when the signal-to-noise ratio in the algorithm gets too low). On the other hand, recording of the post-impact vortex ring properties begins once it is fully formed, which is identified as the time when it reaches maximum circulation. We note that the dimensionless recording time is shorter for high Reynolds number cases since time is scaled by initial vortex ring properties. Also, data prior to the post-impact vortex ring formation is not computed, in large part, due to data loss through the PIV masking applied to the wall.

Time-history plots of the small aperture cases are shown in the first column of Figure 3.5. The incoming vortex ring behaves in a similar manner for both Reynolds numbers, though the low Reynolds number ring shows more rapid decay of initial circulation, as expected due to stronger viscous effects, and as such the impulse and energy are lower. From Figure 3.5(a) and (d) we observed a growth in radius and deceleration of the incoming ring as it approaches the wall. Circulation and energy drop significantly due to interaction with the aperture, including vorticity cancellation with the induced wall vorticity, as shown in Figure 3.5(g) and (m). Vortex ring impulse increases (Figure 3.5(j)) as the ring radius increases. The post-impact vortex ring also has smaller property values for the lower Reynolds number case, as shown by the dashed lines in Figure 3.5.

Time traces for the medium aperture cases are shown in the second column of Figure 3.5. The trends are similar to the small aperture cases; however, there are three major

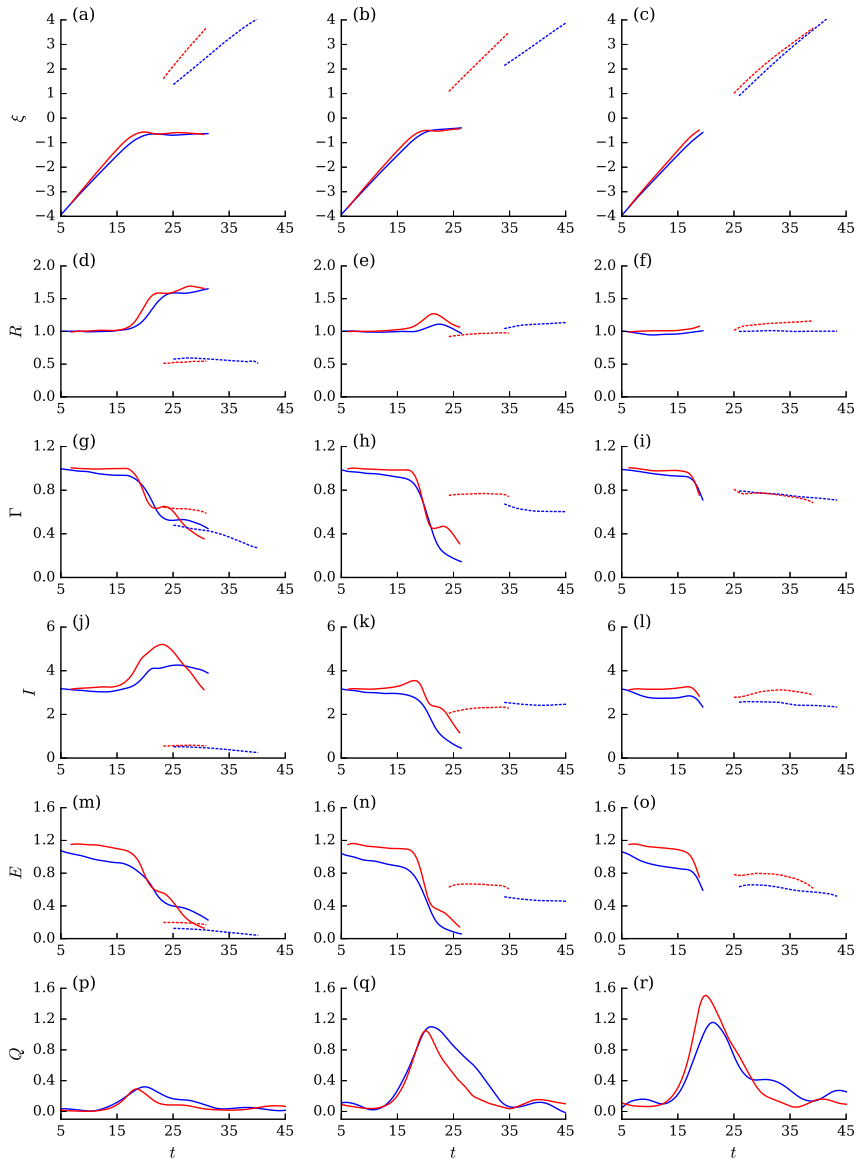

Figure 3.5: Time series of vortex ring properties during the interactions. Small, medium, and large aperture cases are presented in columns from left to right, respectively. Mean vortex ring x position, ring radius, circulation, impulse, energy, and aperture flow rate are organized into rows from top to bottom, respectively. Red and blue lines represent high and low Reynolds number cases, respectively, while solid and dashed lines denote pre-impact and post-impact vortex ring properties.

differences. Firstly, the incoming vortex is able to get closer to the wall and with less radial growth due to the larger opening. This results in minimal impulse growth during impact. Secondly, the post-impact vortex ring has greater circulation and a larger radius due to the larger aperture. Lastly, the formation times for the post-impact vortex ring, evidenced by the time point at the start of the dashed lines in the figure, are noticeably different between the two Reynolds numbers, unlike in the smaller aperture case. This is an another indication that vortex ring "pinch off" does not occur for the medium aperture case; that is, the post-impact ring does not attain maximal circulation.

The larger aperture case, shown in the third column of Figure 3.5, tells a relatively simple story; the incoming vortex ring passes though the aperture and loses some of its energy in the process to cross-diffusive vorticity annihilation [67], as discussed in reference to Figure 3.4.

With regards to the volumetric flow rate through the aperture, in all cases it increases as the pre-impact vortex ring approaches the hole, reaching a maximum value around the time of impact. The flow rate then decays as the pre-impact ring breaks down (or passes through the hole, in the case of the largest aperture radius). As expected, the total flow through the aperture increases with aperture size.

3.2.4 Comparing pre- and post-impact rings

The properties of the post-impact vortex ring with respect to the properties of the incoming pre-impact ring are compared in Figure 3.6 for all cases considered. We remind the reader that the low and high Reynolds number cases have slightly different aperture to ring radius ratios due to differences in the initial pre-imapct ring radii, as discussed in Section 3.1.3. We further note that pre-impact vortex ring properties are measured when the ring is approximately 3 radii away from the aperture (equivalent to the "initial" ring properties, denoted by superscript "i" in Tables 3.1 and 3.2), whereas the post-impact vortex ring properties are extracted once it has fully exited the masked wall region of the PIV recording or when it is fully formed, whichever is later.

The variation of R_2/R_1^i with aperture size is shown in Figure 3.6(a). The ratio first appears to increase linearly with the aperture size, likely due to the restriction on the post-impact vortex ring radius imposed by the aperture during formation [24]. When the aperture radius is nearly equal to the incoming ring (the medium aperture case), the ratio appears to reach a maximum, which is greater than 1; that is, the out-going post-impact ring is larger than the incoming ring. In this aperture size range, the interaction is transitioning from the formation of a new vortex ring at the hole to the incoming ring

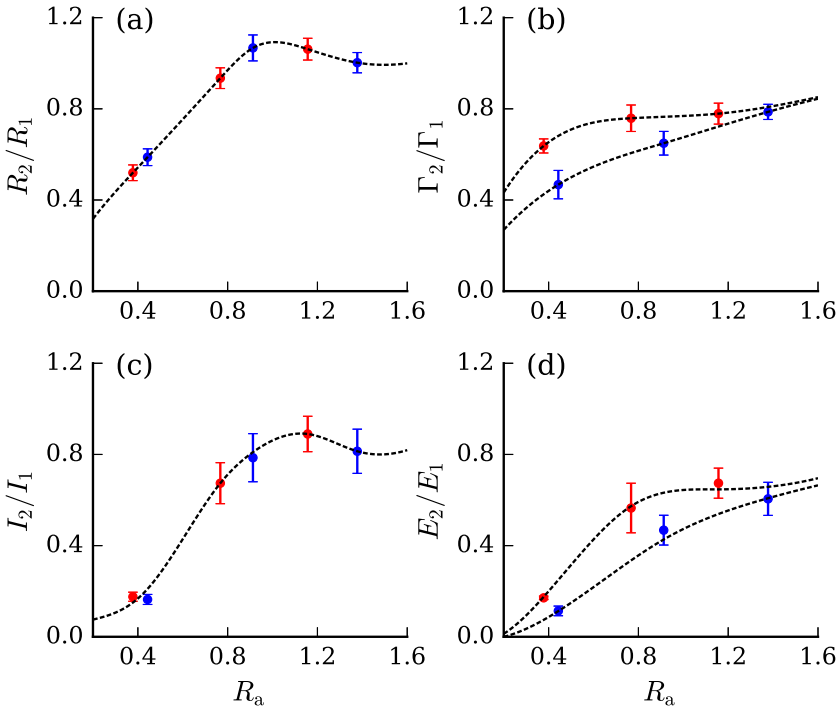

Figure 3.6: Ratios of the post- to pre-impact vortex ring properties versus aperture size for both Reynolds numbers. (a) Ring radius; (b) circulation; (c) impulse; and (d) energy. High and low Reynolds number cases are shown with red and blue symbols, respectively. Spline fit trend-lines are also included.

simply passing through the orifice. For larger aperture sizes, the ratio decreases back towards 1; obviously as $R_a \to \infty$, $R_2/R_1^i \to 1$. Comparing the two Reynolds number cases, it appears that R_2/R_1^i is relatively insensitive to Reynolds number in the range considered.

Unlike R_2/R_1^i, Γ_2/Γ_1^i (Figure 3.6(b)) displays a significant Reynolds number dependence. For both Reynolds numbers, the circulation of the post-impact ring increases with aperture size; the circulation ratio should asymptote to a value slightly less than 1 as R_a increases towards infinity. The lower Reynolds number cases show smaller post-impact ring circulation in comparison with the higher Reynolds number cases, likely due to greater loss in circulation through viscosity as the incoming ring approaches the wall (that is, Γ_1/Γ_1^i at the point of impact is smaller for the low Reynolds number case).

The ratio of impulses shown in Figure 3.6(c) follows the same general trends as the radius ratio, while the ring energy ratio in Figure 3.6(d) is similar to the circulation ratio in behavior. We expect that $I_2/{I_1}^i$ and $E_2/{E_1}^i$ approach values near (but slightly below) 1 as $R_a \to \infty$.

3.2.5 Post-impact vortex ring formation for a small aperture

As we previously established with the experimental observations, the formation of the post-impact vortex ring is terminated by the "pinch off" process, which was first described by Gharib *et al.* [31] for a piston/cylinder vortex generator. Pinch off refers to the separation of the leading vortex ring from its trailing jet, wherein the fluid ejected from an aperture is no longer able roll up into the vortex ring, forming instead into a trailing jet behind the leading vortex ring. Gharib *et al.* [31] explained this phenomenon using the Kelvin-Benjamin variational principle [9], which implies that the "pinch off" process occurs when the jet is unable to sustain the amount of the energy transfer required for a steady translating vortex ring with respect to its impulse-preserving iso-vortical perturbations [31, 64, 88, 93, 65, 77].

The energy of a vortex ring can be normalized as

$$\alpha = \frac{E}{\sqrt{\rho I \Gamma^3}} \tag{3.5}$$

which decreases during formation until it reaches a limit, denoted as α_{lim}, then the vortex ring "pinches off" from the jet and completes its formation. Gharib *et al.* [31] experimentally discovered that the limiting normalized energy is $\alpha_{\text{lim}} \approx 0.33$ for a piston/cylinder configuration. Additionally, the numerical study performed by Mohseni *et al.* [65] demonstrated that the normalized energy is invariant if fluid ejection out of a piston/cylinder

configuration has sufficiently long duration, sufficiently high Reynolds number, as well as producing adequately thin shear layer [71].

It is unlikely that the above conditions are met for the current study, since the source of the fluid ejection is itself a vortex ring. Furthermore, Allen and Naitoh [3] were able to produce a vortex ring with a much lower α_{lim} by using a variable radius orifice during formation. With the post vortex ring properties computed using Equation (3.2), we find that for both the Reynolds number cases in this study, the normalized energy is in the range of $\alpha_{\text{lim}} \approx 0.48 \pm 0.04$, which hints that the pinch-off process occurs much earlier during the formation in comparison to the piston/cylinder configuration.

3.3 Analytical Model

In this section, we develop an analytical model to predict the post-impact vortex ring properties based upon information about the incoming vortex ring for small R_1^i/R_a ratios. We treat the problem as primarily inviscid, neglecting the breakdown of the incoming vortex as it interacts with the wall. Vorticity production and diffusion from the aperture, which is the genesis of the post-impact vortex, is captured by adopting a slug model for vortex ring formation.

We begin with the potential flow model developed by Miloh and Shlien [59] for a vortex ring approaching a wall with an aperture. It has been recently employed by Hu *et al.* [36] to model the pressure loading across an annular smart material energy harvester due to an approaching vortex ring. The model assumes the ring core radius is small in comparison with the ring radius. The dimensionless initial core radius of the experimentally generated ring is in the range of $R_{c1}(0) = 0.17$ and 0.20 for the high and low Reynolds number cases, respectively. Following Miloh and Shlien [59], the potential field in the $x < 0$ half-space ϕ_- contains three components

$$\phi_-(x, r) = \phi_v(x, r) + \phi_w(x, r) + \phi_a(x, r) \tag{3.6}$$

where ϕ_v is the potential function for the incoming vortex ring, ϕ_w is the mirror of the incoming vortex ring across the $x = 0$ plane required to model the wall, and ϕ_a is a surface distribution of sinks of varying strength to model the aperture. The velocity field can be obtained by computing the gradient of the potential function. Full expressions for each term in Equation (3.6) are presented in Appendix A.

The self-induction speed of a thin core vortex ring in an infinite medium, assuming a

Gaussian distribution of vorticity in the core, is given by [89, 94]

$$U_s(R_1, R_{c1}) = \frac{\Gamma_1}{4\pi R_1}\left[\ln\left(\frac{8R_1}{R_{c1}}\right) - 0.558\right] \tag{3.7}$$

For the vortex core to satisfy continuity as the ring radius changes, the core must maintain a constant volume throughout the interaction. As such, the core radius at any time $R_{c1}(t)$ can be computed as

$${R_{c1}}^2(t)R_1(t) = {R_{c1}}^2(0)R_1(0) \tag{3.8}$$

The total advection velocity of the incoming vortex ring (U_1, V_1) due to self-induction, the wall (image ring), and the aperture is

$$U_1(t) = \frac{\mathrm{d}\xi}{\mathrm{d}t} = U_a + U_w + U_s \tag{3.9a}$$

$$V_1(t) = \frac{\mathrm{d}R_1}{\mathrm{d}t} = V_a + V_w \tag{3.9b}$$

where (U_w, V_w) and (U_a, V_a) are the velocities at the vortex ring core due to the image ring (wall) and aperture, respectively. Full expressions for these velocity components are presented in Appendix A.

The volumetric flow rate across the aperture Q, is computed as

$$\begin{aligned} Q(\xi, R_1) &= 2\pi \int_0^{R_a} \left.\frac{\partial \phi_-}{\partial x}\right|_{x=0} r \ \mathrm{d}r \\ &= 2\Gamma_1 \left\{ R_a + \left[({R_1}^2 + \xi^2 - {R_a}^2)^2 + 4\xi^2 {R_a}^2 \right]^{1/4} \sin\left(\sigma/2\right) \right\} \end{aligned} \tag{3.10a}$$

where

$$\sigma(\xi, R_1) = \tan^{-1}\left(\frac{-2\xi R_a}{{R_1}^2 + \xi^2 - {R_a}^2}\right) \tag{3.10b}$$

Inspection of Equation (3.10b) reveals that as $t \to \infty$, corresponding to $\xi \to 0$ and $R_1 \to \infty$, the flow rate converges to a constant value of $Q = 2\Gamma_1 R_a$. This contradicts the observation in the present experiments, in which the volumetric flow rate initially increases before reaching a maximum and subsequently decreasing, see the last row of Figure 3.5. Furthermore, this implies that the vortex ring energy becomes unbounded, as seen from the equation for the energy of a vortex ring in an infinite medium [94]

$$E_1(R_1, R_{c1}) = \frac{1}{2}{\Gamma_1}^2 R_1 \left[\ln\left(\frac{8R_1}{R_{c1}}\right) - 2.05\right] \tag{3.11}$$

For fixed Γ_1, this expression is unbounded as $R_1 \to \infty$ regardless of the change in vortex ring core radius.

To resolve this issue with non-physical model behavior in Q as $t \to \infty$, we propose a conservation of energy condition on the incoming vortex ring (assuming the expression for its energy, Equation (3.11) is not influenced by the wall or aperture). Specifically, the total energy of the system E_s is set to be the initial incoming vortex ring energy, calculated from Equation (3.11). This value remains invariant for the entire interaction under the potential flow assumptions, and thus

$$E_s = E_1(R_1(0), R_{c1}(0)) = \text{const} \tag{3.12}$$

We estimate the rate of energy advected through the aperture, which forms the post-impact ring, using a slug flow model [24, 31, 64], to be

$$\frac{\mathrm{d}E_2(t)}{\mathrm{d}t} = \frac{Q^3(t)}{2\pi^2 {R_a}^4} \tag{3.13}$$

We note that the slug model assumes the radial velocity profile to be uniform. Hence, the incoming vortex ring energy at any time is

$$E_1 = E_s - E_2 \tag{3.14}$$

In order to maintain the constant total energy condition, that is, for the incoming vortex ring energy to decrease as a result of the interaction, the circulation of the ring must be allowed to vary in time. This, in turn, means that the advection speed of the vortex ring, as well as the aperture flow rate, will be time varying.

By combining Equation (3.6) to Equation (3.14), the governing differential equations in Equations (3.9) and (3.13) can be solved to determine the system dynamics. Equations (3.9) and (3.13) are solved using the FORTRAN ODEPACK LSODA algorithm. The low Reynolds number case is simulated with initial conditions $\xi(0) = -5.0$, $R_{c1}(0) = 0.197$, and $R_a = 0.443$. The initial conditions of $\xi(0) = -5.0$, $R_{c1}(0) = 0.177$, and $R_a = 0.378$ are used for the high Reynolds number case. These values are extracted from the experimental measurements.

Figure 3.7 compares the model prediction (black lines) with the experimental results, wherein the 95% confidence intervals for the experiments are shown as grey bands. Figure 3.7(a) and (b) compare the predicted and measured incoming vortex ring x positions versus time for the low and high Reynolds number cases, respectively. In both cases, initial agreement between model and experiment is excellent, with the low Reynolds number

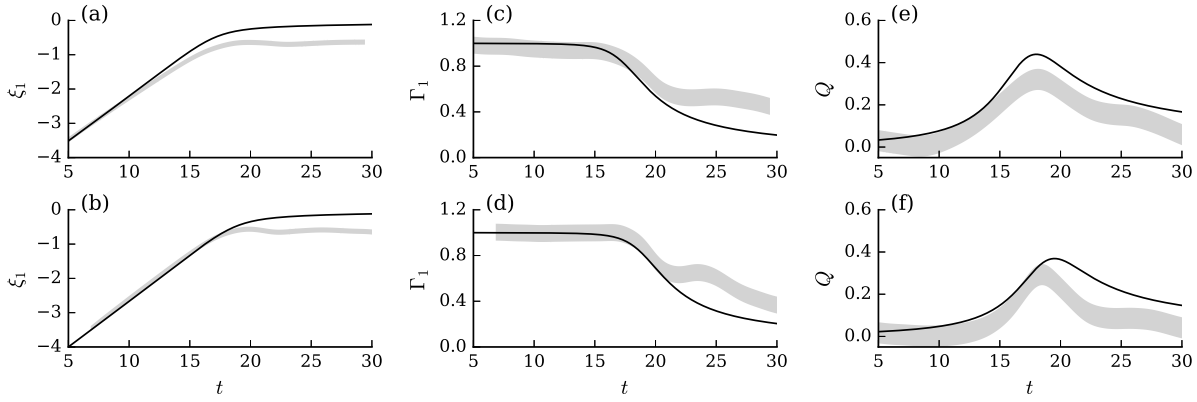

Figure 3.7: Analytical and experimental results comparison. The analytical results are displayed as black lines, while the experimental results with their 95% confidence intervals are represented with grey bands. Low and high Reynolds number cases are shown (a)-(c) and (d)-(f), respectively. The incoming vortex ring's x position, its circulation, and aperture flow rate are shown in each of the columns from left to right, respectively.

results starting to diverge sooner due to viscosity. The model and experimental results for both the low and high Reynolds number cases begin diverge around the time of the impact ($t \approx 20$). Additionally, the incoming vortex ring in the inviscid model propagates closer to the wall than in the experiments, likely due to the finite core size of the experimental ring (in comparison with the infinitesimal vortex core thickness assumed in the model). As previously stated, vortex ring breakdown is not captured in the model.

The second column of Figure 3.7 features the circulation comparison. Agreement between the model and the experiment is good until the boundary layer rolls up into the secondary vortex ring at $t \approx 20$; the circulation reduction in the model is a consequence of the energy conservation model. The aperture flow rate comparisons are shown in the last column of Figure 3.7. Overall, the analytical model is able to forecast the trend and behavior well, although the model slightly over-predicts the flow magnitude. The over-prediction is likely due to the lack of a viscous loss mechanism in the analytical model.

With the aperture flow rate prediction ability validated for the analytical model, we move to employing the Kelvin-Benjamin variational principle [9] to predict the post-impact vortex ring properties. As explained previously in Section 3.2.5, the post-impact vortex ring formation is terminated when its normalized energy α reaches the limit $\alpha_{\text{lim}} \approx 0.48$ via the "pinch off" process. The vortex ring properties will no longer change after pinch off; thus, the properties at this moment can be taken as the final post-impact vortex ring

properties.

Again, we employ the slug model to estimate the properties of the flow across the aperture [31, 64, 93]. Assuming no loss across the aperture, the energy, momentum, and circulation of the jet are transfered to the post-impact vortex ring. Thus, utilizing the aperture flow rate Q obtained from the analytical solution, the energy of the post-impact vortex ring can be obtained using Equation (3.13), while its impulse and circulation can be estimated with

$$\frac{\mathrm{d}I_2(t)}{\mathrm{d}t} = \frac{Q^2(t)}{\pi {R_a}^2} \tag{3.15a}$$

$$\frac{\mathrm{d}\Gamma_2(t)}{\mathrm{d}t} = \frac{Q^2(t)}{2\pi^2 {R_a}^4} \tag{3.15b}$$

All three properties at any time instance can be obtained by numerical integration, then the normalized energy α can be computed using Equation (3.5). Once α reaches α_{lim}, the vortex ring is considered fully formed and its properties no longer change.

Using the experimentally obtained parameters $R_a = 0.378 \pm 0.009$ and $\alpha_{\mathrm{lim}} = 0.48 \pm 0.04$, we obtain a post to pre-impact circulation ratio of $\Gamma_2/\Gamma_1 = 0.44 \pm 0.1$ for the high Reynolds number case. The experiment circulation ratio is $\Gamma_2/\Gamma_1 = 0.64 \pm 0.03$; we see that the model under-predicts the ratio, despite the over-prediction of the aperture flow rate Q shown in Figure 3.7(f). The discrepancy is partially due to the over-prediction of the flow rate that causes the ring to reach the limiting energy faster, which leads an earlier separation. The discrepancy is also potentially due to the use of a slug velocity profile; the numerical study by Rosenfeld *et al.* [88] demonstrated that the velocity profile has a significant influence (up to 400%) on the ring formation values. Furthermore, the roll-up of the incoming vortex ring keeps it near the aperture tip during the interaction, which could manipulate the formation process; similar to the situation of generating a train of vortex rings, where the leading vortex ring will alter the subsequent vortex ring formation [51, 92]. Note, the low Reynolds number case is not compared, since its high viscous effects further invalidates the slug model assumption for the flow though the aperture.

3.4 Conclusion

This study examined the interaction of a thin core vortex ring impinging on a wall with a co-axially aligned aperture for two different incoming ring Reynolds numbers. Flow visualization and particle image velocimetry was employed to elucidate the impact mechanics for

three aperture sizes, one smaller than the incoming ring, one with radius approximately equal to the ring radius, and one larger than it. In the small aperture to ring radius case ($R_a/R_1 \approx 0.41$), the interaction of the ring with the wall is similar to that of a ring impacting a solid wall. However, flow induced by the incoming ring passes through the aperture and rolls up in to a second vortex ring, which eventually pinches off and advects away. The strength of the generated vortex ring scales with the Reynolds number of the incoming ring, though its radius is only mildly influenced. When the aperture radius is approximately equal to the ring radius ($R_a/R_1 \approx 0.83$), the core partially passes through the aperture and merges with vorticity rolling up due to fluid passing through the hole. At still larger aperture radius ($R_a/R_1 \approx 1.26$) the ring passes through the hole, though it loses 35% of its initial energy in the process.

This chapter further presents a model for predicting the post-impact vortex ring properties for the small aperture case at high Reynolds numbers. The model combines a modified version of the potential flow solution introduced by Miloh and Shlien [59] with a slug flow model for vortex ring formation at a sharp-edged orifice. The original potential flow model predicts that flow through the aperture reaches and sustains a constant value as time going to infinity, in contrast to the experimental observation. We overcome this by developing an energy conservation argument, which results in the incoming vortex ring circulation no longer being time invariant. The result is a model that reasonably captures the aperture flow rate and post-impact vortex ring properties observed in the experiments for the high Reynolds number case.

Chapter 4

Hydrodynamic impulse enhancement of a vortex ring interacting with a co-axial aperture[1]

Chapter 3 experimentally studied a vortex ring colliding with a co-axial aperture to explore the dynamics of a viscous vortex core impacting a thin edge. The degree of core impact with the thin edge was controlled by the aperture-to-ring radius ratio, and the axisymmetry of the geometry enforced in a largely two-dimensional interaction. The experiments explored a small range of aperture-to-ring radius ratios and revealed that a vortex ring exited the aperture regardless of aperture size. For small radius ratios, the wall blocked the majority of the incoming ring, which subsequently followed the classical vortex rebound trajectory. The colliding ring did, however, induce flow through the aperture, which created a shear layer from the tip that formed into a new vortex ring exiting the aperture. For sufficiently large apertures, vortex rebound no longer occurred and the entire incoming ring passed through the aperture. Interestingly, the results in Figure 3.6 demonstrated a rise in the hydrodynamic impulse for radius ratios on the order of one, though the physical mechanism for this was not investigated.

In this chapter we further elucidate the physical mechanisms associated with the experimentally observed vortex impulse enhancement detailed in Chapter 3. Additional, the

[1]This work has been published on Journal of Fluid Mechanism [38] with me and my Ph.D. advisor Sean D. Peterson as co-authors. I was responsible for performing the simulation, analyzing the results and writing of the manuscript. Professor Peterson provided guidance for the study and edits for the manuscript.

experimental results are limited by the optical access, and the practicality of aperture manufacturing and alignment. Hence, we seek to improve the documentation of the vortex interaction by taking advantages of the high resolution data from the numerical results.

This chapter is organized as follows: Section 4.1 outlines the problem formulation and numerical setup; Section 4.2 provides an overview of the vortex dynamics; Section 4.3 examines the passive enhancement of hydrodynamic impulse experienced by the incoming vortex ring; Section 4.4 explains the structural loading experienced from the core interaction; Section 4.5 discusses the circulation changes of the vortex ring after the interaction; Section 4.6 briefly touches upon the influence of Reynolds number; and Section 4.7 summarizes the major findings of this chapter.

4.1 Problem definition

We numerically explore the problem of an axisymmetric vortex ring colliding with a wall with a co-axial aperture of radius R_a in an otherwise quiescent viscous fluid, as shown schematically in Figure 4.1. A cylindrical coordinate system $(r,\ x)$ with origin at the

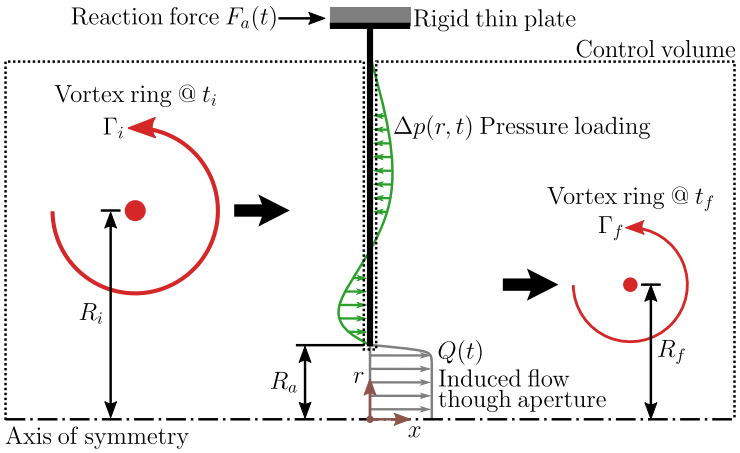

Figure 4.1: Schematic of a vortex ring interacting with a rigid wall with a co-axial aperture in an otherwise quiescent fluid.

center of the aperture is defined such that the x direction aligns with the aperture axis and is positive in the direction of the incoming vortex ring propagation. The velocity field is given by $\boldsymbol{u} = (u, v)$, where u and v are the axial and radial components, respectively. The

azimuthal vorticity field is obtained from $\omega_\theta(x,r,t) = \partial v/\partial x - \partial u/\partial r$, while the vortex ring circulation is computed as

$$\Gamma(t) = \iint_\Omega \omega_\theta(x,r,t)\ \mathrm{d}x\ \mathrm{d}r \tag{4.1}$$

where Ω is the vortex core region, defined herein by the contour of 1% of the initial maximum vorticity of the ring ($0.01 \max[\omega_\theta(x,r,0)]$). The vortex ring radius is given by $R(t)$, which we define as the distance from the x-axis to the location of maximum vorticity within the vortex core. The vortex ring radius is located with sub-grid scale accuracy by fitting a Gaussian distribution to the vorticity field in the least squares sense, similar to sub-pixel interpolation schemes for correlation peak detection in particle image velocimetry [87]. The volumetric flow rate through the aperture is computed as

$$Q(t) = \int_0^{R_a} u(r,0,t)\ r\ \mathrm{d}r \tag{4.2}$$

and the pressure difference across the wall is given by $\Delta p(r,t)$.

The primary interest of this article is to examine how the momentum of the impinging ring is altered by its interaction with the aperture. Thus, it is convenient to express the momentum of the flow field in terms of vorticity. Applying the derivative moment transformation to the density normalized momentum integral yields

$$\int_{C_v} \boldsymbol{u}\ \mathrm{d}V = \frac{1}{2}\int_{C_v} \boldsymbol{x}\times\boldsymbol{\omega}\ \mathrm{d}V - \frac{1}{2}\int_{\partial C_v} \boldsymbol{x}\times(\boldsymbol{n}\times\boldsymbol{u})\ \mathrm{d}S \tag{4.3}$$

where $\boldsymbol{x}$ and $\boldsymbol{n}$ are position and boundary normal unit vectors [104], and ∂C_v is the boundary of the control volume C_v. The first term on the right-hand side of Equation (4.3) is the hydrodynamic impulse (or vortex impulse), while the second term accounts for boundary flux and motions. Assuming the fluid in the far field is quiescent, and no-slip along the wall, the second term is zero [2, 104]. Further assuming axisymmetry, the hydrodynamic impulse $I(t)$ simplifies to

$$I(t) = \pi \iint_{C_v} \omega_\theta(x,r,t)\ r^2\ \mathrm{d}x\ \mathrm{d}r. \tag{4.4}$$

By integrating over the vortex core Ω, Equation (4.4) can be used to compute hydrodynamic impulse of a vortex ring [90, 31]. As note by Cantwell [14] for an unbounded fluid, $I(t)$ only accounts for 2/3 of the external forcing required to generate the fluid momentum, with the remainder needed to adjust the far-field pressure to oppose the motion.

Aperture to initial ring radius ratios (R_a/R_i) spanning from 0 to infinity ($R_a/R_i = 0$, 0.2, 0.4, 0.6, 0.8, 0.9, 1.0, 1.1, 1.2, 1.3, 1.4, 1.6, 1.8, and ∞) at three Reynolds numbers ($\mathrm{Re} = \Gamma_i/\nu = 1000$, 2000, and 3000) are considered, where ν is the fluid kinematic viscosity. The subscript i denotes the initial properties of the vortex ring ($t = 0$), when the vortex ring is located $4R_i$ upstream of the aperture. For the purpose of comparison, the final properties of the vortex ring, denoted by subscript f, are taken when the vortex ring completely clears the aperture. The final times are $t_f\Gamma_i/{R_i}^2 = 42.3$, 39.1 and 38.0 for $\mathrm{Re} = 1000$, 2000, and 3000, respectively, where t is time.

4.1.1 Numerical setup

The two-dimensional axisymmetrical simulations were performed using the second order accurate transient incompressible Naiver-Stokes equations solver `icoFoam` in OpenFOAM 4.1. The wedge-shaped computational domain, comprising fine and course mesh regions generated using Gmsh [30], is summarized in Figure 4.2. All vortex interactions occur

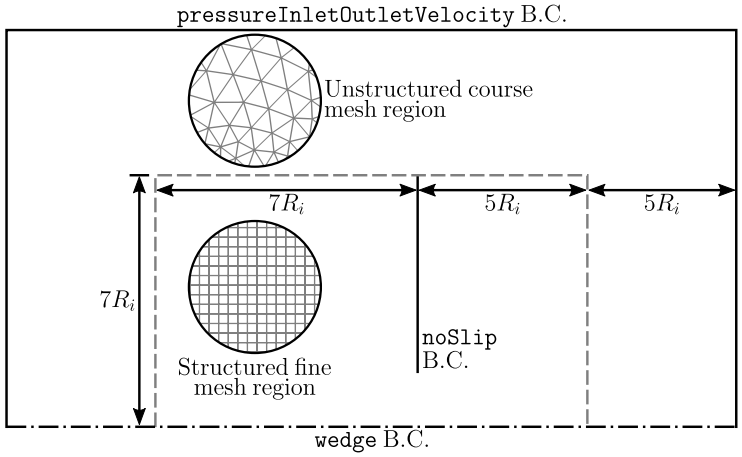

Figure 4.2: Schematic of the computational domain. Note: B.C. stands for boundary condition.

in the $12R_i \times 7R_i$ fine mesh region, which comprises $0.01R_i \times 0.01R_i$ structured cuboid elements. A course triangular prism mesh pads the fine mesh region, extending the domain by an additional $5R_i$ in all directions (except for the axisymmetry boundary) to reduce the influence of the far-field boundary condition. The employed numerical scheme is not energy conserving [80, 83], and as such the mesh size used in this study is much smaller than previous second-order accurate vortex ring-wall interaction simulations (e.g. Chu *et*

al. [17]) to minimize numerical diffusion effects [83]. The mesh size is sufficiently small that the boundary layer near the aperture plate is resolved without mesh inflation layers. The mesh size was selected based on a grid convergence study of the full wall impact ($R_a/R_i = 0$) case, which produces the most vorticity and strongest boundary layer. The convergence metric was peak enstrophy varying by less than 1%.

The vortex core radius is assumed to be much larger than the plate thickness, and thus the wall is modeled with a zero thickness no-slip baffle extending to the edge of the fine mesh region. Note that the wall does not extend to the outer unstructured region to prevent back pressure across the aperture, similar to the experiments in Chapter 3. The `totalPressure` is applied as the far-field boundary condition, which sets the pressure $p = 0$ for outflow and $p = |\boldsymbol{u}|^2/2$ for inflow to mimic an unbounded fluid domain. The `wedge` boundary condition is applied on the faces of the one-element-thick domain to facilitate the axisymmetrical simulation.

4.1.2 Vortex initialization

The vortex ring was initialized in an open domain (no wall) with a Gaussian (Lamb-Oseen) vorticity distribution given by

$$\frac{\omega_\theta(x, r, 0){R_o}^2}{\Gamma_o} = \frac{1}{\pi(R_c/R_o)^2} \exp\left[-\frac{(x - x_o)^2/{R_o}^2 + (r - R_o)^2/{R_o}^2}{(R_c/R_o)^2}\right] \tag{4.5}$$

where Γ_o, R_c, R_o, and x_o are the circulation, core radius, ring radius, and axial position of the ring, respectively. The simulation was allowed to evolve until the vortex core obtained a stable vorticity distribution, as shown in Figure 4.3. This vorticity distribution was then mapped to the actual domain (with wall and aperture) with the ring centered at $x/R_i = -4$. The values of Γ_o, R_c, and R_o were selected such that the vortex ring had the desired initial attributes R_i and Γ_i after core transition completed (Figure 4.3(d)).

4.1.3 Validation

We validate the simulations by comparison with published experimental data for two conditions: a vortex ring impacting a solid wall [17]; and the experimental results in Chapter 3. Figure 4.4 compares the trajectories of a vortex ring impacting a solid wall from the simulations and experiments for Re = 2000. The simulation accurately predicts the vortex rebound observed experimentally using flow visualization. This further implies that the vortex position in simulations can be assessed with reasonable accuracy via the vorticity

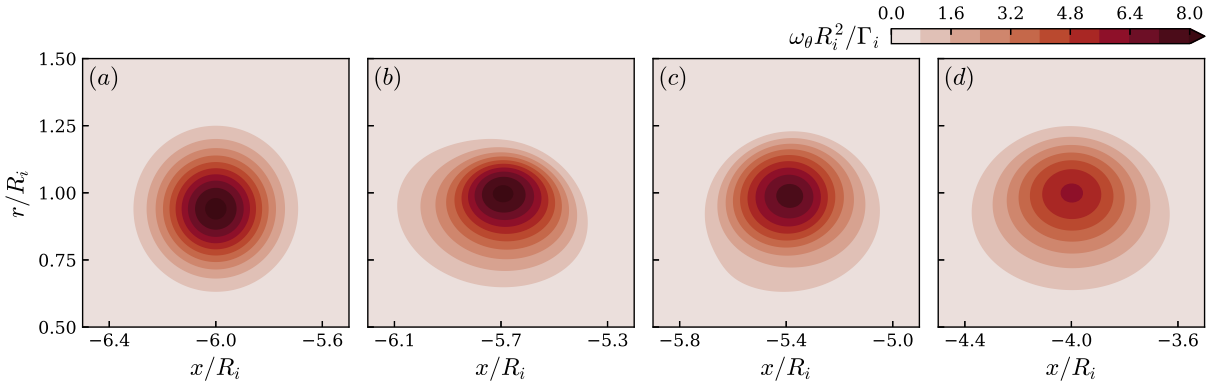

Figure 4.3: Initial transition of the vortex core from a Gaussian distribution to a realistic elliptical distribution. Vorticity fields are shown at $tR_i{}^2/\Gamma_i \approx$ (a) -8.3, (b) -7.2, (c) -5.9, and (d) 0 for all Reynolds number.

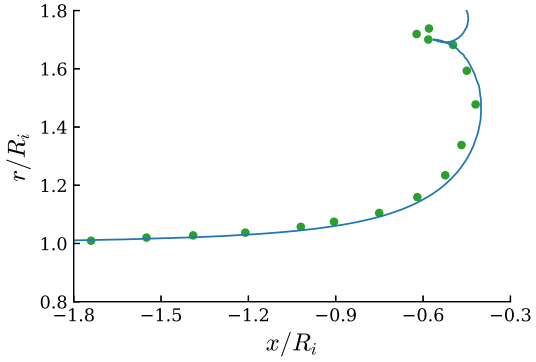

Figure 4.4: Trajectory of a vortex ring impacting a wall at $\mathrm{Re} = 2000$. Simulation results are represented by a line, while the experimental results from Chu *et al.* [17] are marked by dots.

peak location, despite the core deformation during the collision. Qualitative comparison with flow visualizations in Chapter 3 are shown in Figure 4.5 for $R_a/R_i = 0.4$ at Re = 4000 (Figure 4.16 in Section 4.3.1 further compares experiment and simulation results for the $R_a/R_i = 1.2$ case). The simulations show very good agreement with the experiments, ac-

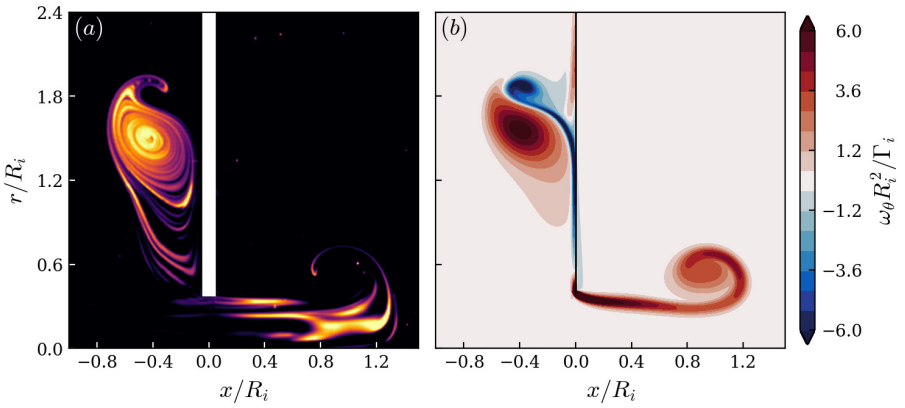

Figure 4.5: Comparison between (a) flow visualization from Chapter 3 and (b) simulation of a vortex ring impacting a coaxial aperture with $R_a/R_i = 0.4$ and Re = 4000.

curately capturing the core deformation and secondary vortex production throughout the interaction.

Of potential concern is the impact of the employed axisymmetric assumption on the flow development. Orlandi and Verzicco [81], for example, have shown that the axisymmetrical condition prevents azimuthal instability development at higher Reynolds numbers. However, Swearingen *et al.* [95] revealed that the azimuthal instability develops on the secondary vortex ring under the strain field of the primary vortex ring. Chapter 3 have shown the strength of both the primary and secondary vortex rings are reduced due to the aperture, which damps the azimuthal instability. Furthermore, the azimuthal instability only reaches a noticeable amplitude at the late stage of the interaction for the classical vortex ring-wall interaction case [81, 95, 16]. Thus, the occurrence of the azimuthal instability far exceeds the timescale of interest in the present study, and the axisymmetrical simulations are deemed adequate for the Reynolds numbers investigated. This is corroborated by the observation that the dye layers in the flow visualization are preserved upon impact, indicating that the flow remains laminar throughout the interaction.

4.2 Results overview

We classify the vortex dynamics of the ring-aperture interaction into three regimes depending on the aperture to initial ring radius ratio R_a/R_i, namely, the impact, "vortex nozzle", and slip-through regimes. For the impact regime ($R_a/R_i \lessapprox 0.9$), the aperture wall blocks most of the colliding vortex ring and causes it to rebound, with behavior qualitatively similar to a vortex ring impacting a solid wall. In the slip-through regime ($R_a/R_i \gtrapprox 1.3$) the majority of the incoming ring passes through the aperture and no rebound is observed. The "vortex nozzle" regime ($0.9 \lessapprox R_a/R_i \lessapprox 1.3$) exhibits behavior qualitatively similar to the slip-through regime, however, quantitatively the vortex ring impulse is enhanced during the interaction with the aperture. These three regimes are discussed in the following sub-sections using the Re = 2000 case as an exemplar.

4.2.1 Impact regime

We begin with the special case of a vortex ring impacting a solid wall ($R_a/R_i = 0.0$) as a reference baseline; the vorticity evolution is shown in Figure 4.6. This configuration is well documented, see, for example, Walker *et al.* [101] and Cheng *et al.* [16], and as such we include only a brief description herein. In Figure 4.6(a) and (b), a boundary layer is

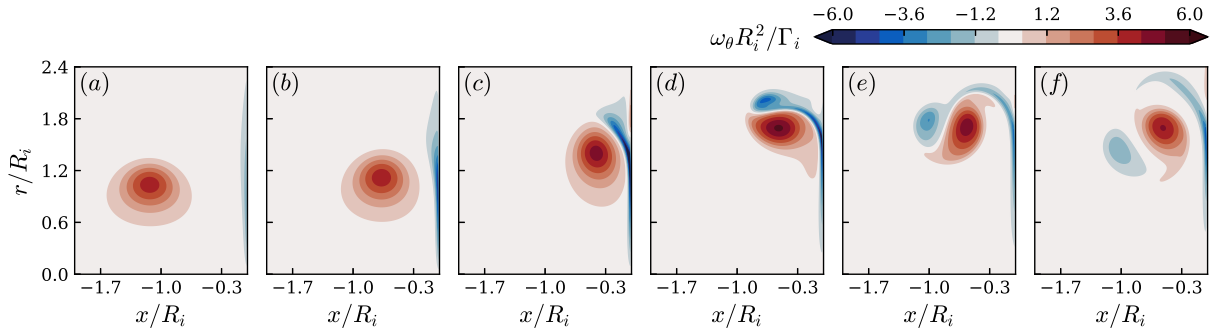

Figure 4.6: Vorticity evolution for $R_a/R_i = 0.0$ at Re = 2000, with an increase in time from (a) $t\Gamma_i/{R_i}^2 \approx 13.0$ to (f) $t\Gamma_i/{R_i}^2 \approx 25.9$ at an interval of $t\Gamma_i/{R_i}^2 \approx 2.6$.

induced as the vortex ring approaches the wall. Upon collision in Figure 4.6(c) and (d), the lower pressure vortex core imposes an adverse pressure gradient that leads to unsteady boundary layer separation. The separated boundary layer rolls into a secondary ring, which couples with the impinging ring and rebounds, as shown in Figure 4.6(d)-(f).

Figure 4.7 displays the evolution of the $R_a/R_i = 0.6$ case, which exhibits similar features to the $R_a/R_i = 0$ case, including boundary layer formation and separation (Figure 4.7(a)-(c)) and subsequent coupling with the incoming ring and rebound from the wall (Figure 4.7(d)-(f)). However, at the aperture, same-sign vorticity forms at the aperture

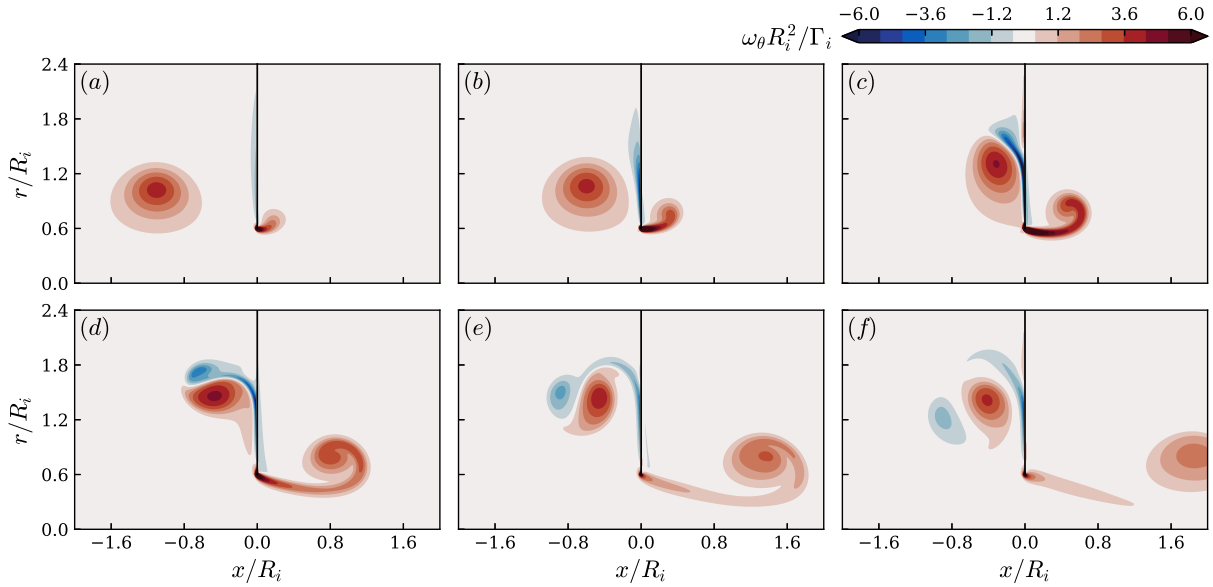

Figure 4.7: Vorticity evolution for $R_a/R_i = 0.6$ at Re = 2000, with an increase in time from (a) $t\Gamma_i/{R_i}^2 \approx 13.0$ to (f) $t\Gamma_i/{R_i}^2 \approx 25.9$ at an interval of $t\Gamma_i/{R_i}^2 \approx 2.6$. Corresponding movies are available in the supplementary materials.

edge as fluid is forced through the opening as the approaches, see Figure 4.7(a) and (b). The vortex-induced shear layer at the aperture tip spirals into a new vortex ring in a manner similar to vortex ring formation by a piston/cylinder generator [31] and discussed in Chapter 3.

To further explore the rebound dynamics, we consider the evolution of the total positive, Γ_p, and negative, Γ_n, circulations in the $x/R_i < 0$ half-plane in Figure 4.8. The circulations Γ_p and Γ_n are computed from Equation (4.1) with ω_θ filtered to include only positive and negative signed vorticity in the integration domain, respectively. Figure 4.8(a) shows the colliding vortex ring during its interaction. With no aperture (solid wall), circulation reduces through crossing-diffusion with the opposite-signed vorticity generated along the wall. As the aperture ratio increases, the amount of opposite-signed vorticity generated along the wall decreases, as shown by the evolution of Γ_n in Figure 4.8(b). Despite the

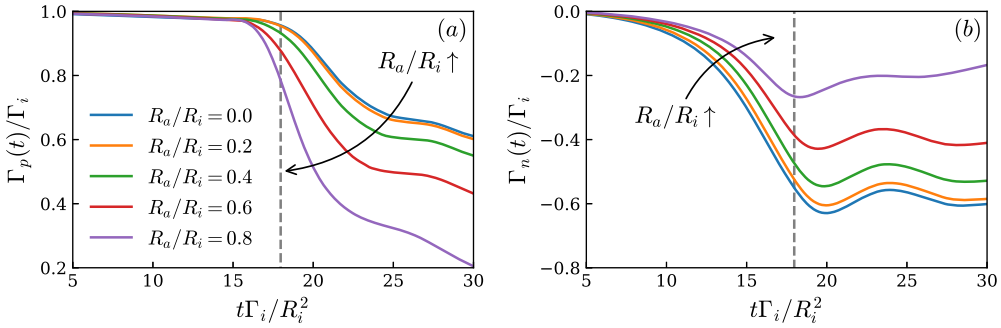

Figure 4.8: Circulation evolution of the (a) colliding, $\Gamma_p(t)$, and (b) secondary, $\Gamma_n(t)$, vortex rings for Re = 2000 throughout the interaction for $R_a/R_i = 0.0$ to 0.8. The dashed line indicates the time at which a ring would pass the $x/R_i = 0$ plane in the absence of a wall ($R_a/R_i = \infty$).

reduction in opposite-signed vorticity generation, the circulation loss of the incoming ring is more pronounced as the aperture ratio increases due to the direct vorticity transport though the aperture. The directly transported vorticity joins the new ring formed by the shear layer emanating from the aperture tip. As a consequence of the reduced circulation at larger apertures ratios, the vortex rebound is weakened, as shown by the primary vortex ring trajectories in Figure 4.9.

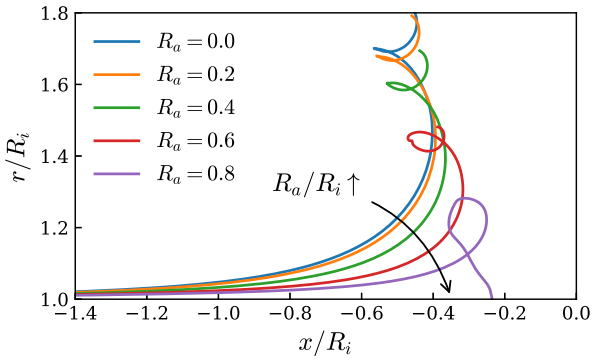

Figure 4.9: Trajectory of the primary vortex ring core for radius ratios in the range $R_a/R_i =$ 0.0 to 0.8 at an interval of 0.2 and Re = 2000.

Once the radius ratio reaches $R_a/R_i \approx 0.9$, so much of the colliding vortex ring passes though the aperture that the remaining ring is too weak to rebound, which marks the

upper limit of the impact regime.

4.2.2 Slip-through regime

When the aperture radius is larger than the incoming vortex ring, the ring will slip though the aperture instead of rebounding, as shown by the vorticity evolution for $R_a/R_i = 1.4$ in Figure 4.10. The vortex ring no longer induces an appreciable boundary layer on the

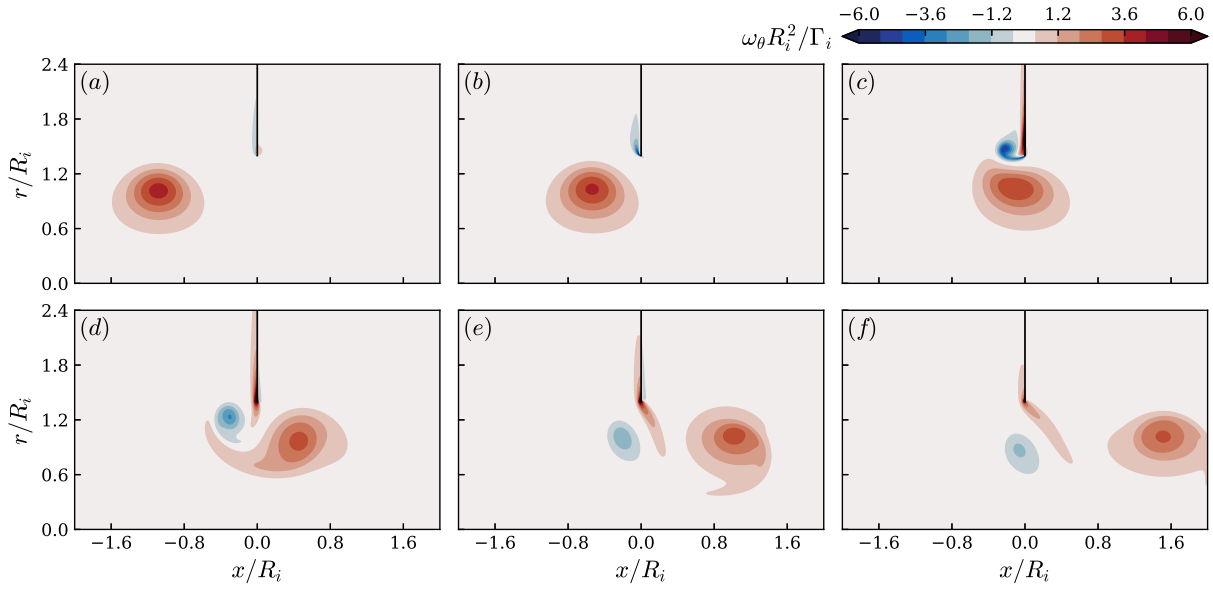

Figure 4.10: Vorticity evolution for $R_a/R_i = 1.4$ at Re = 2000, with an increase in time from (a) $t\Gamma_i/{R_i}^2 \approx 13.0$ to (f) $t\Gamma_i/{R_i}^2 \approx 25.9$ at an interval of $t\Gamma_i/{R_i}^2 \approx 2.6$. Corresponding movies are available in the supplementary materials.

facing plane, as displayed in Figure 4.10(a). The flow in the vicinity of the aperture edge due to the main ring is now in the retrograde direction, resulting in a shear layer of opposite signed vorticity moving upstream, see Figure 4.10(b) and (c). This vorticity rolls up into a new tip vortex of opposite sign to that generated in the impact regime, see Figure 4.10(c). This newly formed tip ring is drawn downstream by the passing ring, which is in turn deformed by its presence, as illustrated in Figure 4.10(d). Towards the end of the interaction, Figure 4.10(e) and (f), the passing vortex ring reorganizes itself and propagates away from the aperture.

For cases with even larger aperture ratio, the influence of the aperture continues to diminish. The opposed-signed tip vortex ring is produced until $R_a/R_i \approx 1.8$, but it does not interact with the passing ring to any meaningful degree for $R_a/R_i \gtrapprox 1.6$. Rather, the tip ring propagates upstream (in the negative x direction), while the primary ring passes with no major disturbance. For $R_a/R_i \gtrapprox 1.8$, the influence of the aperture is essentially negligible.

4.2.3 Vortex nozzle regime

The vortex nozzle regime ($0.9 \lessapprox R_a/R_i \lessapprox 1.3$) shares qualitative similarity with the slip-through regime in terms of vortex dynamics, as shown in Figure 4.11. The incoming

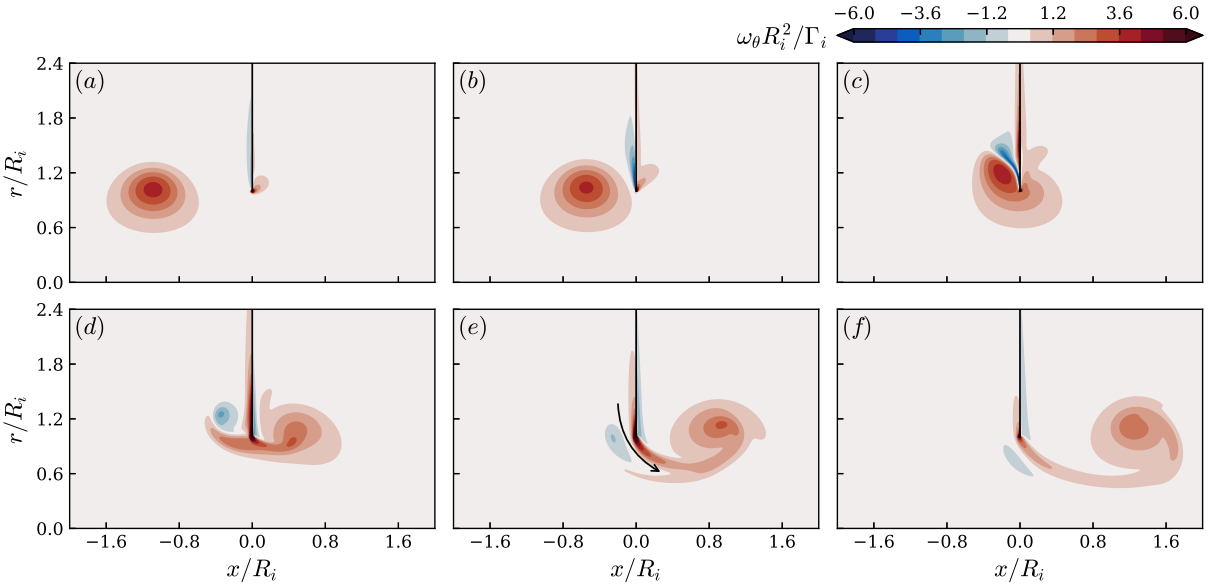

Figure 4.11: Vorticity evolution for $R_a/R_i = 1.0$ at Re = 2000, with an increase in time from (a) $t\Gamma_i/{R_i}^2 \approx 13.0$ to (f) $t\Gamma_i/{R_i}^2 \approx 25.9$ at an interval of $t\Gamma_i/{R_i}^2 \approx 2.6$. Corresponding movies are available in the supplementary materials.

vortex ring induces opposite signed boundary layer near the aperture tip (Figure 4.11(a) and (b)), that eventually separates when the colliding vortex ring is close to the aperture (Figure 4.11(c)). The secondary vortex ring does not rebound, but is rather pulled towards the aperture. The wall deforms the primary and secondary rings (Figure 4.11(d)]), both of which are pulled though the aperture (Figure 4.11(e)). The secondary ring also induces a

shear layer near the aperture edge that feeds back to the passing vortex ring. At the same time, the passing ring reorganizes its deformed core, similar to the spiraling of a vortex sheet during the formation process of a vortex ring [24, 33, 65]. After the interaction, the passing vortex re-spirals its core into a Gaussian-like distribution and continues to propagate onward (Figure 4.11(f)). The complex tip vortex dynamics for this aperture-to-ring size leads to interesting quantitative modifications to the passing ring, as discussed in the next section.

4.3 Passive enhancement of the hydrodynamic impulse

Figure 4.12 presents the final vortex ring impulse $I_f = I(t\Gamma_i/R_i \approx 39.1)$ computed from Equation (4.4) as a function of aperture-to-ring radius ratio for Re = 2000. The results

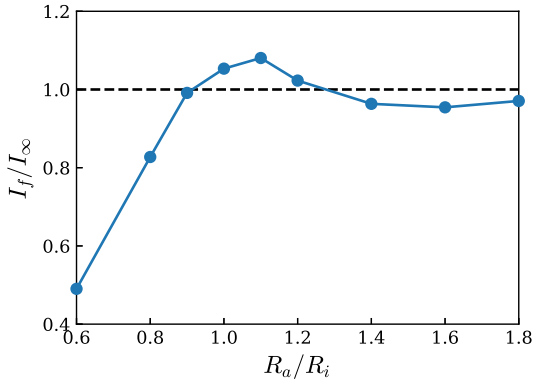

Figure 4.12: Final hydrodynamic impulse, I_f, of the passing vortex ring for various radius ratios, R_a/R_i, taken at $t\Gamma_i/{R_i}^2 \approx 39.1$ for Re = 2000. Radius and circulation are normalized by the baseline case of a freely advecting vortex ring ($R_a/R_i = \infty$) at the same time point.

are normalized by the baseline impulse, I_∞, of a vortex ring advecting through the domain in absence of a wall ($R_a/R_i = \infty$) at the same time point. In the impact and slip-through regimes ($R_a/R_i \lessapprox 0.9$ and $R_a/R_i \gtrapprox 1.3$, respectively), the final ring impulse is lower than that of a freely advecting ring due to losses associated with interaction with the wall and aperture tip, respectively. The normalized final impulse tends towards unity as R_a/R_i becomes large, as expected. Interestingly, when the ring radius is approximately the same

as the aperture radius, we observe impulse enhancement, which is the defining feature of the vortex nozzle regime introduced in Section 4.2. As seen in Figure 4.12, the vortex ring can increase its hydrodynamic impulse by more than 8% compared to a freely convecting vortex ring through this nozzle effect for Re = 2000, with the largest enhancement observed for $R_a/R_i = 1.1$.

To better understand the physics of the impulse enhancement, we consider Fraenkel's model of a vortex ring to express the impulse and energy [28, 94] given to second order by

$$I = \pi \Gamma R^2 \left[1 + \frac{3}{4} \left(\frac{R_c}{R} \right)^2 \right] \tag{4.6a}$$

$$E = \frac{1}{2} \Gamma^2 R \left[\ln \frac{8R}{R_c} - \frac{7}{4} + \frac{3}{8} \left(\frac{R_c}{R} \right)^2 \ln \frac{8R}{R_c} \right]. \tag{4.6b}$$

In the present simulations the final core-to-ring radius ratio (R_c/R) for the impulse enhancement cases differs by less than 2% from that of a freely advecting vortex, which accounts for at most 0.2% of the impulse variation and 1% of the energy variation based on Equation (4.6). Hence, we neglect the terms in square brackets in Equation (4.6) for the remainder of this discussion and focus only on the leading order changes due to variations in the primary variables Γ and R only.

Considering the first order terms of Equation (4.6), we can compare post-impact properties I_f and E_f with analogous properties for a free ring, yielding

$$\frac{I_f}{I_\infty} \approx \left(\frac{\Gamma_f}{\Gamma_\infty} \right) \left(\frac{R_f}{R_\infty} \right)^2 \tag{4.7a}$$

$$\frac{E_f}{E_\infty} \approx \left(\frac{\Gamma_f}{\Gamma_\infty} \right)^2 \left(\frac{R_f}{R_\infty} \right), \tag{4.7b}$$

which can be combined to give

$$\frac{I_f}{I_\infty} \approx \left(\frac{E_f}{E_\infty} \right)^{1/2} \left(\frac{R_f}{R_\infty} \right)^{3/2}. \tag{4.8}$$

Noting that the rigid wall does no work on the fluid, and the ring losses energy to vorticity production at the no-slip boundary during the interaction (Figure 4.11), then $E_f/E_\infty < 1$. Therefore, according to Equation (4.8), the observed impulse enhancement ($I_f/I_\infty > 1$) must coincide with an increase in ring radius ($R_f/R_\infty > 1$). Figure 4.13(a) shows that

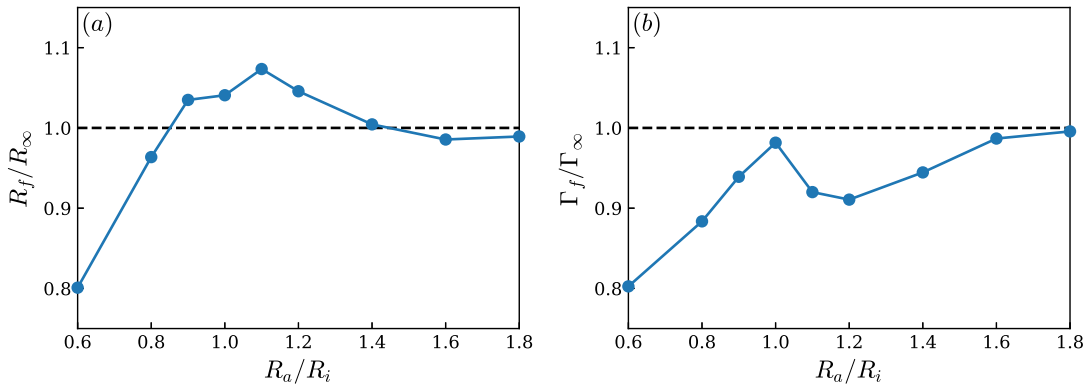

Figure 4.13: Final (a) radius, R_f, and (b) circulation, Γ_f, of the passing vortex ring for various radius ratios, R_a/R_i, taken at $t\Gamma_i/{R_i}^2 \approx 39.1$ for $\mathrm{Re} = 2000$. Impulse is normalized by the baseline case of a freely advecting vortex ring ($R_a/R_i = \infty$) at the same time point.

indeed the final ring radius, R_f, is larger than that of a freely convecting vortex ring in the vortex nozzle regime.

Furthermore, rearranging Equation (4.7) yields

$$\frac{I_f}{I_\infty} \approx \left(\frac{E_f}{E_\infty}\right)^2 \left(\frac{\Gamma_f}{\Gamma_\infty}\right)^{-3} \tag{4.9}$$

reveals that the impulse enhancement must be accompanied by a decrease in circulation ratio ($\Gamma_f/\Gamma_\infty < 1$). Figure 4.13(b) shows that the circulation of the vortex ring does indeed decrease through the interaction with the aperture, though the loss of circulation is somewhat mitigated in the vortex nozzle regime. The mechanisms behind this will be discussed in greater detail in Section 4.5.

4.3.1 Fluid entrainment

The volume of a vortex ring can be approximated with an ellipsoid with a semi-major axis that is proportional to the ring radius [94]. Thus, the radial expansion of the passing vortex ring observed in Figure 4.12(a) for the vortex nozzle regime implies that fluid entrainment occurs during the aperture interaction. That is, the mechanism of the impulse enhancement is the fluid entrainment process. To further explore the role of fluid entrainment in the impulse enhancement, we express the impulse in terms of ring volume, $\mathcal{V}$, and self-induced

velocity, U_s, as follows

$$I(t) = (1 + C_{am})\mathcal{V}(t)\ U_s(t) \tag{4.10}$$

where $C_{am} \approx 0.72$ is the constant added mass correction [19, 94, 96]. We note that C_{am} is purely dependent on the core to ring radius ratio, which is unaffected by the wall interaction in the vortex nozzle regime. Thus, it is reasonable to assume that C_{am} remains constant.

The convective velocities of the ring obtained from the simulations are illustrated in Figure 4.14(a). Except for large radius ratios, $U_f/U_\infty < 1$, indicating that the ring loses

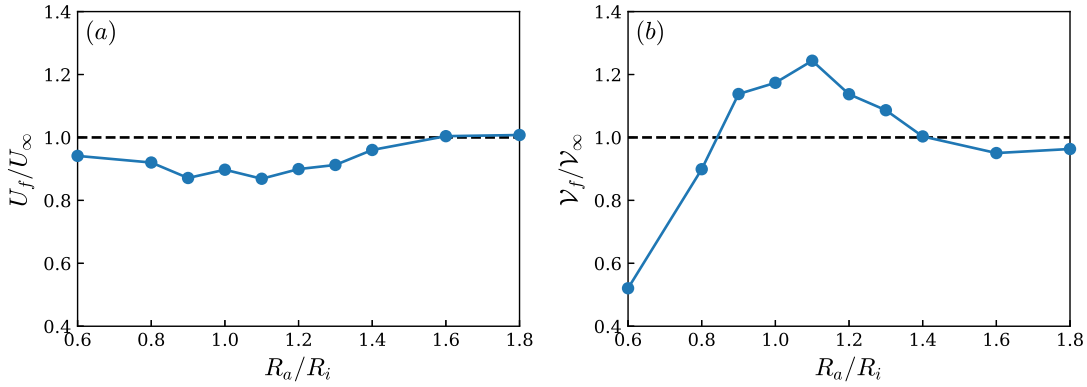

Figure 4.14: Final (a) velocity and (b) volume of the passing vortex ring, $\mathcal{V}_f$, versus radius ratio, R_a/R_i, taken at $t_f\Gamma_i/{R_i}^2 \approx 39.1$ for Re = 2000. Velocity and volume are normalized by the baseline case of a freely advecting vortex ring ($R_a/R_i = \infty$) at the same time point. Re = 2000 shown.

velocity during the wall interaction, consistent with the reduction in circulation and the rise in ring radius observed in Figure 4.13 [28, 94]. Therefore, the only way for the ring to gain impulse is for its volume to increase. This is supported by Figure 4.14(b), which shows a substantial increase of the passing vortex ring's volume in the vortex nozzle regime. The largest volume gain of 24% occurs at $R_a/R_i = 1.1$, which is the radius ratio that also exhibits the largest impulse enhancement.

Entrainment is visualized by seeding fluid along the front and back of the aperture wall with passive tracers at $t\Gamma_i/{R_i}^2 \approx 0$ as shown in Figure 4.15(a) and allowing them to passively advect until $t_f\Gamma_i/{R_i}^2 \approx 39.1$, with the final positions displayed in Figure 4.15(b). Solid black dots mark tracers that are ultimately entrained into the ring. The initial position of these black tracers indicate that the fluid near the front of the aperture ($0.9 < r/R_i < 1.5$) is entrained into the passing vortex ring during the collision. Comparing with

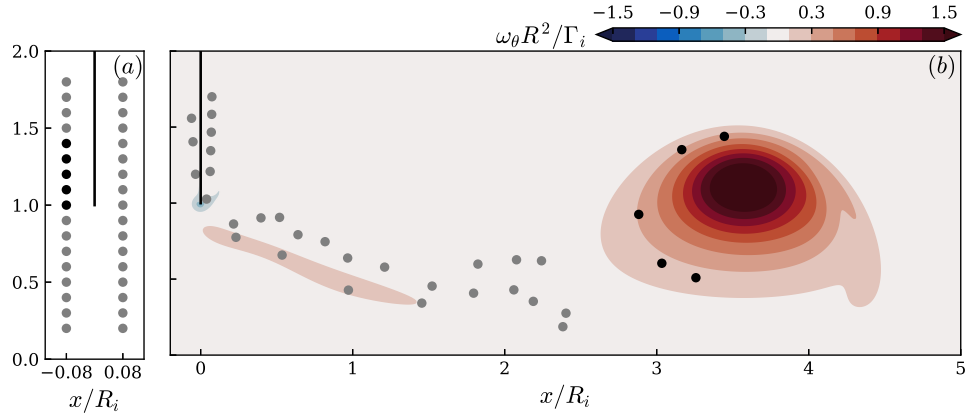

Figure 4.15: Fluid tracers at their (a) initial seeding position and (b) final locations at $t_f\Gamma_i/{R_i}^2 \approx 39.1$ for $R_a/R_i = 1.0$ and Re $= 2000$. Black circles indicate the tracers entrained into the vortex ring during collision.

the vorticity distribution in Figure 4.11, the tip vortex ring occupies the initial black tracer area during the collision, hinting at the tip vortex ring's role in the entrainment process.

To further explore the entrainment mechanism in relationship with the tip vortex ring, we display vorticity field snapshots and their corresponding experimental flow visualizations for $R_a/R_i = 1.2$ in Figure 4.16. This initial vortex ring is marked with fluorescent dye in the experiments (see Chapter 3 for further details) In Figure 4.16(a) and (d), region A illustrates the formation of the tip vortex ring. The lack of dye within the core of the tip ring shows that it comprises ambient fluid near the plate. In Figure 4.16(b) and (e), the tip vortex begins to drawn fluid away from the aperture wall and injects it towards the aperture, as shown by the arrows labeled B [see also Figure 4.11(e)]. Eventually, the passing vortex ring entrains the injected fluid, as shown by the fluid circled and labeled C in Figure 4.16(c) and (f). Such entrainment has previously been described by Dabiri and Gharib [20] during formation, wherein the vortex ring captures the fluid within the vortex ring "bubble". The sequence of events depicted in Figure 4.16 reveals that the tip vortex ring is the driving agent behind the fluid entrainment that enables the impulse amplification. The coupling between the tip vortex ring and the aperture wall creates a jet that feeds ambient fluid into the passing vortex ring.

A freely advecting vortex ring has zero net volumetric flux across a plane perpendicular to its path since it replaces the displaced volume by sweeping fluid from in front to behind the ring [19]. In the present case, the physical obstruction of the wall results in net positive

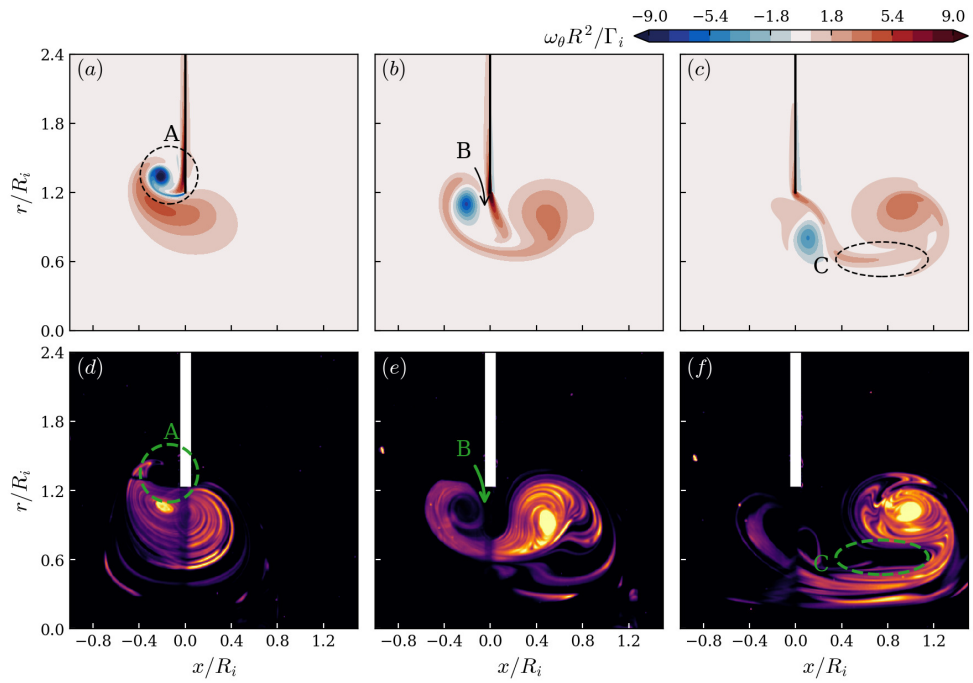

Figure 4.16: Snapshots of (a)-(c) vorticity field and (d)-(f) flow visualization of $R_a/R_i = 1.2$ at $\mathrm{Re} = 4000$. Columns correspond to $t\Gamma/R^2 \approx 1.80$, 20.2, and 22.5 from left to right.

mass flux through the aperture as the traveling ring forces fluid through the hole. Mass is conserved across the plane of the wall by virtue of retrograde flow beyond the extent of the finite expanse wall. Figure 4.17 presents the peak volumetric flow rate $Q_m = \max[Q(t)]$ through the aperture, which shows a net positive volumetric flux rate for all radius ratios.

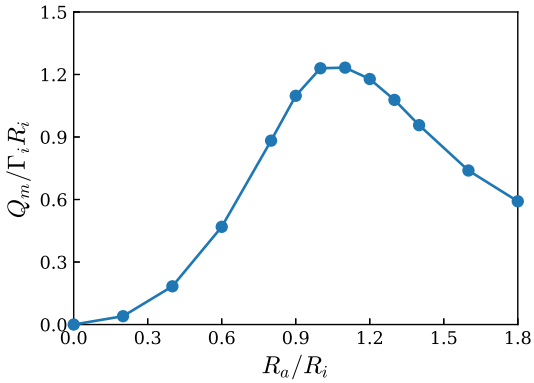

Figure 4.17: Peak volumetric flow rate, Q_m, for each radius ratio, R_a/R_i. Re = 2000 shown.

As shown in Figure 4.15(b), only the vortex nozzle range of radius ratios results in fluid entrainment into the passing vortex ring, which consequently exhibits the highest peak volumetric flow rate.

4.3.2 Source of impulse

Lastly we consider the source of the impulse in the "vortex nozzle", which is a conserved quantity. The observed net gain of hydrodynamic impulse in the system requires an external source. Consider the control volume shown in Figure 4.1, with its boundary enclosing the entire infinite fluid domain with a branch cut employed along the wall. The external source must come from forces imposed on the fluid by the wall. Figures 4.18 and 4.19 show the temporal evolution of the pressure field and the reaction force $F_a(t)$ in the structure, respectively for the $R_a/R_i = 1.0$ case. The pressure initially pulls the structure to the left as the vortex ring approaches (Figure 4.18(a)), then to the right after the ring passes through, with the post-interaction pressure field exhibiting less load on the structure due to the reduced ring circulation (Figure 4.18(c)). The reaction force in the structure (Figure 4.19), which is equivalent to the force the structure applies on the fluid shows a net positive force (in the x-direction) applied to the fluid through the interaction. Therefore,

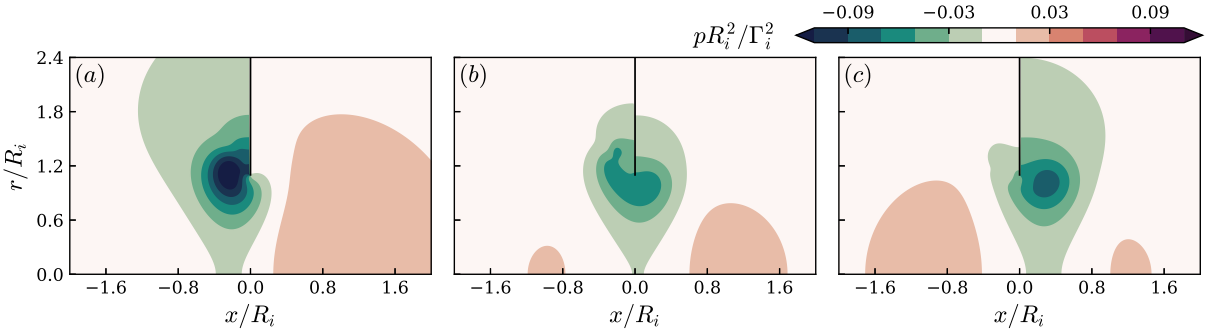

Figure 4.18: Pressure distribution for $R_a/R_i = 1.1$, taken at $t\Gamma_i/R_i{}^2 \approx 17.8$, 18.8, and 19.9 from left to right. Re = 2000 shown. Re = 2000 shown.

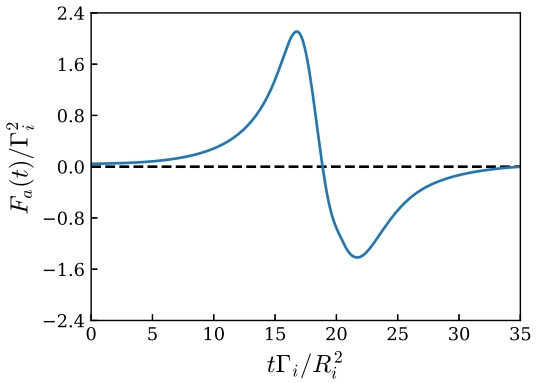

Figure 4.19: Reaction force histories, $F_a(t)$, for $R_a/R_i = 1.0$.

the momentum balance for the control volume can be written as

$$I_i + I_a = I_i + \int_{t_i}^{t_f} F_a \, \mathrm{d}t = I_i - 2\pi \int_{t_i}^{t_f} \int_{R_a}^{\infty} \Delta p \; r \; \mathrm{d}r \; \mathrm{d}t = I_f + I_s \tag{4.11}$$

which includes a net positive average reaction force due to the pressure loading applied during the interaction for impulse enhancement. Note that I_s stands for the total impulse of secondary vortices, such as shear layers and the tip ring shown in Figure 4.10(f) and I_a represents the added impulse. The impulse gain for the case shown in Figures 4.18 and 4.19 is $I_a/\Gamma_i {R_i}^2 = 2.16$.

4.4 Structural loading

In this section, we will further expand the discussion in the last sub-section on the structural loading to the entire R_a/R_i range. Snapshots of the pressure field for the solid wall ($R_a/R_i = 0.0$) and impact regime ($R_a/R_i = 0.6$) are shown in Figure 4.20. Impact with

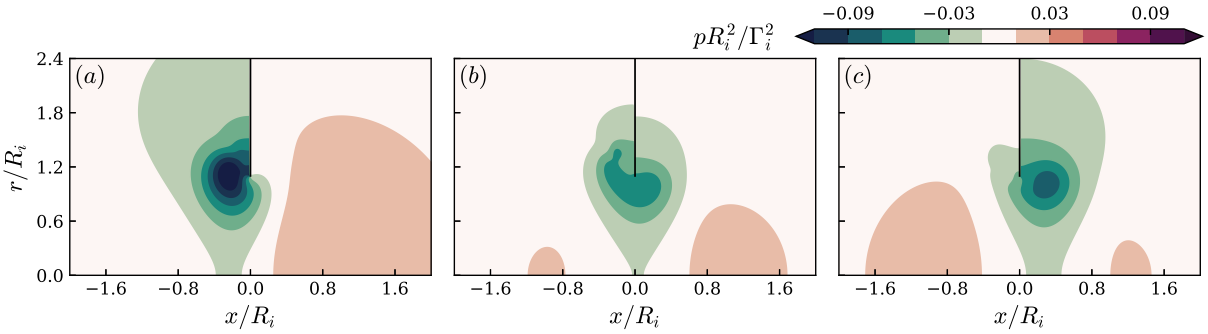

Figure 4.20: Pressure distribution for (a) $R_a/R_i = 0.0$ at $t\Gamma_i/{R_i}^2 \approx 16.4$, and (b)(c) $R_a/R_i = 0.6$ at $t\Gamma_i/{R_i}^2 \approx 16.4$, 19.0, respectively. Re = 2000 shown.

a solid wall is a limiting case for the structural loading. As the ring collides, the forward flow at the central axis hits the wall, forming a high pressure stagnation zone at the center, which balances out the low pressure from the vortex core (Figure 4.20(a)). Thus, almost no net force is exerted on the structure. On the other hand, the impact regime exhibits a similar forcing pattern to the vortex nozzle regime discussed in the previous section. The aperture opening relieves the high stagnation pressure seen in the solid wall case, allowing the low pressure core to dominate and pull on the plate initially (Figure 4.20(b)). Once the

new ring formed at the aperture gains sufficient strength, its influence begins to show as it pulls on the plate in the positive x direction, while the impinging ring influence reduces as it rebounds away (Figure 4.20(c)). For the vortex nozzle and slip-though regimes, the low pressure vortex core becomes the only contributor to the structural loading, as shown in Figure 4.18, where it pulls at first in the negative then positive x direction as it passes though the aperture. As the aperture becomes larger and larger, the pressure loading from the passing vortex ring diminishes.

As such, the structural loading, $F_a(t)$, exhibits the same pattern regardless of the regime, excepting the case of a solid wall with no aperture ($R_a/R_i = 0.0$), as shown in Figure 4.21(a). The related added impulse, I_a, is shown in Figure 4.21(b) for all cases.

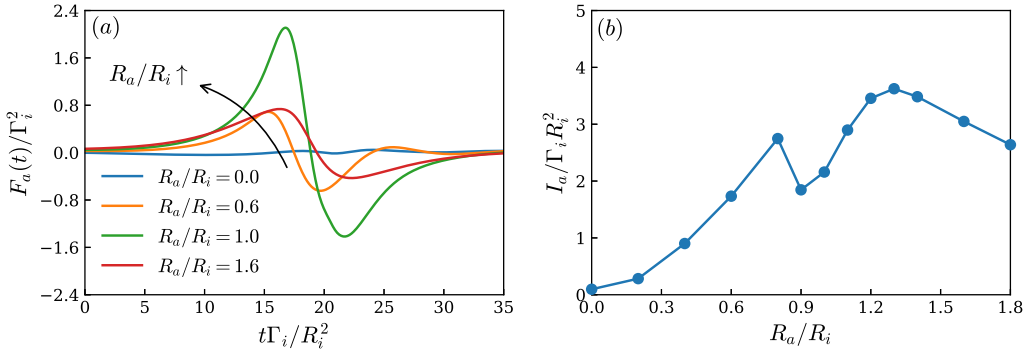

Figure 4.21: Typical (a) pressure force histories, $F_a(t)$, and (b) added impulse I_a as a function of radius ratio, R_a/R_i. Re = 2000 shown.

The figure shows that the added impulse is positive in every cases, albeit small for R_a/R_i approaching zero, consistent with the small net force on the wall suggested by due Figure 4.21(a). This is not to say, however, that the colliding vortex ring does not experience significant impulse gain. As shown by the trajectories of the colliding vortex ring (Figure 4.4), the colliding ring undergoes a noticeable radial expansion, which corresponds to an increases of impulse ($I \propto \Gamma R^2$, see the beginning of Section 4.3). However, this impulse gain is balanced out by the production of secondary vortices, which have opposing impulse.

As R_a/R_i increases, so too does the added impulse due to the mitigation of the secondary vorticity production. In the vortex nozzle region there is a sudden drop in the added impulse, which then rises again outside of this region. We see that I_a continues to rise after $R_a/R_i = 1.2$, but the impulse gain for the passing ring begins to diminish (see Figure 4.12). This is a result of the aperture tip vortex ring being unable to feed into the

passing ring; instead, it creates secondary shear layers. For the large R_a/R_i, the influence of the aperture begins to drop off, and hence a decrease in the added impulse is observed.

Lastly, to compare the unsteady loading between cases, we plot the peak-to-peak force, $F_{ptp} = \max[F_a(t)] - \min[F_a(t)]$, against the radius ratio in Figure 4.22. As expected, the

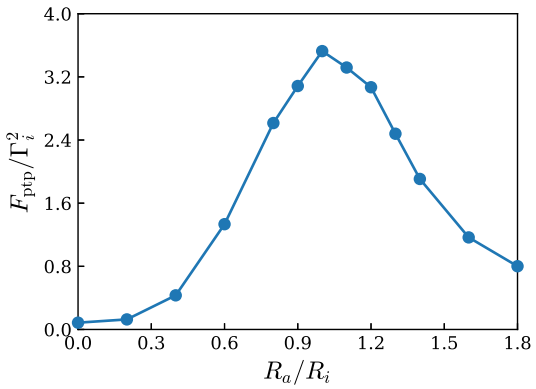

Figure 4.22: The peak-to-peak force, F_{ptp} as a function of radius ratio, R_a/R_i. Re = 2000 shown.

unsteady loading maximizes in the vortex nozzle regime. This leads to an unsteady force amplitude that is orders of magnitude higher than for the solid wall and four times larger than the slip through regime with $R_a/R_i = 1.8$. This highlights the criticality of vortex positioning for applications such as sensing/energy harvesting with smart materials, where unsteady loading needs to be maximized [36].

4.5 Vorticity production

The final circulation of the vortex ring, Γ_f, is plotted against the radius ratio in Figure 4.13(b), normalized by the $R_a/R_i = \infty$ case to eliminate circulation changes from diffusion over time. The circulation rises to a local maximum at $R_a/R_i = 1.0$ then dips to a local minimum at $R_a/R_i = 1.2$, marking the approximate boundary of the vortex nozzle regime. At higher aperture radius ratios the circulation tends towards the freely advecting vortex case as the influence of the aperture diminishes.

The circulation of the passing vortex ring at $R_a/R_i = 1.0$ has approximately the same value as that of the $R_a/R_i = 1.6$ case, where the influence of the aperture is almost negligible. The passing vortex ring in the $R_a/R_i = 1.0$ case maintains its circulation despite

significant transformation and interaction, as illustrated in Figure 4.11. The energy of a vortex ring is proportional to the square of the circulation, see Equation (4.6b), and thus the minimal loss of circulation for $R_a/R_i = 1.0$ also implies that direct collision with the aperture tip does not consume as much energy. This begs the question, why does the passing vortex ring in the $R_a/R_i = 1.0$ case lose so little circulation despite significant disruption during impact with the aperture?

To address this question, we investigate vorticity production. As discussed by Morton [67], the passing ring can only lose circulation via cross-diffusion with opposite-signed vorticity, which in this case, must be induced at the wall. Following Chu *et al.* [17], the vorticity production can be quantified by the enstrophy history $\mathcal{E}(t)$ in the fluid domain S, which is computed as

$$\mathcal{E}(t) = \pi \int_S {\omega_\theta}^2(x, r, t)\ r\ \mathrm{d}x\ \mathrm{d}r. \tag{4.12}$$

Examples of the enstrophy history for the case of $R_a/R_i = 0.8$, 1.0 and 1.2 are shown in Figure 4.23(a). Enstrophy generally decreases in time due to diffusion, but at the moment of collision, it spikes to a peak due to vorticity production. To compare between cases, the

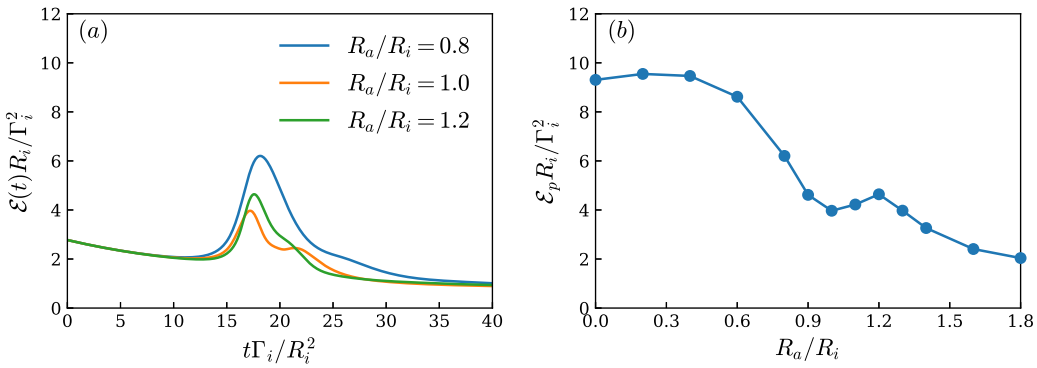

Figure 4.23: Examples of (a) enstrophy history and (b) peak enstrophy during collision, $\mathcal{E}_p$, for each radius ratio, R_a/R_i. Re = 2000 shown.

peak enstrophy ($\mathcal{E}_p$) reached during collision for each case is presented in Figure 4.23(b). The plot shows that vorticity production is the highest at the lower ranges of R_a/R_i due to the large amount of induced vorticity and vortex stretching generated during collision of the vortex ring with the wall [18]. At high radius ratios, the peak enstrophy tapers off because of the diminishing induced vorticity on the wall and at the aperture tip.

Local extrema are observed for $R_a/R_i = 1.0$ and $R_a/R_i = 1.2$ that correlate well with the local extrema in the final vortex ring circulation in Figure 4.13(b), showing that

the circulation variation of the passing vortex ring is linked to vorticity production, and the subsequent cross-diffusion. The drop in vorticity production at $R_a/R_i = 1.0$ and the subsequent peak at $R_a/R_i = 1.2$ results from regions of the vortex core colliding with the aperture tip. Unlike in collision with a solid wall where the vortex core remains relatively "protected" and intact, the inner region of the passing vortex ring directly interacts with the aperture tip in this range of radius ratios. The center of a viscous vortex core has the lowest velocity and is surrounded by a high-velocity bell. For a ring with a similar radius as the aperture, the low-velocity region envelops the aperture tip as it slips by, while the fluid in the high-velocity bell simply flows around, thus minimizing opposite-sign vorticity production. If the aperture is slightly bigger than the ring radius, such as the $R_a/R_i = 1.2$ case, the high-velocity bell interacts with the aperture tip directly and creates a strong shear layer resulting in increased opposite-sign vorticity production. This is visualized in Figure 4.24 where both the induced vorticity at the surface and the tip are lower for

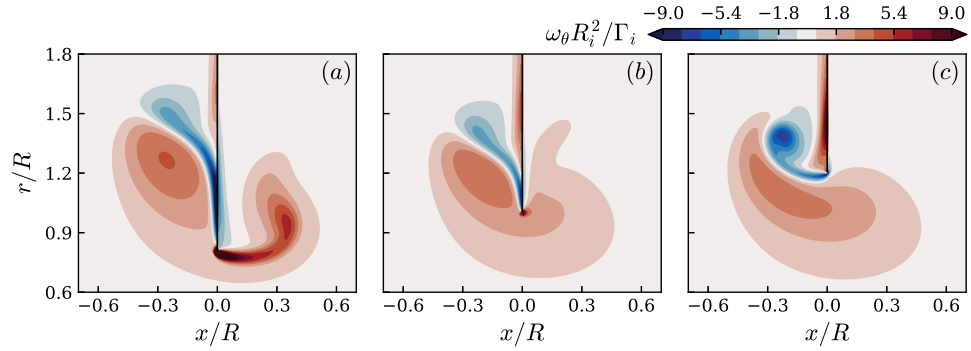

Figure 4.24: Zoomed view of the vorticity field near the aperture tip for the cases of (a) $R_a/R_i = 0.8$, (b) 1.0 and (c) 1.2 at $t\Gamma_i/{R_i}^2 \approx 18.5$. Re = 2000 is shown.

$R_a/R_i = 1.0$ than $R_a/R_i = 0.8$ and 1.2.

In summary, the velocity distribution of a viscous vortex core plays a critical role during collision with a sharp structural tip, because the partial collision exposes the inner core to the solid boundary. This differs from the classical vortex-wall interaction, wherein the vortex rebound protects the vortex core from interacting with the wall.

4.6 Influence of Reynolds number

Lastly, we touch upon is the influence of the Reynolds number. Figure 4.25 compares the vorticity snapshots at the moment of impact ($t\Gamma/R^2 = 19.2$ and 17.7 for Re = 1000 and 2000, respectively). Despite considerable differences in vortex ring strength due to viscous

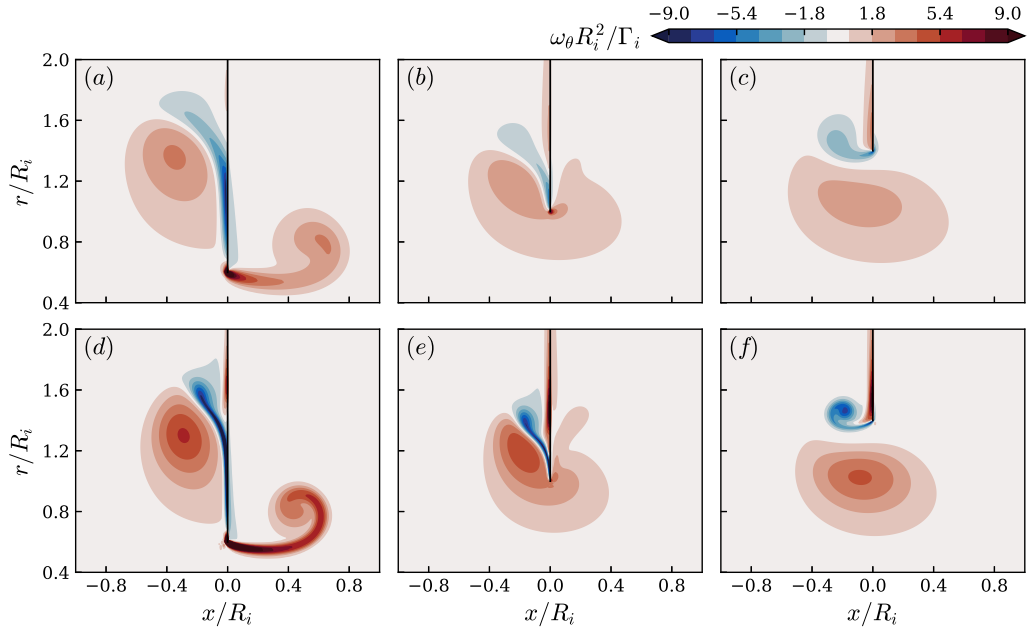

Figure 4.25: Vorticity fields for Re = 1000 at $t\Gamma/R^2 = 19.2$ and 3000 at $t\Gamma/R^2 = 17.7$ are shown on the first and second rows, respectively. Radius ratio $R_a/R_i = 0.6$, 1.0, and 1.4 are displayed in the columns from left to right, respectively.

diffusion during approach towards the wall, the features remain near identical. The weak Reynolds number dependence agrees with the literature on the classical vortex ring/dipole - wall interactions [80, 81].

The impulse enhancement follows the same trend as shown in Figure 4.25(a), which presents the final vortex ring impulse as a function of radius ratio for Re = 1000, 2000, and 3000. However, the impulse enhancement is observed for a broader range of radius ratios for higher Reynolds numbers, likely a result of the reduced losses during the collision as the viscous effect weakens. In addition, the impulse enhancement increases with increasing Reynolds numbers, with 4% enhancement observed for Re = 1000 and 11% for Re = 3000. To further examine the Reynolds number influence on the vortex nozzle effect, we

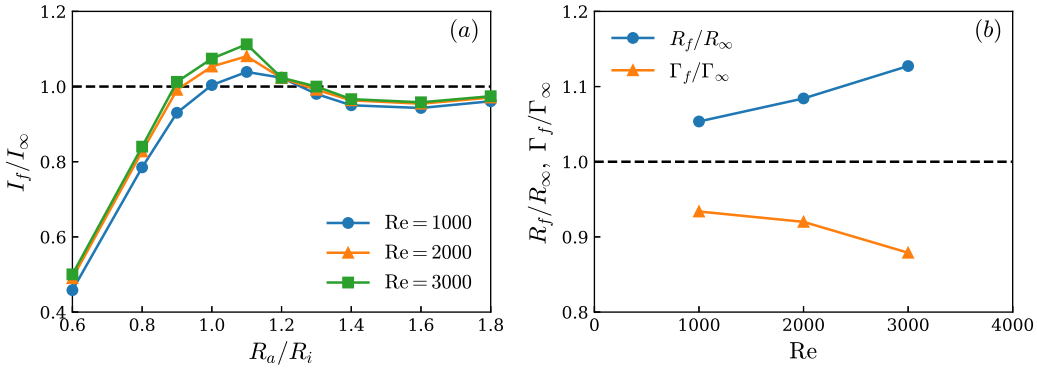

Figure 4.26: Reynolds number comparisons of the final vortex ring (a) impulse I_f at all radius ratio, and (b) radius R_f and circulation Γ_f at $R_a/R_i = 1.1$. Values of Re = 1000, 2000, and 3000 are taken at $t\Gamma/R^2 = 42.3$, 39.1 and 38.0, respectively.

compare the primary vortex ring properties (ring radius and circulation) at $R_a/R_i = 1.1$ in Figure 4.26(b). To no surprise, the final ring radius is higher due to the improved vortex nozzle effect, which entrains extra fluid to expand the ring radius. On the other hand, the drop in circulation appears to be counter-intuitive, since the lower circulation suggests higher losses despite the reduced effect viscosity. However, our analysis in Section 4.3 shows that for the energy to be at best conserved, the circulation must drop in order for the impulse to increase (see Equation (4.9)). Hence, the circulation loss is a trade-off of the improved vortex nozzle at higher Reynolds numbers. Hence, the vortex nozzle is a robust feature during the collision of a vortex ring with an aperture of a similar size over the Reynolds numbers investigated herein.

4.7 Conclusion

The problem of a viscous vortex ring colliding with a co-axial aperture was explored numerically over a range of aperture-to-ring radius ratios. The vortex dynamics are classified into three regimes: impact, vortex nozzle, and slip-through, based upon the primary event experienced by the vortex ring. When the aperture is smaller than the ring radius, the portion of the vortex ring that impacts the wall exhibits the classical vortex rebound action. When the aperture is larger than the ring it slips though the aperture, potentially undergoing some core deformation due to the influence of the tip. The most interesting phenomenon occurs when the ring radius is approximately the same as that of the aper-

ture. In this case, the passing vortex ring experiences hydrodynamic impulse enhancement of up to 4%, 8% and 11% respectively for Re = 1000, 2000 and 3000 when compared to a freely advecting ring. The impulse enhancement is the result of fluid entrainment during the collision, wherein the passing vortex ring gains considerable volume (mass). Whereas a traditional jet nozzle gains momentum through fluid acceleration, the vortex nozzle increases momentum through mass accumulation from fluid entrainment. Because of the fluid entrainment, the geometric constraint actually enhances the fluid transport across the aperture. The source of the impulse is the structural reaction force, which counters the pressure loading bias created by the passing vortex ring. The impulse enhancement is also attributed to the relatively smaller reduction in circulation that arises due to the details of the interaction of the vortex core with the aperture edge. Upon collision, the slow moving fluid at the centre of the vortex core envelops the aperture tip, allowing high velocity fluid to move around the structure without generating significant opposite-sign vorticity. Reduced production of opposing vorticity weakens the cross-diffusion during the collision, thus allowing the passing vortex ring to maintain nearly all of its circulation. Reduced vorticity production also results in low enstrophy which correlates with low energy loss. Thus, the collision consumes little energy from the passing vortex ring.

The reported results in this article highlight the basic behaviour of vortices colliding with a thin plate tip, which could aid the understanding in engineering applications that employ thin plates, such as smart material sensing/energy harvesting [36, 85]. More importantly, the current interpretation of structural loading from vortex motions are based on the hydrodynamic impulse term in Equation (4.3), which on the surface, breaks down two mechanisms, namely circulation and trajectory modifications during active vortex creation and destruction [103, 2, 48]. Outside of the formation phase, fluid entrainment was thought to be only a consequence of diffusion, which brings no gain in impulse [20]. However, our curated scenario exposes the hidden mechanism of passive (without energy input) fluid entrainment in sacrifice of circulation, which introduces noticeable impulse gains for vortices, similar to a jet nozzle.

Chapter 5

The influence of collision angle for viscous vortex reconnection[1]

To address the proposed questions regarding the role of pyramid stretching and collision angle for viscous vortex reconnection, we seek to re-evaluate the process by considering the collision of thick core vortex rings at various collision angles. The chapter is organized as follows: Section 5.1 outlines the problem formulation and numerical setup; Section 5.2 provides an overview of the influence of collision angle on vortex reconnection; Section 5.3 explores the details of the vortex threads during reconnection; and Section 5.5 summarizes the major findings of this chapter.

5.1 Problem statement

Herein, we numerically explore the influence of collision angle on the viscous reconnection process. There are three primary initial condition configurations in the studies of the fundamental vortex reconnection process: orthogonal [111, 7]; anti-parallel [42, 39, 53]; and two-ring configurations [47, 46]. It is well known that vortex reconnection is a universal phenomenon, with a similar process occurring regardless of initial condition [111, 57, 109, 46, 7, 45, 6]. However, for the goal of investigating collision angle effects, the choice of initial condition can greatly simplify the analysis. Hence, deliberate consideration regarding the initial condition are required to isolate the influence of the collision angle.

[1]This work has been accepted for Physics of Fluids with me and my Ph.D. advisor Sean D. Peterson as co-authors. I was responsible for performing the simulation, analyzing the results and writing of the manuscript. Professor Peterson provided guidance for the study and edits for the manuscript.

First, the orthogonal vortex tube configurations are commonly employed to examine the impact of asymmetry on vortex reconnection [111, 7]. Studies have shown that a pair of orthogonal vortex tubes undergo re-orientation that locally aligns the colliding vortices into an anti-parallel configuration prior to collision. The re-orientation process precludes control of the collision angle and is hence rejected from this study.

The anti-parallel configuration provides indirect control over the collision angle by adjusting the ratio between the perturbation amplitude and the separation distance (see Figure 5.1). However, there are two major shortcomings that render it unsuitable for

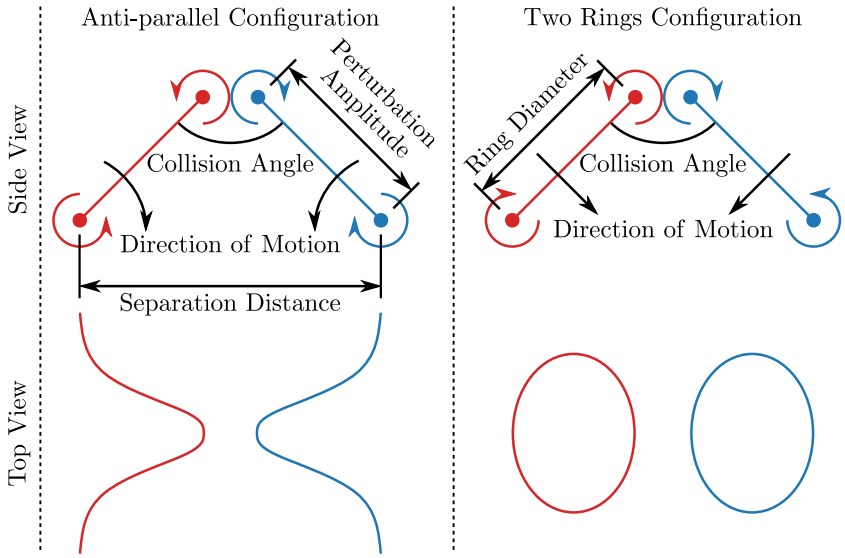

Figure 5.1: Anti-parallel and two rings initial conditions for the numerical investigation of the vortex reconnection.

this study. First, the perturbation rotates around the axis of the unperturbed vortex tubes, which alters the collision angle continuously during its approach, making it difficult to define an exact angle at the moment of collision. Second, the curvature at the peak of the perturbation will also be altered by the change in amplitude (smaller amplitude corresponds to a flatter peak). From the thin filament model of the pyramid process [62, 63], the local curvature plays a critical role in the kinematics during pyramid formation. Hence, the influence of collision angle can not be isolated from the curvature effect for this configuration.

The two ring configuration, shown in Figure 5.1, provides direct control over the collision angle without affecting spanwise curvature. However, it is not without shortcomings. As

mentioned previously, a change in reconnection completeness with respect to collision angle was observed, which Kida *et al.* attributed to the secondary motion induced by the rest of the vortex ring [46]. They reported that the remainder of the vortex ring undergoes a major distortion upon collision, which come in contact with the reconnection threads and enhances the reconnection completeness. However, the reported secondary motion is unique to the two ring configuration and does not apply to other scenarios. Furthermore, the distorted vortex rings undergo their own vortex tilting and stretching which contribute to the evolution of various global quantities critical to the analysis of vortex reconnection, making it difficult to isolate the effect of reconnection alone from the quantitative data.

Herein we opt to employ the vortex ring configuration because of its ease in defining and adjusting the collision angle. We impose an additional symmetry condition by employing a circular array of vortex rings to prevent secondary flow interactions in the reconnection region [34]. Global quantities are computed over the sub-divided symmetrical domain only, reducing ambiguity over changes from secondary motions unrelated to the reconnection process. We stress that the goal of our investigation is to examine the fundamental process of vortex reconnection with a focus on the role of collision angle, not the interaction of symmetrically aligned vortex rings. The additional imposed symmetry is to eliminate the secondary motions that are specific to the two ring configuration. By eliminating the two-ring specific secondary motion, the results can be more universally referenced as a fundamental behaviour of viscous vortex reconnection.

5.1.1 Simulation setup

In this sub-section, we details the setup of the symmetrical collisions between thick core vortex rings. Figure 5.2 presents a schematic of the collision angle $\theta = 90^\circ$ case as an exemplar. The collision angle (θ) can be altered by changing the number of rings (N_r). The origin of the domain is defined as the intersection of the initial axes of propagation of all the rings; the xy plane contains the initial propagation axes and thus bisects all of the vortex rings, with the z-axis forming a right-handed coordinate system (out of the page in Figure 5.2).

The initial vortex rings have equal circulation Γ, ring radius R, core radius R_c, and Reynolds number $\mathrm{Re} = \Gamma/\nu$, where ν is the kinematic viscosity. For the remainder of the article, the length scale R and time scale R^2/Γ are employed for non-dimensionalization, unless otherwise noted. The vorticity within the vortex core is initialized with a circular Gaussian distribution, consistent with the recent studies of similar topics [62, 63, 107, 108]. However, the circular Gaussian distribution is not a steady solution for thick core vortex

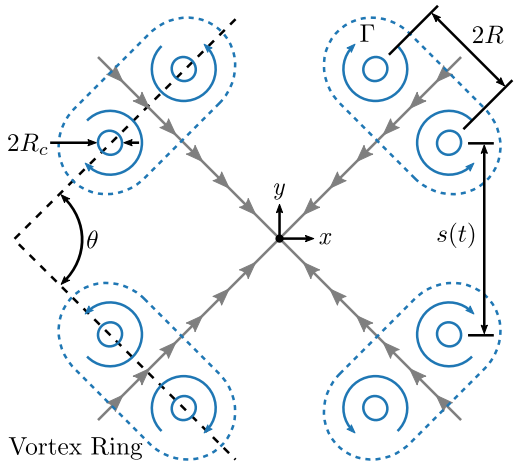

Figure 5.2: Top view schematic of the collision angle $\theta = 90°$ configuration.

rings, for which a realistic core has a more elliptical shape [28, 76]. Therefore, the initial circular core requires a transition phase in order to reach steady state. To ensure that the core transition does not interfere with the reconnection process, the simulations for each collision angle case were initialized with a Gaussian core distribution and allowed to evolve until the cores reached a steady state and then mapped to the actual simulation domain.

The separation distance $s(t)$ is defined as the shortest distance between the cores of the colliding vortices as shown in Figure 5.2. We define the position of a vortex core as the location of the peak vorticity within it. To further improve the precision of the vortex position (limited by grid size), we performed sub-grid interpolation by locally fitting a bi-variable Gaussian distribution around the 5×5 local grid points around the peak vorticity within the vortex core then used the peak of the fit to locate the vortex position.

Regarding the initial positioning of the vortex rings, we employ a different strategy from the study of Kida *et al.* [46]. In their study, the vortex rings are placed at a constant initial separation distance $s(t = 0)$ regardless of collision angle. However, the vortex rings are converging towards each other at different rates depending on their collision angle ($\propto \cos(\theta/2)$). To address this difference in the approach time scale, we instead use an initial separation distance that varies based on the collision angle such that the collision initiation time is the same for all cases. For a thin vortex core this would simply require scaling the initial separation distance by $\cos(\theta/2)$. It is further complicated, however, by the thick elliptical vortex core, which adds an angle-dependent offset, since vortex reconnection initiates upon core perimeter contact, not the center. Since there is no clear definition for the moment of contact due to the continuous vorticity distribution, we instead fine-tuned

the initial position such that each collision angle case has the same reconnection initiation time, such that the colliding vortices retain their initial circulation until $t \approx 5$ (to be discussed in Section 5.2.3, see Figure 5.8). The initial separation distance $s(t = 0)$ selected for our simulations is plotted in Figure 5.3. As expected, the initial separation distance

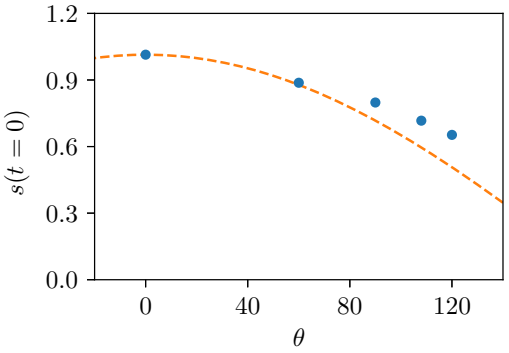

Figure 5.3: Initial separation distance $s(t = 0)$ (blue dots) with respect to the collision angle θ. Orange dashed line represents the trend of $\cos(\theta)/2$.

follows the trend of $\cos(\theta)/2$ at low collision angle, but deviates at high angles because of the vortex core offset.

For the parametric study, we employed vortex rings with core-to-ring radius ratio of $R_c/R = 0.25$ at $\mathrm{Re} = 500$, 1000, 2000, and 3000. For each Reynolds number, simulations with $N_r = 2$, 3, 4, 5, and 6 were performed, corresponding to $\theta = 0°$, 60°, 90°, 108°, and 120°, respectively (see Figure 5.4). As previously mentioned, we restrict our analysis to

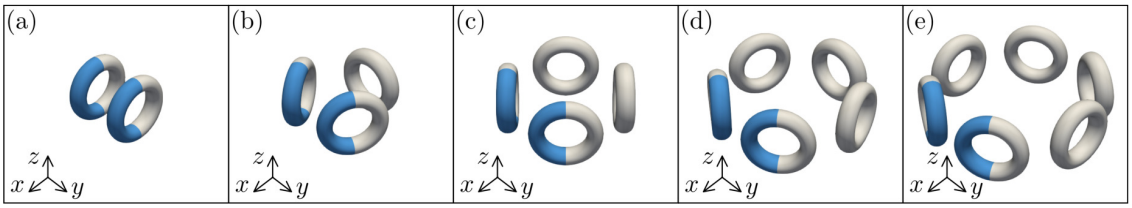

Figure 5.4: Vorticity isosurfaces of $|\boldsymbol{\omega}| = 1$ for the initial conditions. Collision angles of $\theta = 0°$, 60°, 90°, 108° and 120° shown from (a) to (e), respectively. Regions of interest are highlighted in blue.

one of the collision zones by exploiting the symmetry of the problem, as highlighted by

the blue isosurfaces in Figure 5.4. Following Hussain and Duraisamy [39], the mechanisms of viscous vortex reconnection are explored primarily via two key planes: the cutting (xy) plane and the reconnection (xz) plane, shown schematically in Figure 5.5.

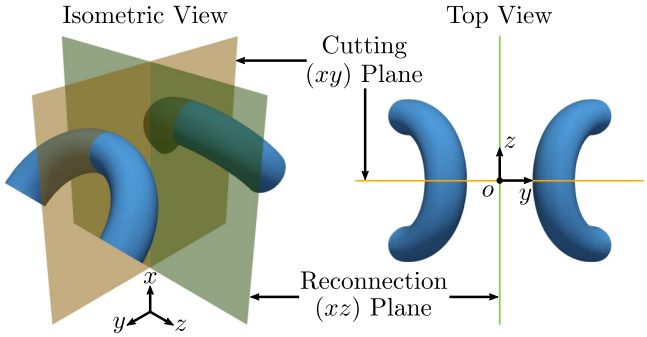

Figure 5.5: Schematics of the cutting (xy) and reconnecting (xz) planes.

5.1.2 Numerical Scheme

The Navier-Stokes equation in the form

$$\frac{\mathrm{d}\boldsymbol{u}_{\boldsymbol{k}}}{\mathrm{d}t} = (\boldsymbol{u}\times\boldsymbol{\omega})_{\boldsymbol{k}} - \nu|\boldsymbol{k}|^2\boldsymbol{u}_{\boldsymbol{k}} - \boldsymbol{k}\frac{\boldsymbol{k}\cdot(\boldsymbol{u}\times\boldsymbol{\omega})_{\boldsymbol{k}}}{|\boldsymbol{k}|^2} \tag{5.1}$$

are solved with an in-house pseudo-spectral code in a triple periodic domain. Herein, $\boldsymbol{u}$, $\boldsymbol{\omega}$, $\boldsymbol{k}$, and subscript $\boldsymbol{k}$ are the velocity vector, vorticity vector, spectral space vectors, and the Fourier coefficients of a vector field, respectively. Time-stepping is implemented with the low-storage third-order Runge-Kutta scheme. The standard 2/3-rule is applied to prevent aliasing error.

The domain sizes $(x,\ y,\ z)$ are $(16R,\ 8R,\ 16R)$ for $\theta = 0°$, and $(12R,\ 12R,\ 16R)$ for all other collision angles. The mesh size and time step used for each Reynolds number are listed in Table 5.1, which are based upon a grid convergence study for $\theta = 120°$ (as it exhibits the highest vorticity amplification). The mesh was considered to be converged when all global and local quantities of interest (*e.g.*, maximum vorticity) varied by less than 1% compared to the next lower resolution simulation. For further validation, we compared our results with the experimental study of three colliding rings [34], as shown in the Appendix B.

Reynolds number	Mesh size	Time step
500	1/20	1/16
1000	2/55	1/32
2000	1/45	1/64
3000	1/70	1/128

Table 5.1: Mesh size and time step employed for each Reynolds number normalized by the length (R) and time (R^2/Γ) scales, respectively.

5.2 Results overview

In this section, we provide an overview of the results for Re = 2000 to highlight the effects of collision angle on the reconnection process (Reynolds number effects are considered in the final subsection herein). Snapshots of vorticity isosurfaces in their symmetrical sub-domain for all collision angles are shown in Figure 5.6. Note, for ease of reference in the discussion, we use letter sub-plot labels to refer to each collision angle in Figure 5.6. The roman numeral sub-plot labels (i)-(v) in Figure 5.6 refer to time steps from $t = 0$ to 20 at an interval of $\Delta t = 5$. Snapshots at $t = 0$ shown in Figure 5.6(i) are the same as the blue regions in Figure 5.1, but with their x-axes orientated vertically.

At $t = 5$ in Figure 5.6(ii), the colliding vortices initiate core contact, but no obvious qualitative differences are observed other than the collision angles. At $t = 10$ in Figure 5.6(iii), the colliding vortex tubes are now parallel with each other. Note, the colliding portion of the vortex tubes is commonly refereed as the reconnection threads in the literature. Major differences can be observed at this stage, where the reconnection threads are shorter but the tails of the threads (blue flat region extending downward from the leading threads) are larger for high collision angle cases. As the interactions progresses, the differences between the reconnection threads become increasingly prominent as shown in Figure 5.6(iv) and (v). For the $\theta = 60^\circ$ case in Figure 5.6(b-v), the vortex threads remain strong and continue to stretch radially outward. On the other hand, at large angles, such as the $\theta = 120^\circ$ case in Figure 5.6(e-v), the reconnection threads have already receded away. The reconnection bridges, which are newly formed vortex tubes that connect the colliding vortices, are also noticeable at either end of the reconnection threads starting at $t = 15$ (see Figure 5.6(iv)). Overall, we observed the same reconnection process across all non-zero collision angles, where the keys features, such as the reconnection threads and bridges, are clearly present. This agrees with the literature that similar reconnection process occurs regardless of the initial condition [111, 57, 109, 46, 7, 45, 6].

We note that there is no reconnection for the limiting case of $\theta = 0^\circ$ due to the colliding

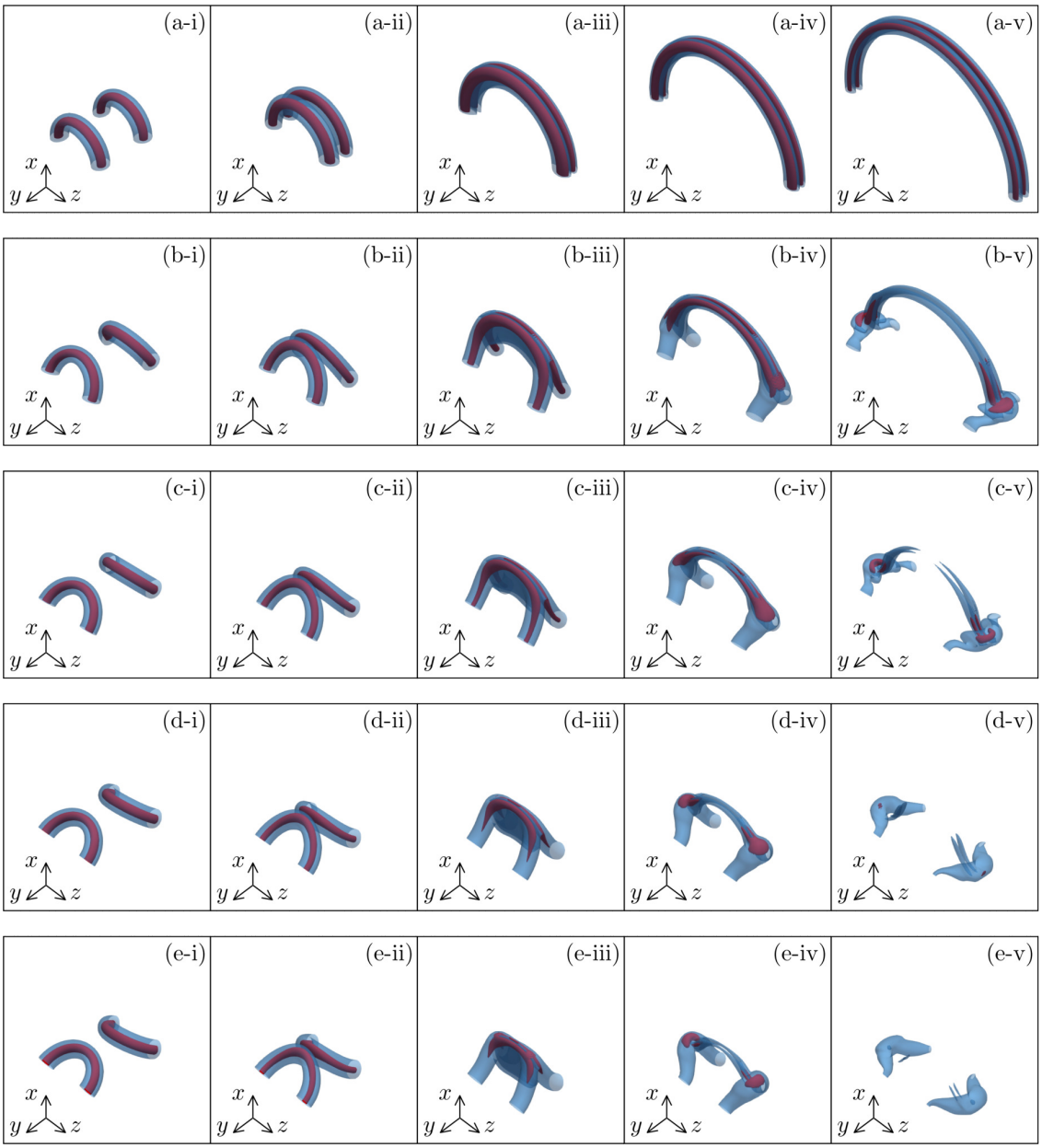

Figure 5.6: Vorticity isosurfaces of $|\boldsymbol{\omega}| = 1$ (transparent blue) and 2 (solid red) for collision angles (a) $\theta = 0°$, (b) 60°, (c) 90°, (d) 108°, and (e) 120° at $\mathrm{Re} = 2000$. Snapshots at $t = 0$ to 20 with an interval of $\Delta t = 5$ are shown in (i) to (v), respectively.

vortices remaining perfectly parallel to one another throughout their interaction. Entire vortex lines are annihilated completely because of the uniform cross-diffusion, hence no reconnection. However, the circulation reduction for the colliding vortex tubes is caused by the same mechanism as in the rest of the vortex reconnection cases, wherein the circulation is reduced by viscous cross-diffusion between the colliding vortices, and its rate is amplified by vortex stretching. The results from the case of $\theta = 0°$ provide an important baseline where the pyramid stretching is absent (parallel stretching only, see Figure 1.1), hence the inclusion in this study.

5.2.1 Enstrophy evolution

The vorticity evolution in Figure 5.6 demonstrates a strengthening of parallel stretching with respect to decreasing initial collision angle as a result of the improved uniformity in mutual induction between the colliding vortices, in agreement with our discussion around Figure 1.1. However, there are no obvious signs of the pyramid stretching.

To verify the qualitative observations in Figure 5.6, we quantify the level of vortex stretching using enstrophy evolution, which is defined as $\Omega(\boldsymbol{x}, t) = \boldsymbol{\omega}(\boldsymbol{x}, t) \cdot \boldsymbol{\omega}(\boldsymbol{x}, t)$. Its evolution is governed by the following enstrophy transport equation

$$\frac{\mathrm{D}\Omega}{\mathrm{D}t} = \omega_i \omega_j \left(\frac{\partial u_i}{\partial x_j} + \frac{\partial u_j}{\partial x_i} \right) + \nu \nabla^2 \Omega + 2\nu ||\nabla \boldsymbol{\omega}||^2 \tag{5.2}$$

where the subscripts i, j indicate the vector components in Einstein notation. The first term in the right-hand side of Equation (5.2) is the vortex stretching term that determines the level of enstrophy production, while the last two terms are the diffusion and dissipation terms from viscous effects [10]. Thus, enstrophy intensification during the reconnection process is an excellent indicator for level of vortex stretching.

Since pyramid stretching produces localized stretching at the pyramid apex (see Figure 1.1), we can quantify it from the peak enstrophy at the cutting plane $\Omega_p(t) = \max[\Omega(x, y, z = 0, t)]$. Note, we verified through inspection that the peak enstrophy remains within the vortex core throughout the entire simulation. On the other hand, parallel stretching produces overall stretching due to the uniformity in the mutual induction, and thus we employ total enstrophy $\Omega_p(t) = \int \Omega(\boldsymbol{x}, t) \, \mathrm{d}V$ for the entire symmetrical sub-domain to measure it. We note that the undesired vortex stretching from the rest of the vortex ring reported by Kida *et al.* [46] is eliminated by the symmetrical condition. Thus, it is safe to assume that the intensification of the total enstrophy $\Omega_p(t)$ is a good approximation for the overall stretching experienced during the reconnection process.

The evolution of the total and the peak cutting plane enstrophy are illustrated in Figure 5.7(a) and (b), respectively. As expected, a high level of total enstrophy amplification

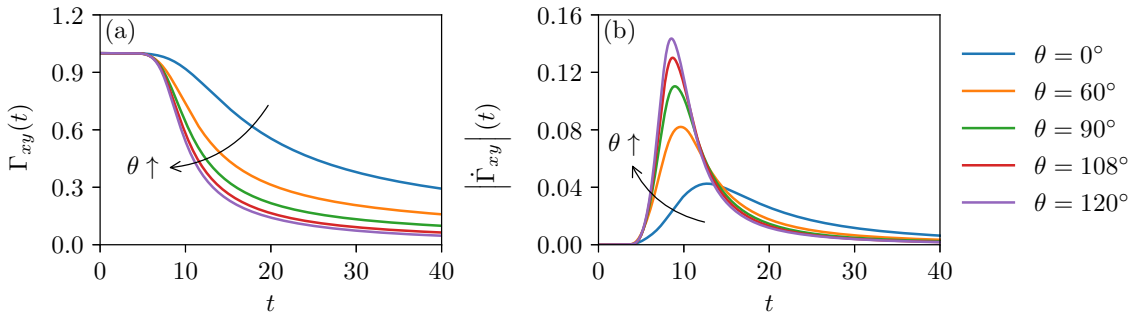

Figure 5.7: Temporal evolution of (b) total enstrophy (Ω_p) and (a) cutting plane peak enstrophy (Ω_p) for each collision angle (θ) at Re = 2000.

is observed for small angle cases in Figure 5.7(a), in agreement with the qualitative observations from Figure 5.6, where the reconnection threads are more stretched out at small angles. However, the large angles produce the most enstrophy amplification locally at the cutting plane, as shown in Figure 5.7(b). Combining with their minimal total enstrophy amplifications in Figure 5.7(a), the data reveal a highly localized stretching and vorticity amplification for large angles, aligned with pyramid stretching [62, 63]. This localized stretching results in double the local enstrophy intensity between the $\theta = 0°$ and $120°$ cases. The lack of evidences for such extreme amplification from the vorticity visualizations in Figure 5.6 is likely a result of the low value iso-surfaces masking the highly localized event, which may also explain the lack of reports of such localized stretching in the literature of viscous vortex reconnection.

Lastly, in agreement with the discussion in Figure 1.1, the collision angle controls the uniformity of mutual induction between the colliding vortices. For large angles, strong non-uniformity produces localized stretching through the pyramid process. On the other hand, at small angles, the uniformity weakens the pyramid stretching while strengthening the parallel stretching. The inverse trend between the local and total enstrophy with respect to collision angle illustrated in Figure 5.7 agrees with our hypothesis regarding the role of the collision angle in vortex reconnection, as it controls the vorticity amplification by adjusting the relative contributions of pyramid and parallel stretching.

5.2.2 Reconnection rate

The rate of reconnection is enhanced by vortex stretching, where the steeper gradient of a concentrated vortex core causes stronger cross-diffusion (higher $\nabla^2\boldsymbol{\omega}$) for the colliding vortices. As such, we would expect faster reconnection at larger angles because of the localized vorticity amplification.

To verify our speculation, we turn our attention to the cutting plane circulation evolution, $\Gamma_{xy}(t)$, and its rate, $|\dot{\Gamma}_{xy}|(t)$, as presented in Figure 5.8. We note that the loss of

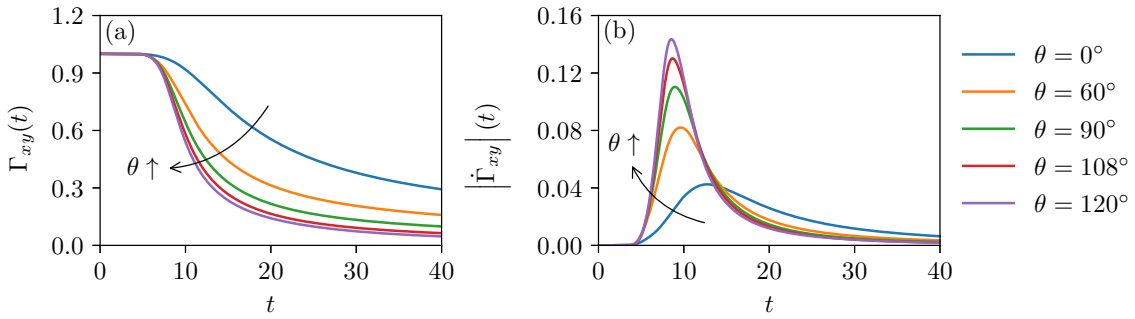

Figure 5.8: Temporal evolution of (a) the cutting plane circulation, and (b) its rate for each collision angle (θ) at $\mathrm{Re} = 2000$.

cutting plane circulation directly corresponds to a gain in the circulation for the reconnection bridges on the reconnection plane (Γ_{zy}) for non-zero angles. Thus, it is an effective measure of the reconnection rate and completeness. Figure 5.8 demonstrates that both the rate and completeness (indicated by the circulation value at large times) are greatly improved (faster and more complete) for large angles, in agreement with the conclusion of strong vorticity amplification at large angles from Figure 5.7(b). That is, pyramid stretching is able to produce effective vorticity amplification localized at the cutting plane to accelerate cross-diffusion for viscous vortex reconnection. Interestingly, the appearance of intense parallel stretching of the reconnection threads observed in Figure 5.6 is not an indication of performance of the viscous vortex reconnection, which can be easily misinterpreted when investigating vortex dynamics from flow visualization alone.

5.2.3 Reynolds number effects

In this sub-section, we report the impact of the Reynolds number. An overview of the vorticity iso-surfaces at $t = 15$ for all Reynolds number examined is illustrated in Figure 5.9.

In general,the reconnection threads are more stretched out at high Reynolds numbers, indicating a strengthening of parallel stretching for the reconnection threads.

Quantitatively, it has been argued that the Reynolds number scaling of viscous vortex reconnection is universal [39, 74, 6], with reconnection time $\propto \mathrm{Re}^{-3/4}$, where reconnection time is defined as the time for the cutting plane circulation (Γ_{zy}) to drop from 95% to 50% of its initial value. However, the reconnection time criteria is problematic for this study as it cannot account for the change in reconnection completeness, which also varies with the collision angle. Instead, we opt to employ the maximum rate of circulation loss on the cutting plane $\dot{\Gamma}_m = \max|\dot{\Gamma}_{xz}(t)|$ (see peak values in Figure 5.8(b)) to characterize the rate of reconnection, a parameter that is also reported in Hussain and Duraisamy [39].

Figure 5.10(a) compares the trends of $\dot{\Gamma}_m$ for Re = 500 and 3000. Both Reynolds numbers exhibit increasing trends regarding the collision angle, indicating that the localized vorticity amplification from the pyramid stretching is stronger at larger angles regardless of the Reynolds number. Interestingly, the reconnection rate is faster at Re = 3000 at large angles, but the trend reverses for small angles, which implies a change in the Reynolds number scaling with respect to the collision angle.

To confirm our observation, we explore the trend of the Reynolds number scaling in Figure 5.10(b), which reveals a wide range of scalings with opposing trends between high and low collision angles in the Reynolds number range examined. High Reynolds number vortices lead to faster mutual induction, resulting in stronger vortex stretching. For the pure parallel stretching of the $\theta = 0^\circ$ case, the peak reconnection rate scaling trends downward with increasing Reynolds number, indicating that the gain in vorticity amplification from vortex stretching is not sufficient to compensate for the loss of vorticity through viscous cross-diffusion. If the observed strengthening of the reconnection thread parallel stretching in Figure 5.9 is the primary mechanism for the viscous reconnection process, then we would expect a similar Reynolds number scaling to the $\theta = 0^\circ$ case for the rest of the collision angle scenarios. However, as the initial collision angle increases and offsets the balance of the stretching types, we see a gradual reversal of the Reynolds number scaling. That is, a sufficient strength of the pyramid stretching can produce a level of vorticity amplification that further increases the rate of cross-diffusion for reconnection at high Reynolds numbers.

Again, the observed strengthening of parallel stretching in Figure 5.9 is deceptive for judging the level of vorticity amplification through stretching for viscous vortex reconnection, as it can not explain the shift of Reynolds number scaling in Figure 5.10. The change in Reynolds number scaling solidifies the impact of the pyramid stretching and challenges the presumption of a universal Reynolds number scaling for viscous vortex reconnection

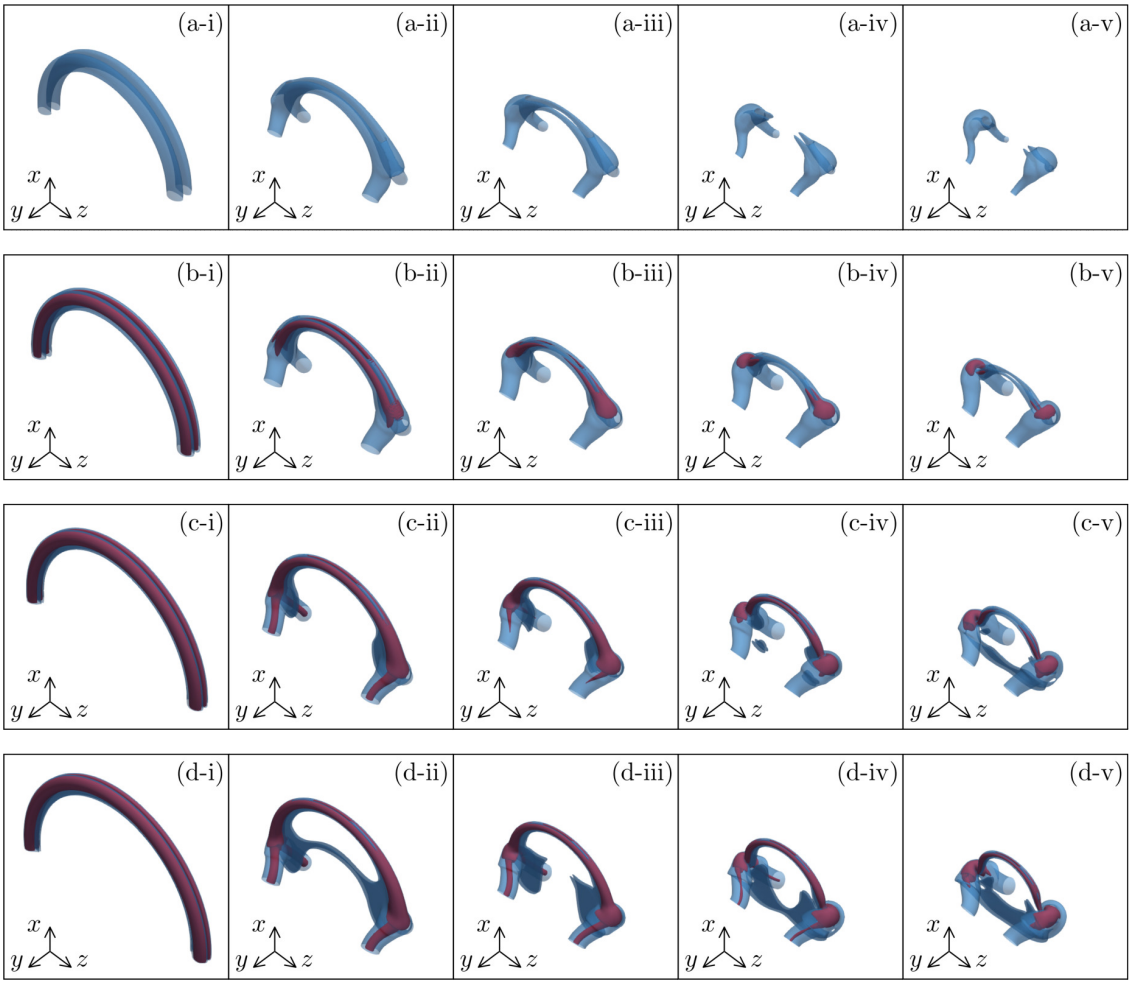

Figure 5.9: Vorticity isosurfaces of $|\boldsymbol{\omega}| = 1$ (transparent blue) and 2 (solid red) for Reynolds numbers (a) Re = 500, (b) 1000, (c) 2000, and (d) 3000 at $t = 15$. Collision angles of $\theta = 0°$, 60°, 90°, 108°, and 120° are shown in (i) to (v), respectively.

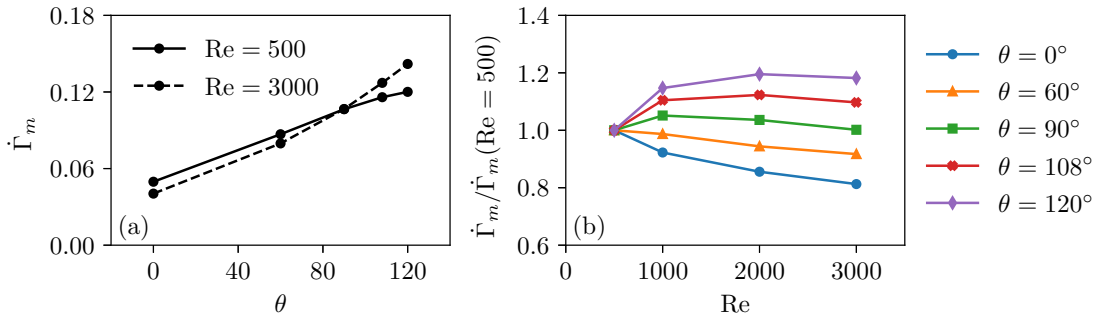

Figure 5.10: Comparison of the maximum rate of cutting plane circulation loss $\dot{\Gamma}_m$ with respect to (a) collision angle, and (b) Reynolds number normalized by values at Re = 500.

[39, 74, 6].

Last, we observe a ceiling for the max rate of circulation loss with respect to the Reynolds number in Figure 5.10(b). This is caused by the ephemeral nature of pyramid stretching, which will be further elaborated as a part of the discussion for the reconnection thread evolution in the Section 5.3.4.

5.3 Evolution of reconnection threads

In the last section, we reported a correlation between the localized vorticity amplification and the initial collision angle (see Figure 5.7(b)), which is in agreement with the expected behaviour of pyramid stretching. The localized vorticity intensification greatly increases the reconnection rate (see Figure 5.8) and Reynolds number scaling (see Figure 5.10), implying that pyramid stretching is the primary vortex stretching mechanism that determines the performance of viscous vortex reconnection. To further understanding the observed correlation, we examine the kinematics of the colliding vortices in detail.

To confirm the presence of pyramid stretching, we consider curvature evolution of the reconnection threads. Though there is no unique descriptor of the central axis for such deformed vortex tubes during the interaction, herein, we consider the vortex line connecting the peak vorticity within the vortex core at the cutting plane (xy plane) as the vortex center, which we refer to as the 'peak vorticity line'. The curvature evolution of the peak

vorticity line with respect to its arc length l is computed as

$$k(l,t) = \frac{|\gamma'(l) \times \gamma''(l)|^2}{|\gamma'(l)|^3} \tag{5.3}$$

where $\gamma(l)$ is the position along the vortex line and the prime symbol indicates a derivative with respect to l. We note that the peak vorticity line is obtained from the vorticity vector field using a fourth-order Runge-Kutta scheme with sub-pixel interpolation. As previously noted, we have confirmed though inspection that the peak vorticity on the cutting plane remains within the vortex core of the reconnection threads throughout the entire interaction.

The curvature evolution at the middle of the reconnection thread (where the vortex line intersects with the cutting plane), $k(0,t)$, is shown in Figure 5.11. Overall, a wide range of

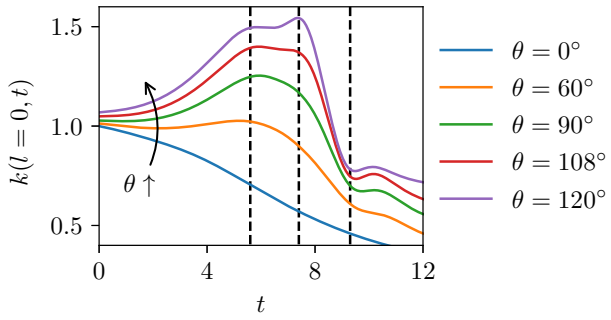

Figure 5.11: Curvature evolution at the middle ($l = 0$) of the reconnection thread. Reynolds number of Re $= 2000$ shown. Dash-lines mark time points associated with the end of pyramid stretching ($t \approx 5.6$), start of parallelization ($t \approx 7.4$), and the start of parallel stretching ($t \approx 9.3$).

behaviors ranging from a monotonic loss of curvature for $\theta = 0°$ (pure parallel stretching) to a rapid growth then decline of curvature for high angles is observed over the range of collision angles. The following sub-sections explore the curvature evolution in Figure 5.11 at the various stages (marked by dashed-lines) in detail.

5.3.1 Initial stretching ($t < 5.6$)

A key characteristic of pyramid stretching is the increase in curvature [62, 63], in contrast to the curvature loss from the parallel stretching (see Figure 1.1). For the case of $\theta = 0°$

with pure parallel stretching, the curvature monotonically decreases (see Figure 5.11) and the length-wise curvature distribution at $t = 5.6$ is flat (see Figure 5.12) as expected. This

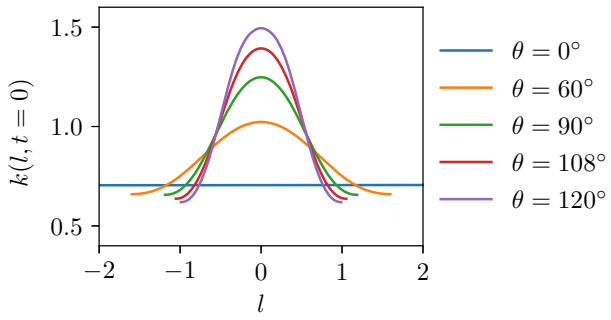

Figure 5.12: Curvature distribution at $t = 5.6$ and $\mathrm{Re} = 2000$ for all collision angles θ.

flat curvature distribution is an indication of the absence of a pyramid structure and non-uniformity in mutual induction. A vortex line in pyramid form would have a hyperbolic shape with a curvature peak in the middle [62, 63].

For $\theta = 60°$, pyramid stretching is introduced by the non-uniform mutual induction between the colliding vortices. At this angle pyramid stretching is still weak, and the curvature remains roughly constant prior to $t < 5.6$ as a result of the parallel stretching balancing out the pyramid stretching in the middle of the threads. However, the vortex line still develops into a pyramid form as illustrated by the curvature distribution in Figure 5.12, where the curvature is the highest in the middle ($l = 0$) and tapers off to either side. This indicates that pyramid stretching contributed to the increased local vorticity amplification we see from Equation (5.2)(b) in comparison to the $\theta = 0°$ case.

For $\theta = 90°$ and above, increased non-uniformity in mutual induction further promotes pyramid stretching while impeding parallel stretching. As such, the curvature growth (see Figure 5.11) and the pyramid form of the vortex lines (see Figure 5.12) are increasingly prominent, solidifying the link between the initial collision angle and the strength of pyramid stretching. The larger separation at the base of the pyramid at high angles creates a strong mutual induction differential along the thread, which promotes greater pyramid stretching, increasing the curvature and, thus, the level of vorticity intensification (see Equation (5.2)(b)). The extreme vorticity amplification creates a steep vorticity gradient that accelerates viscous cross-diffusion, and ultimately determines the rate and completeness of vortex reconnection. The vorticity isosurfaces presented in Figure 5.13 show that the pyramid apex becomes increasingly obvious from $\theta = 60°$ to $120°$ at $t = 5.5$, demonstrating the formation of the pyramid stretching and its link to collision angle.

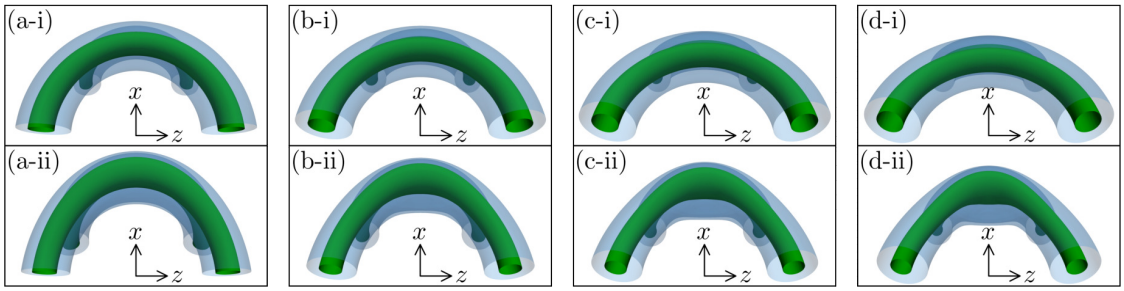

Figure 5.13: Vorticity isosurfaces of $|\boldsymbol{\omega}| = 1$ (transparent blue) and 2.5 (solid green) at (i) $t = 0$ and (ii) $t = 5.5$. Collision angles of $\theta = 60°$, $90°$, $108°$, and $120°$ are shown in (a) to (d), respectively.

5.3.2 Thread parallelization ($5.6 < t < 9.4$)

Between $5.6 < t < 7.4$ in Figure 5.11(a), the curvature evolution deviates noticeably from the increasing trend of pyramid stretching ($t < 5.6$). To determine the cause of such change in behavior, we first project the thread onto the reconnection (xz) and top (yz) planes and then consider the mid-point curvature in those planes, $k_{xz}(0,t)$ and $k_{yz}(0,t)$, respectively. The evolution of these projected curvatures are illustrated in Figure 5.14. We note that

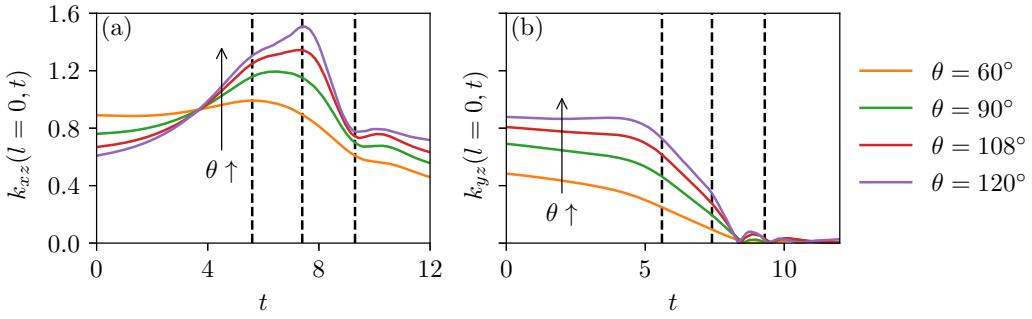

Figure 5.14: Curvature evolution of the key vortex line projected onto (a) the top (xz) and (b) the reconnection (yz) planes at $\mathrm{Re} = 2000$. Dash-lines marks $t = 5.6$, 7.4 and 9.3.

the differences in the initial values with θ are the result of the respective orientations due to the varying initial collision angles.

Figure 5.14(a) shows an increase in k_{xz} prior to $t = 5.6$ due to pyramid stretching,

which corresponds to the rapid curvature increase observed for $t < 5.6$ in Figure 5.11. From $5.6 < t < 7.4$, k_{xz} continues to increase for $\theta = 108°$ and $120°$ due to a strong pyramid stretching, albeit at a slower rate, whereas the growth of k_{xz} for $\theta = 60°$ and $90°$ halts and reverses. On the other hand, there is considerable loss of k_{yz}, shown in Figure 5.14(b), over the same period; that is, the colliding threads are becoming increasingly parallel to one another. A direct consequence of the increased parallelism is the improved uniformity in the mutual induction, which diminishes the effectiveness of the ongoing pyramid stretching and mitigates the growth of k_{xz} between $5.6 < t < 7.4$. For $t > 7.4$, $k_{yz}(0, t)$ reaches near zero, indicating that threads are no longer on the route to form a pyramid; instead, the colliding threads are now fully parallel. This is clearly shown in Figure 5.15, which presents the top view of the peak vortex lines. As a result, the curvature can not grow further due

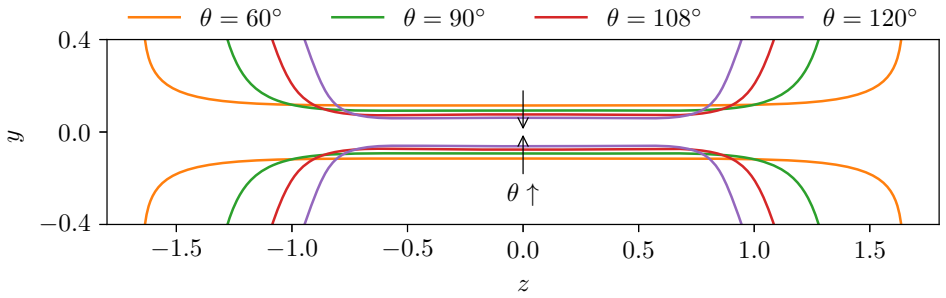

Figure 5.15: Top view of the peak vorticity line for each collision angle (θ) at $t = 9.3$ with $\mathrm{Re} = 2000$.

to the termination of the pyramid stretching, and the proceeding parallel stretching causes a rapid loss in k_{xz}.

Again, the peak vorticity line analysis can be corroborated by the vorticity isosurfaces shown in Figure 5.16. The snapshots prior to the rapid loss of k_{yz} ($t = 4.5$, see Figure 5.14(b)) are shown in Figure 5.16, where the colliding vortex tubes retain their curvature as expected. Subsequently at $t = 8$ when k_{yz} reaches zero, the vortex tubes are now full parallel with each other, indicating termination of the pyramid process.

Parallelization of the vortex tubes is triggered once the colliding vortex cores 'touch'. The colliding vortices can not penetrate the symmetrical plane, as demonstrated by the vortex core deformations shown in the cross-sectional vorticity distribution in Figure 5.17 at $t = 4.5$ during pyramid stretching. Note, the core distortions at this time are not a result of any vorticity cancellation, since they have yet to lose any of their circulation (see

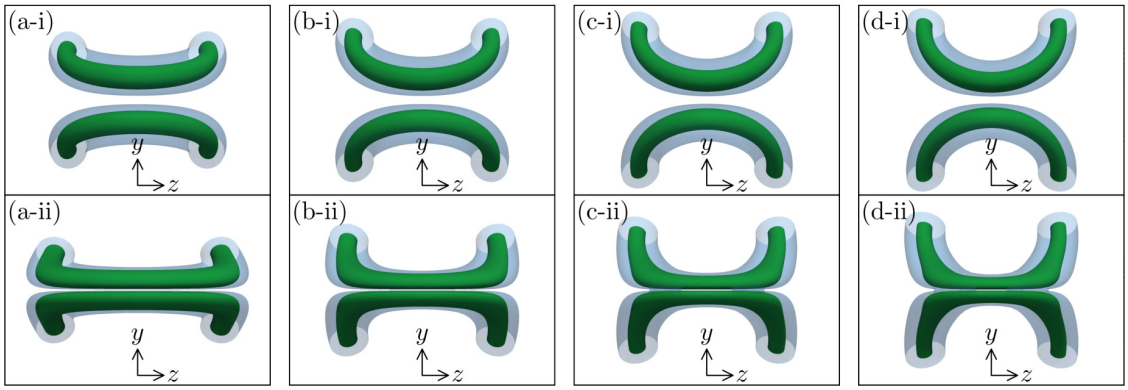

Figure 5.16: Vorticity isosurfaces of $|\boldsymbol{\omega}| = 1$ (transparent blue) and 2.5 (solid green) at (i) $t = 4.5$ and (ii) $t = 8$. Collision angles of $\theta = 60°$, $90°$, $108°$, and $120°$ are shown in (a) to (d), respectively.

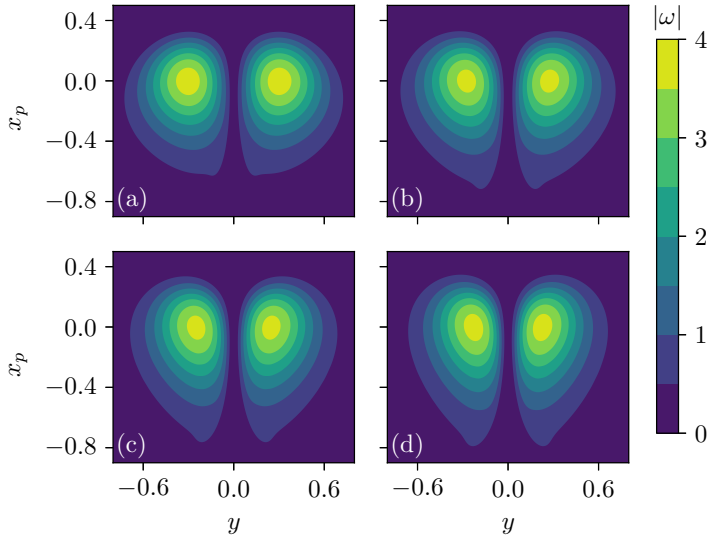

Figure 5.17: Vorticity distribution of the colliding vortex cores on the cutting plane (xy) at $t = 4.5$ and $\mathrm{Re} = 2000$. Collision angles of $\theta = 60°$, $90°$, $108°$, and $120°$ are shown in (a) to (d), respectively. The vortex cores are aligned at peak vorticity position x_p for ease of comparison.

Figure 5.8(a)). Thus, the colliding portion of the vortex tubes must have experienced a deceleration towards the symmetrical plane.

Based on these observations, we propose that the transition to parallel stretching is the primary mechanism that ends the pyramid process. As illustrated by the schematics in Figure 5.18, parallelization is initiated upon contact of the colliding vortex cores, which stalls their motion toward the reconnection plane. The regions of the vortex tubes away

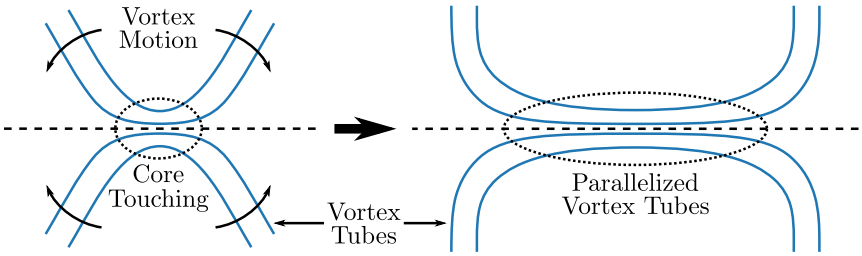

Figure 5.18: Schematic of the parallelization process.

from the core touching zone are still able to travel toward the reconnection plane under their own curvature-induced motion, which reverses the pyramid stretching progress and forces the colliding vortices to become parallel.

In other words, the assumption of the pyramid form of the vortices breaks down upon contact between the colliding vortex cores. Parallelization is not a process unique to viscous reconnection of thick core vortices. The pattern can also be found in previous viscous (Figure 2 from Ref. [39]), inviscid (Figure 6 from Ref. [13]), and thin core (Figure 2 from Ref. [107]) simulations. That is, the parallelization process appears to be an universal feature for vortex collision governed by both the Euler and Navier-Stokes equations.

5.3.3 Stages of stretching

Our results suggest that the stretching process consists of two distinct stages. The first stage mainly occurs during the approach, wherein vorticity amplification is dominated by pyramid stretching. While it only occurs for a very brief period, this stage determines the rate of reconnection by establishing the strength of the local vorticity field. The effectiveness of the pyramid stretching can be altered through the initial collision angle to greatly improves the rate of cross-diffusion across the reconnection plane. Subsequently, the collision of the vortex cores trigger the parallelization process. After the parallelization process, pure parallel stretching takes place, which continues indefinitely since reconnection

never completes [39]. Even though most of the reconnection occurs in the stage, it does not play a major role in determining the rate of reconnection due to its weak vorticity amplification.

Though the evolution of the reconnection threads in the parallel stretching stage are well documented in the literature, the later stages of reconnection thread separation warrant comment. The threads begin to separate from each other after $t \approx 10$, as shown in Figure 5.19. Here $s(t)$ is defined as the shortest distance between the peaks of vorticity

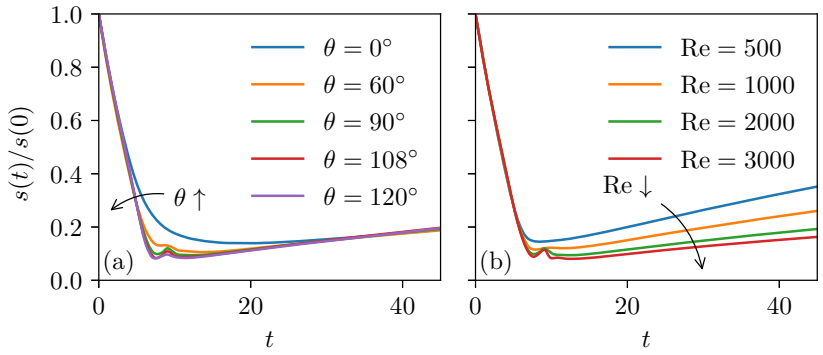

Figure 5.19: Time series of the normalized separation distance $s(t)/s(0)$ for (a) all collision angles at Re = 2000 and (b) all Reynolds numbers at $\theta = 90°$.

within the vortex core (see Figure 5.2). This is also reported by Yao and Hussain [107], wherein they attribute the separation to the outward mutual induced velocity overcoming the inward self-induced velocity. However, by normalizing the separation history with the initial value, we can collapse the data from the various collision angles, as seen in Figure 5.19(a), demonstrating that the separation occurs over the same time scale. Note, the initial position in our simulation is fine tuned, such that the reconnection of different angles occur at the same time. The similarity in time scale reveals that the separation mechanism is the same regardless of collision angle, including for the special case of $\theta = 0°$ [18, 23]. That is, the separation is actually a result of the vortex core enlargement from diffusion, which pushes them apart. This can be further validated by Figure 3 from Ref. [107] and our vorticity contours of the cutting plane vortex cores at $t = 30$ in Figure 5.20, where the cores are actually not separating from each other as they remain in contact. Our data with respect to Reynolds number also shows a slower time scale for higher Reynolds number, see Figure 5.19(b), in agreement with our conclusion that lower viscosity (for fixed circulation) reduces the rate of core diffusion and enlargement [18, 23].

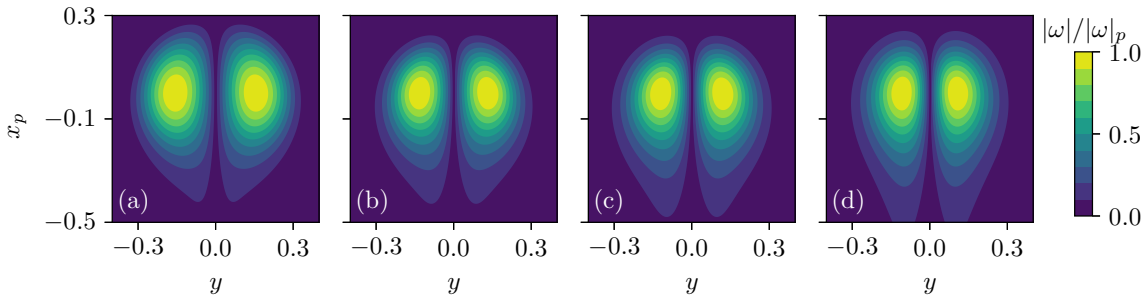

Figure 5.20: Vorticity distribution, normalized by the peak magnitude value $|\boldsymbol{\omega}|$, of the colliding vortex cores on the cutting plane (xy) at $t = 30$ and $\mathrm{Re} = 2000$. Collision angles of $\theta = 0$, 60°, 90°, and 108° are shown in (a) to (d), respectively. The vortex cores are aligned at the peak vorticity position x_p for ease of comparison.

5.3.4 Reynolds number effect

The Reynolds number scaling of viscous vortex reconnection can be altered though the collision angle as discussed in Section 5.2.3. To further investigate the the Reynolds number effect, we consider the the mid-point curvature evolution of the threads in Figure 5.21, analogous to Figure 5.11(a), at different Reynolds numbers for $\theta = 60°$ and $\theta = 120°$. The thread curvature evolution of these two cases exhibit the same trend regardless of

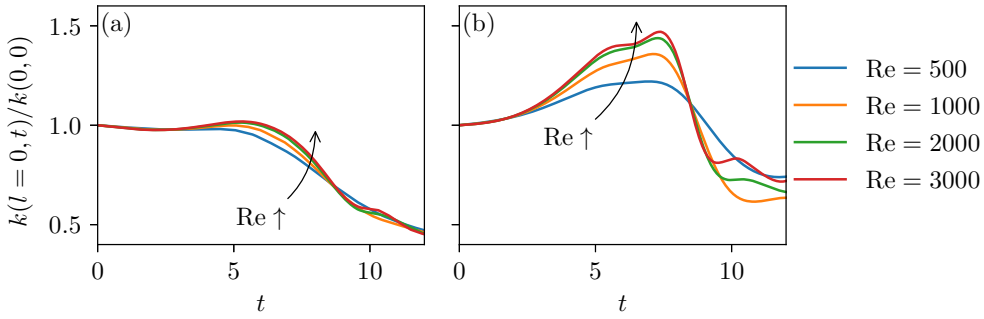

Figure 5.21: Comparison of mid-thread curvature evolution $k(l = 0, t)$ at various Reynolds number for $\theta =$ (a) 60° and (b) 120°.

Reynolds number, with an initial increase due to pyramid stretching followed by a decreases after parallelization. At low Reynolds number, the energy loss to viscous diffusion

results in both weaker self- and mutually-induced velocities, leading to weakened pyramid stretching. Additionally, the enlarged vortex cores due to strong diffusion at low Reynolds number also cause the parallelization process to occur earlier since the cores can touch each other sooner. Therefore, we see a stronger curvature gain from pyramid stretching as the Reynolds number increases in Figure 5.21.

The opposing trends in Reynolds number scaling in Figure 5.10(b) between the $\theta = 60°$ and $\theta = 120°$ can be attributed to the difference in the strength of the pyramid stretching with respect to the collision angle. Pyramid stretching is stronger at large angles and, therefore, when the Reynolds number increases, the improvement in vorticity amplification from pyramid stretching is able to overcome the loss of viscosity for cross-diffusion, resulting in a net gain in the reconnection rate with respect to Reynolds number. On the other hand, pyramid stretching is weak at smaller angles and, as a result, the improvement in vorticity amplification at higher Reynolds number is insufficient for cross-diffusion, resulting in a net loss in the reconnection rate with respect to the Reynolds number. That is, there is no universal scaling for viscous vortex reconnection, because the collision angle is a major control parameter.

5.4 Comments on other proposed mechanisms of arresting the pyramid process

Termination of pyramid stretching is the subject of a recent debate with regards to the possibility of finite-time singularity for the Euler and Navier-Stokes equations through the pyramid process [62, 63, 107]. Moffatt and Kimura analytically modeled the pyramid process with the Biot-Savart law for a pair of vortex rings, and provided an exemplar solution for a Gaussian vortex core with a initial size of $R_c = 10^{-5}$ in an inviscid flow (see Figure 23 from Ref. [62]). While the initial core size of this example is magnitudes lower than our simulation, they have shown that the core size to separation distance ratio reaches a limiting value of $s/R_c = 0.943367$ at the time of the Biot-Savart singularity. A value of s/R_c near unity is similar to our results shown in Figure 5.17, which permits us to speculate the behaviour at the extreme limit based on the evidence from this study.

The vorticity distribution of the Gaussian vortex core is defined as

$$\omega_\theta(r) = \omega_p \exp\left(-r^2/{R_c}^2\right) \tag{5.4}$$

where ω_p is the peak vorticity value at the center of the vortex core, and the total circulation

is

$$\Gamma = 2\pi \int_0^\infty \omega_\theta(r)\ r\mathrm{d}r = \pi\omega_p {R_c}^2. \tag{5.5}$$

Using the same integral in Equation (5.5) but instead with upper limits of R_c and $2R_c$, we find the circulations of the areas covered by one, and two core radii to be 62.21%, and 98.17% of the total circulation, respectively. That is, for the limiting value of $s/R_c = 0.943367$ in the example provided by Moffatt and Kimura [62], there is already significant overlap between the colliding vortex regions (see Figure 5.22), suggesting that core touching has already commenced prior to the occurrence of the finite time singularity. Therefore, we

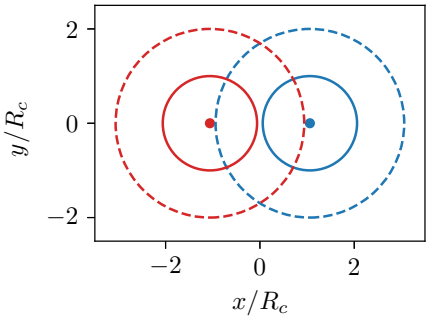

Figure 5.22: Illustration of the overlapping regions of Gaussian vortex cores with a core radius to separation distance ratio of $s/R_c = 0.943367$. Solid and dashed lines circle the areas of $1R_c$, and $2R_c$, respectively.

conjecture that the finite-time singularity through the pyramid process for the Gaussian core example from Moffatt and Kimura [62] can not be achieved due to the breakdown of the pyramid assumption from parallelization, unless there is a set of initial conditions for a Gaussian vortex core where the resulting limiting value of s/R_c is sufficiently large such that the contact between the colliding cores can be prevented.

5.4.1 Core flattening

Core flattening has long suspected to be a key contributor to the prevention of a finite-time singularity [35, 8, 63, 107]. We also observed noticeable core deformation post contact as shown in Figure 5.23, which reduces the mutual induction between the colliding vortices (x-axis). The weakened mutual induction contributes to the termination of pyramid

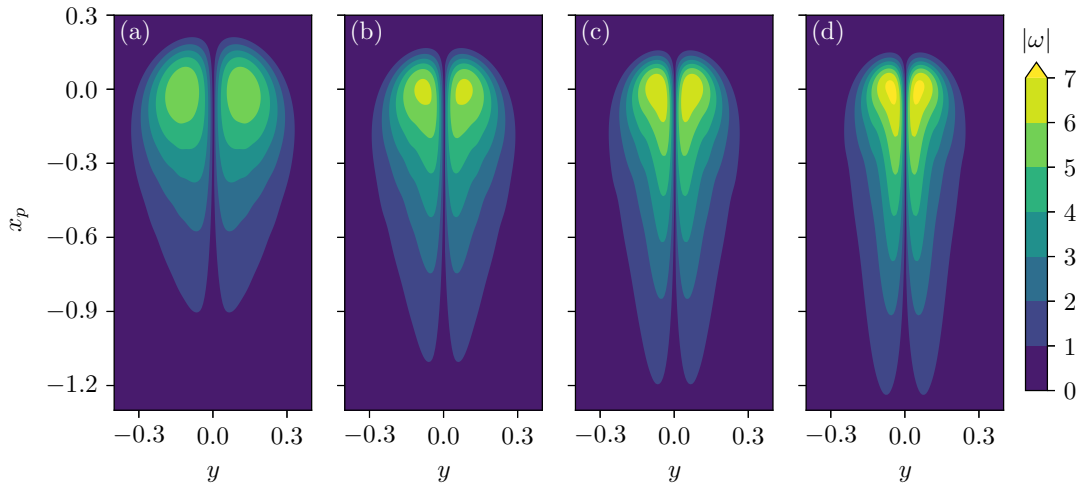

Figure 5.23: Vorticity distribution of the colliding vortex cores on the cutting plane (xy) at $t = 7.4$ and Re $= 2000$. Collision angles of $\theta = 60°$, $90°$, $108°$, and $120°$ are shown in (a) to (d), respectively. The vortex cores are aligned at the peak vorticity position x_p for ease of comparison.

stretching. Figure 5.23 also demonstrates a dependency of core flattening on collision angle, which can be attributed to increased strain on the vortex core due to the increased pyramid stretching at high angles.

By comparing our data with the slender core ($R_c = 0.01$) results from Yao and Hussain [107] (Figure 3 in Ref. [107]), we see a significant reduction in the core deformation with a decrease in core size. Their post-collision vortex cores maintained the shape of a Lamb dipole with only minor stripping of vorticity, a major deviation from the flattened cores in Figure 5.23. The Lamb dipole is the limiting case (in term of separation) for a vortex pair without any external strain [23]. As such, it is tenable that core flattening will not be a major factor for slender core vortices, in agreement with the analysis of Moffatt and Kimura [62].

5.4.2 Reconnection bridges

Yao and Hussain [107] proposed the bridge to be another contributor to the termination of the pyramid process. However, the bridge formed out of reconnection is in its early stage, as evident from Figure 6(a) in Yao and Hussain [107], where the colliding vortex cores

retain more than 90% of their circulation at the inflection point of the temporal curvature evolution ($\tau \approx 0.3$ from Figure 5(b) in Ref. [107]), which indicates the end of the pyramid process.

In the present study the threads lost less than 2% of their circulation to the bridge at the start of the parallelization process (see Figure 5.8(a) at $t = 5.6$). Furthermore, the bridges are still in the form of thin sheets at the end of the rapid curvature reversal ($t = 9.3$) as shown in Figure 5.24, implying that the bridges are likely incapable of inducing sufficient flow at the apex of the threads to substantially decrease the curvature. The thin

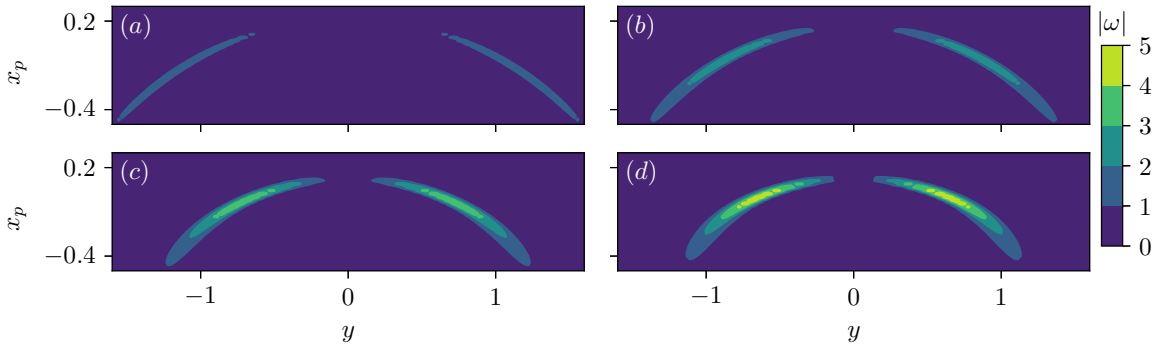

Figure 5.24: Vorticity distribution on the reconnection plane for $\theta =$ (a) 60°, (b) 90°, (c) 108°, and (d) 120° at $t = 9.3$ and Re = 2000. The bridges are aligned at the peak vorticity position x_p on the cutting plane for ease of comparison.

core simulations also support this observation, where the curvature growth halts at $\tau \approx 0.3$ (see Figure 5(b) in Ref. [107]), but the bridges remain as sheets at $\tau = 0.35$ (see Ref. [107] Figure 4). Note, Yao and Hussain [107] use τ as their temporal variable, equivalent to t in the present manuscript.

Even if the bridges have sufficient strength to influence the motion of the thread, for example, at $t = 15$ as shown in Figure 5.25 (note this is after the termination of the pyramid process), where the bridges are the bulges at ends of the reconnection threads, it is unlikely that they will significantly decrease the curvature of the threads due the inverse relationship of induced velocity with respect to the distance from the vortex core as shown in Figure 5.26. Therefore, we conclude that the bridges do not play a significant role in the termination of the pyramid process.

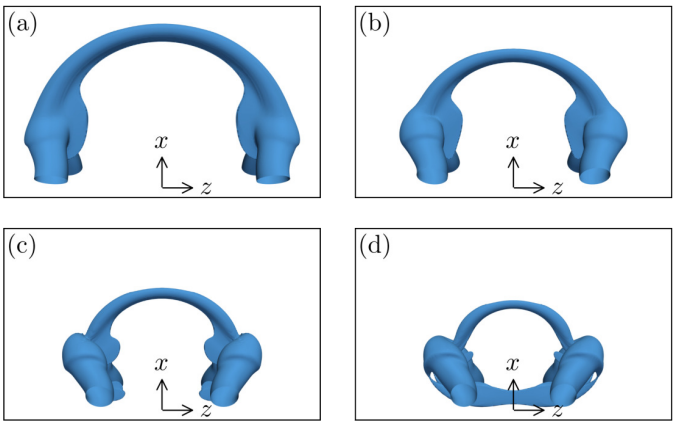

Figure 5.25: Vorticity isosurfaces of $|\boldsymbol{\omega}| = 1$ at $t = 15$ and $\mathrm{Re} = 2000$. Collision angles of $\theta = 60°$, $90°$, $108°$, and $120°$ are shown in (a) to (d), respectively.

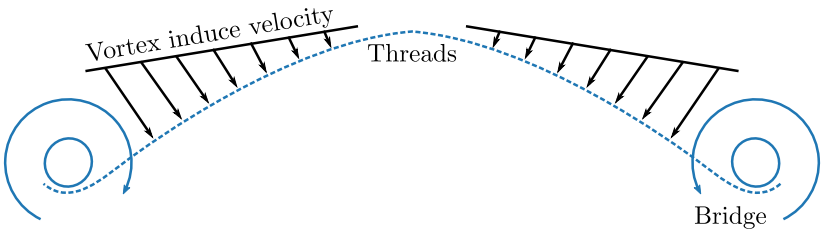

Figure 5.26: Schematic of the bridges' influence on the threads.

5.5 Conclusion

We revisit nuances of viscous vortex reconnection by colliding vortex rings at different initial collision angles. The change in collision angle allowed us to alter the balance of various mechanisms involved in the reconnection process independent of Reynolds number, and access the inner workings of viscous vortex reconnection. The main findings from our numerical experiments are summarized below.

Collision angle influences the viscous vortex reconnection process. While the reconnection process remains similar, an increase in the collision angle increases the rate and completeness of the reconnection. Moreover, changing the initial angle modifies the Reynolds number scaling of the reconnection, which challenges the presumption of an universal scaling for viscous vortex reconnection [39].

The collision angle exerts its influence through the manipulation of the pyramid stretching process during the approach of the colliding vortices, which we have found to be the primary mechanism of vorticity amplification for the viscous reconnection. The pyramid process is capable of extreme vorticity intensification that establishes the strength and gradient of the local vorticity field for vortex reconnection via viscous diffusion upon collision. A large initial collision angle promotes pyramid stretching, hence improving reconnection performance.

The pyramid stretching process was originally theorized with vortex filaments under Biot-Savat induction for quantum vortex reconnection. We have shown that the pyramid process also exists for the viscous reconnection of thick core vortices for the first time, thus supporting it as a universal route to vortex reconnection. However, the pyramid stretching phase ends quickly because of the parallelization process. Touching of the vortex cores upon collision prevents further motion towards the collision plane, allowing the portions of the vortex tubes away from the initial contact point to 'catch up' and parallelize with each other, which ends the pyramid process and initiates the parallel stretching phase.

The parallel stretching phase never completes for the vortex ring connection, and most of the reconnection occurs within this phase. However, parallel stretching exhibits weak vorticity amplification, and thus it does not play a significant role in determining the rate and completeness of the reconnection. A small initial collision angle improves the parallel stretching at this stage, but it does not correlate with the improvement of the vortex reconnection, which is deceptive for the analysis of vortex interaction and reconnection because of its high visibility in flow visualization.

Identification of the role of the parallelization process in vortex reconnection provides an alternative resolution to a recent dispute regarding the finite-time singularity though the

pyramid process, where the analytical model [62] claims the possibility, but the subsequent numerical simulations [107] did not find any evidence of finite-time singularity under a similar scenario. We conjecture that the parallelization process breaks the assumption of the pyramid structure upon core touching, which prevents the development of a finite-time singularity for Gaussian cores though the pyramid process regardless of the vortex core deformation and viscosity.

We also revisited other claims of regularization for the pyramid process by Yao and Hussain [107], namely core flattening and bridge vortices. By contrasting our thick core simulation with past slender core simulations, we found the smaller core significantly reduces the core deformation, in agreement with the analysis of Moffatt and Kimura [62] that core flattening is negligible at the lower limits of the core size. With regards to the bridge vortices, they are formed out of the reconnected vorticity via viscous diffusion long after parallelization and at a much slower time scale. Therefore, we conjecture that bridges do not play a significant role in terminating the pyramid process, even for low Reynolds number thick core vortex reconnection.

Chapter 6

Evolution of an uniform vortex dipole in a strain field

Herein, we examine the motion of a strained vortex dipole in an inviscid flow using contour dynamics. The paper is organized as follows: Section 6.1 outlines the problem formulation and numerical setup; Section 6.2 briefly discusses the strain monopole evolution; Section 6.3 explores the evolution of strained vortex dipoles; Section 6.4 discuss the enhanced mutual attraction due to core deformation; and Section 6.5 summarizes the major findings of the work. Lastly, the validation of our numerical scheme for the contour dynamics is displayed in Appendix C.

6.1 Problem statement

We consider a vortex dipole in an unbounded ideal fluid. A Cartesian coordinate system $\boldsymbol{x} = (x, y, z)$ is defined such that the x-axis is aligned with the convective direction of the vortex dipole, and the z-axis is parallel to the vortex lines, as shown in Figure 6.1. The vortex dipole consists of two uniform vorticity patches bounded by contours C_j. The vortex patches have opposing circulation of $\Gamma_j = A_j(t)\Omega_j(t)$, where $A_j(t)$, and $\Omega_i(t)$ are the patch area and uniform vorticity value, respectively. The subscript j indicates the patch number (i.e. 1 and 2 for top and bottom patches, respectively).

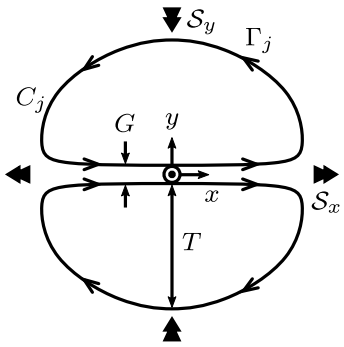

Figure 6.1: Schematic of a vortex dipole in a strain field with relevant variables indicated.

	$\mathcal{S}_x/\mathcal{W}_0$	$\mathcal{S}_y/\mathcal{W}_0$	$\mathcal{S}_z/\mathcal{W}_0$
Planar	$\mathcal{E}_r$	$-\mathcal{E}_r$	0
Bi-axial	0	$-\mathcal{E}_r$	$\mathcal{E}_r$
Pure	$-\mathcal{E}_r$	$-\mathcal{E}_r$	$2\mathcal{E}_r$

Table 6.1: Types of irrotational strain employed based on the axial stretching strength (along the z-axis).

6.1.1 Strain field

A three-dimensional irrotational uniform strain flow of $\boldsymbol{u}_s(\boldsymbol{x}) = (\mathcal{S}_x x,\ \mathcal{S}_y y,\ \mathcal{S}_z z)$ is imposed, where $\mathcal{S}_x$, $\mathcal{S}_y$ and $\mathcal{S}_z$ are the strain rates along each coordinate axis. The strain field is constrained by the continuity condition $\mathcal{S}_x + \mathcal{S}_y + \mathcal{S}_z = 0$. This strain flow has its principle axes aligned with the vortex dipole. Misalignment essentially introduces a rotational component to the stain field, which is not a concern of the present study, and is hence not considered herein. We further restrict $\mathcal{S}_y$ to be negative such that the y-component of the strain flow acts to push the two vortices together. $\mathcal{S} > 0$ would split the dipole into two monopoles that would then evolve separately with minimal coupled dynamics [98]. Hence, their behaviours could be readily predicted via vortex monopole models.

Herein four types of strain fields are considered, as listed in Table 6.1. The initial uniform vorticity magnitude of each patch is given by $\mathcal{W}_0 = \mathcal{W}(t = 0)$, and the initial strain-to-vorticity ratio is $\mathcal{E}_r$.

The first type is the planar strain field, which has equal but opposite strain rates in the x-y plane, and no axial stretching (along the z-axis). This is the only type of strain field investigated in previous strained vortex dipole studies [11, 46, 98]. The second type is the bi-axial strain field. This is achieved by decreasing the expansion rate in x-axis to

compensate for the increase in z-axis stretching. The third type is the pure axial strain field with equal magnitudes of compression both along x- and y-axes to compensate for the strong axial stretching in z-axis.

For each strain type, the strain-to-vorticity ratio is systematically varied between $0 \leq \mathcal{E}_r \leq 1$. The ratio is bounded from above by unity to examine vortex dominated flow.

6.1.2 Contour dynamics

The induced velocity at any point $\boldsymbol{u}_\omega(\boldsymbol{x})$ by the uniform vortex patches is computed from

$$\boldsymbol{u}_\omega(\boldsymbol{x}) = -\frac{1}{2\pi} \sum_{j=1}^{N} \mathcal{W}_j(t) \int_{C_i} \ln |\boldsymbol{x} - \boldsymbol{x}'| \, \mathrm{d}\boldsymbol{l}' \tag{6.1}$$

where N is the number of vortex patches, and $\mathrm{d}\boldsymbol{l}'$ is the infinitesimal boundary segment at $\boldsymbol{x}'$ [110].

Contour dynamics is a purely two-dimensional method, but the effect of axial stretching can be captured analytically as [70, 40]

$$\mathcal{W}(t) = \mathcal{W}_0 \exp(\mathcal{S}_z t). \tag{6.2}$$

That is, axial stretching essentially acts to dynamically decrease the strain-to-vorticity ratio $\mathcal{E}_r$ throughout the interaction when $\mathcal{S}_z > 0$.

6.1.3 Numerical scheme

The total velocity at any point is

$$\boldsymbol{u}(\boldsymbol{x}) = \boldsymbol{u}_\omega(\boldsymbol{x}) + \boldsymbol{u}_s(\boldsymbol{x}). \tag{6.3}$$

which is a combination of both the background strain flow $\boldsymbol{u}_s(\boldsymbol{x})$ and the vortex induced flow $\boldsymbol{u}_\omega(\boldsymbol{x})$. To compute the evolution of the vortex motion, we discretize the vortex contours into a collection of linear segments. The integral in Equation (6.1) is evaluated in closed form along each linear segment, then summed, along with the strain flow, to compute the total induced velocity at each of the end points of the line segments. The line segments are then advected in time using an adaptive eighth-order explicit Runge-Kutta method. For all simulations in this study, the contours are discretized into 1024 segments.

A symmetry condition between the two halves of the dipole is implemented to improve computational efficiency, as past studies of strained vortex dipoles have found them to maintain their top-bottom symmetry [11, 46, 98].

The numerical scheme is validated in two ways, by checking that circulation in conserved, and via comparison with classical examples in contour dynamics. Regarding circulation, since the vortex patches have uniformly distributed vorticity, conservation of circulation is equivalent to conservation of area, such that (6.2) becomes $A(t) = A(0)\exp(\mathcal{S}_z t)$. The deviation in vortex patch area for all results presented herein is less than 0.1%. In addition, several classical examples of contour dynamics were solved using the present numerical scheme, including a strained vortex monopole [43, 70], the Kirchhoff elliptic vortex [25, 60], and coalescence of two equal same-signed vortices [110, 40]. Samples of the solutions of these classical problems are presented in Appendix C, which agree very well with the vortex dynamics documented in the literature.

6.1.4 Initial conditions

Special considerations for the initial condition are required, because circular cores for the vortex dipole produce unrealistic deformations [46]. An inviscid strain-free vortex dipole (the limiting case of $\mathcal{E}_r = 0$, also known as a Lamb–Chaplygin dipole [58]) travels steadily with no self-induced deformation, and maintains its two-fold symmetry (front-back and top-bottom). To find such an initial condition for our simulations, we employ the method developed by Pierrehumbert [84]. In short, the method relies on the fact that a steady vortex dipole has a constant stream function value along its bounding contour. Hence, the shape of a steady uniform vorticity vortex dipole can found by adjusting its contour until the stream function value becomes constant at the vortex boundary using an iterative optimization algorithm.

The shape of the vortex core can be controlled through the gap ratio $G/(G + 2T)$, where G is the gap length, and T is the thickness of the vortex patch in the y-direction (see Figure 6.1). A gap ratio of 0.1 is employed herein, which produces the vortex dipole shown in Figure 6.2 Note, $R_{eq} = \sqrt{A(t = 0)/\pi}$ is the equivalent radius of the vortex core. A non-zero gap ratio is employed for two reasons. First, it is unreasonable to assume that only axial touching vortex pairs exist in turbulent flow, and we wish to examine the nonlinear collision dynamics driven by an external/curvature-induced strain field. Second, [63] have shown that colliding vortices (with their pyramid model) reach an asymptotic value $y_c/R_{eq} = 0.7788$, where y_c is the core centroid position, at the time of the Biot-Savart singularity. Our initial condition has a value of $y_c/R_{eq} = 0.8736$ (slightly bigger gap),

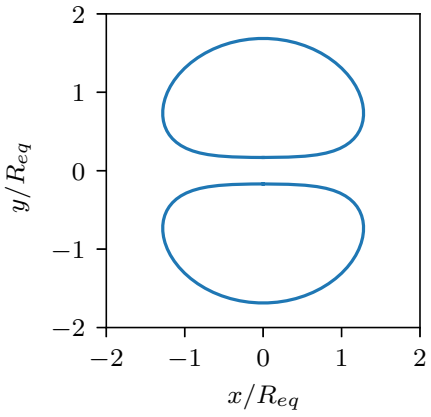

Figure 6.2: Initial condition of a vortex dipole with a gap ratio of $G/(G+2T) = 0.1$.

which permits us to evaluate the vortex core behaviour prior to the singularity under the influence of curvature-induced strain.

For the remainder of the article, we will employ the equivalent radius of the vortex core as length scale and the magnitude of the strain rate in y-axis $|\mathcal{S}_y|$ as the time scale unless otherwise stated.

6.2 Strained monopole review

In this section, we review the results for an initially circular vortex monopole in the same external strain flow in Table 6.1 to provide a baseline for the dipole study. Particularly, the principal axes length ratio (R_a/R_b, see Figure 6.3) is the primary quantitative results reported in the literature [43, 70], which does not apply to the dipole study. Instead, we employ the thickness parameter $T = 2\min(R_a, R_b)$ as the measurement of the compactness for the vortex core to facilitate comparisons with the dipole results.

The vortex monopole remains elliptical at all times in the strain flow, and its motion

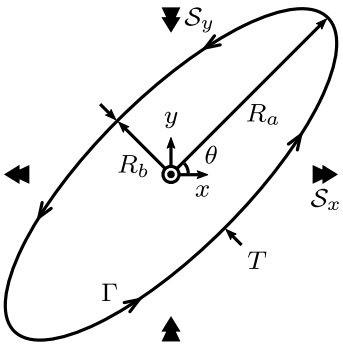

Figure 6.3: Schematic of a vortex monopole in an irrotational strain flow.

is governed by the following set of ordinary differential equations

$$\frac{\mathrm{d}R_a}{\mathrm{d}t} = R_a\left(\alpha\cos^2\theta + \beta\sin^2\theta\right) \tag{6.4a}$$

$$\frac{\mathrm{d}R_b}{\mathrm{d}t} = R_b\left(\beta\cos^2\theta + \alpha\sin^2\theta\right) \tag{6.4b}$$

$$\frac{\mathrm{d}\theta}{\mathrm{d}t} = \Omega(t)\frac{R_aR_b}{(R_a+R_b)^2} - \frac{\alpha-\beta}{2}\frac{R_a^2+R_b^2}{R_a^2-R_b^2}\sin 2\theta \tag{6.4c}$$

where θ is the orientation of the vortex monopole [70]. The results reported here are obtained with the Equation (6.4), though it was confirmed that the contour dynamics method described in Section 6.1 yielded identical results (see Appendix C for a comparison sample).

The equations of motion for the monopole can be decomposed into two major effects. First, the self-rotation of an elliptical vortex captured by the first term in Equation (6.4c), which states that a higher ellipticity of the vortex monopole corresponds with a lower self-rotation rate. Second, the irrotational strain field can be decomposed into a linear (symmetric) and a rotational (antisymmetric) component depending on the bearing (θ) of the principal axes. As the monopole reorients under its self-induced rotation, the linear component of the strain flow can either flatten or compact the vortex core, which in turn influences the rotation rate along with the rotational component of the strain field.

For the planar strain listed in Table 6.1, the vortex motion bifurcates into either averaging or flattening regimes, as shown in Figure 6.4. For the averaging regime in Figure 6.4(a), the strain flow elongates the monopole into an ellipse. Once the major axis passes $\theta = 45°$, where the max aspect ratio occurs, the strain flow compresses the boundary back to a circular shape. For the flattening regime in Figure 6.4(b), the major axis never rotates

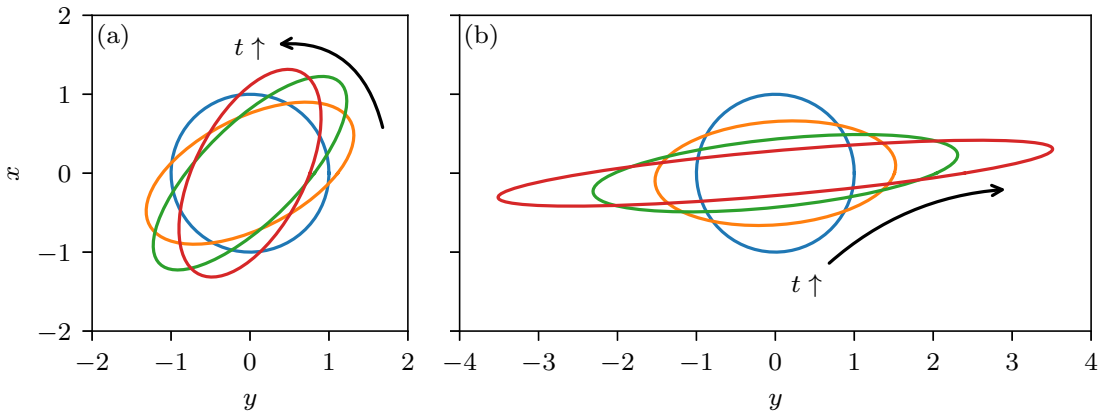

Figure 6.4: Snapshots of a vortex monopole in a planar strain flow with a strain-to-vorticity ratio of (a) $\mathcal{E}_r = 0.1$, and (b) $\mathcal{E}_r = 0.6$ at a time interval of $t = 0.426$.

past $\theta = 45°$ because the counter-clockwise self-rotation halts, and the strain flow flattens the monopole indefinitely into a sheet.

The quantitative results for the averaging regime for the planar strain flow are shown in Figure 6.5. Prior to the major axis reaching $\theta = 45°$, the rotation rate $\dot{\theta}$ decelerates under the influence of both the counter-rotating strain component and the increased monopole ellipticity, as shown in Figure 6.5(a). Therefore, a stronger strain field results in a slower rotation rate, which corresponds to a longer period of thickness oscillation in Figure 6.5(b). However, the deceleration is insufficient to prevent the monopole from moving past $\theta = 45°$, after which the strain flow compacts the vortex back to the circular shape; hence the oscillation of the vortex increases, but it never flattens.

For $\mathcal{E} \geq 0.123$, the strain flow prevents the major axis of the elliptical vortex monopole from passing $\theta = 45°$, and reverses the monopole self-rotation as shown in Figure 6.6(a). As such, the principal axes of the vortex are orientated with the flattening strain field indefinitely, hence compressing the monopole into a vortex sheet. A transient period can be seen from the normalized thickness evolution in Figure 6.6(b) because of the initial misalignment, but as time progress, the counter-rotating component of the strain flow re-aligns the principal axes between the strain flow and the vortex. Thus, the vortex flattens at the same rate as a simple material surface, as shown by the levelled normalized thickness at large times in Figure 6.6(b). Note, the normalized thickness is defined as $\widetilde{T} = T_1(t)/\exp(\mathcal{S}_y t)$, which highlights the role of vorticity on the thickness evolution in contrast to a vorticity free material contour under the same compression. The exponential

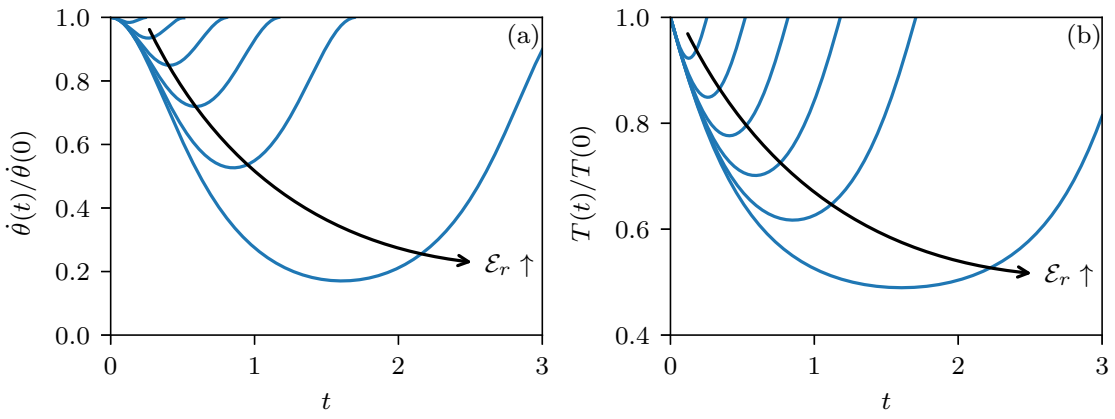

Figure 6.5: Evolution of the (a) rotation rate $\dot{\theta}(t)$, and (b) thickness $T(t)$ of a vortex monopole in a planar strain field with a strain-to-vorticity ratio of $\mathcal{E}_r = 0.02$ to 0.12 at an interval of 0.02. Only one period of oscillation shown for clarity.

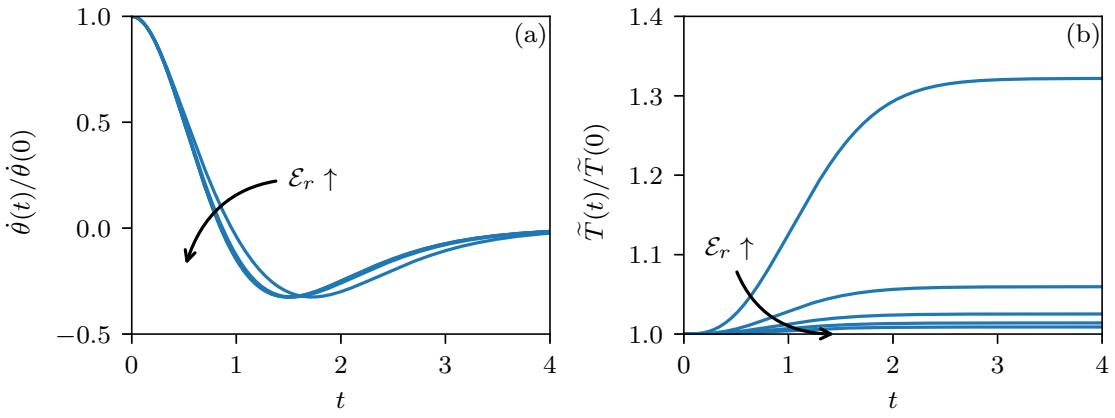

Figure 6.6: Evolution of the (a) rotation rate $\dot{\theta}(t)$, and (b) normalized thickness $\widetilde{T}(t)$ for a vortex monopole in a planar strain field with a strain-to-vorticity ratio of $\mathcal{E} = 0.2$ to 1.0 at an interval of 0.2.

term is the thickness of the a vorticity free material contour obtained by solving equation $\mathrm{d}T_1/\mathrm{d}t = \mathcal{S}_y T_1/2$.

The introduction of the bi-axial stretching (see Table 6.1) has two effects, since the axial stretching effectively lowers the strain-to-vorticity ratio $\mathcal{E}_r$ dynamically. First, the bifurcation limit pushed to a much higher limit (above strain-to-vorticity ratio of 3). Second, for the averaging regime, the initially circular vortex patch will be elongated permanently due the hysteresis introduced at the begin, where the effect of the strain flow is relatively strong. As time proceeds, the stretching effectively drops $\mathcal{E}_r$ to zero, and the vortex becomes an stable ellipse that rotates under its self-induction. That is, the indefinite flattening occurs for the bi-axial stretching cases. The pure stretching case is trivial, where the circular vortex reduces its area due to stretching but maintains the shape.

6.3 Strained dipole

6.3.1 Planar strain field

Three strain-to-vorticity ratios, $\mathcal{E}_r = 0.05$, 0.2, and 0.4, are considered to highlight vortex dipole behaviours under the applied planar strain field introduced in Table 6.1.

The evolution of the dipole contours for $\mathcal{E}_r = 0.05$ is shown in Figure 6.7, which illustrates a typical formation of the head-tail structure of a strained vortex dipole. In Figure 6.7(b), the dipole halves are being squeezed together under the converging strain flow, which deforms it into a heart-like shape. Subsequently, the classical head-tail structure is formed upon core touching in Figure 6.7(c). The back end of the heart-like shape is compressed into the tail, while the leading dipole has shape similar to a strain-free axially touching vortex dipole [84, 91]. As time progresses in Figure 6.7(d-f), the dipole continues to shrink as vorticity is ejected into the tail.

The dipole behaviour begins to change with a further increase in the vorticity to $\mathcal{E}_r = 0.2$, as shown in Figure 6.8. The vortex cores are far more stretched out horizontally, to a point where the leading edges have no visible bulges, as seen in Figure 6.8(d). However, the profile of the vortex patches are still thickest near the leading edges, which then taper off in a tail. At $t = 1.5$, the bulges near the leading edge are finally visible, indicating that there is still a structure that resembles a head-tail arrangement, but with much of the circulation allocated to the tail.

With a sufficiently large strain-to-vorticity ratio the dipole can be flattened into vortex sheets completely, as shown in Figure 6.9 for $\mathcal{E}_r = 0.4$. At the early stages of the

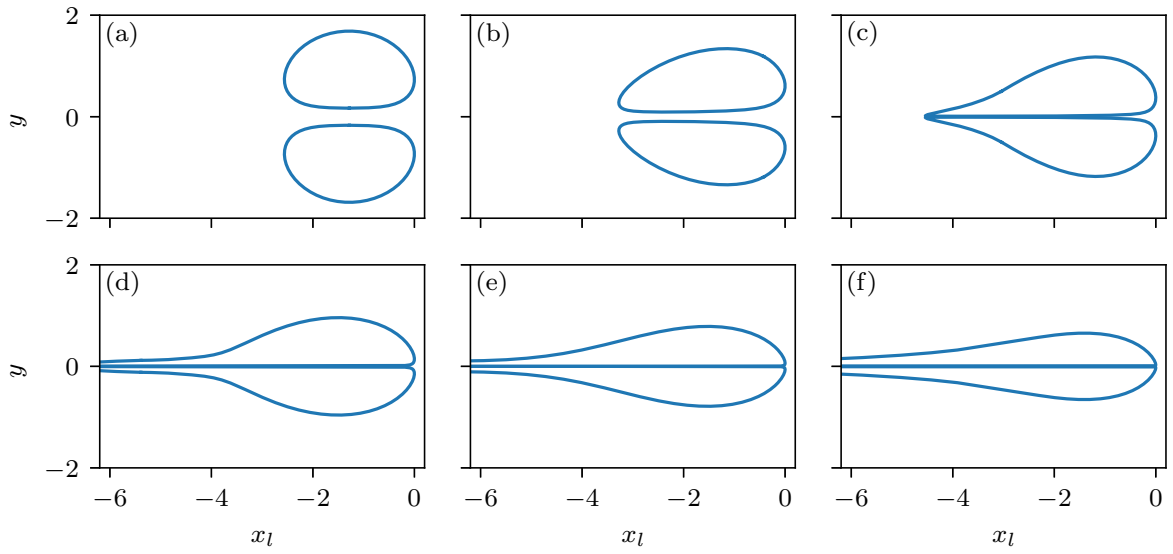

Figure 6.7: Contour evolution of a vortex dipole in a planar strain field with $\mathcal{E}_r = 0.05$. Snapshots from $t = 0$ to 1.5 at an interval of 0.3 are shown from (a) to (f), respectively. The contours at each time step are aligned at their leading edge x_l for ease of comparison.

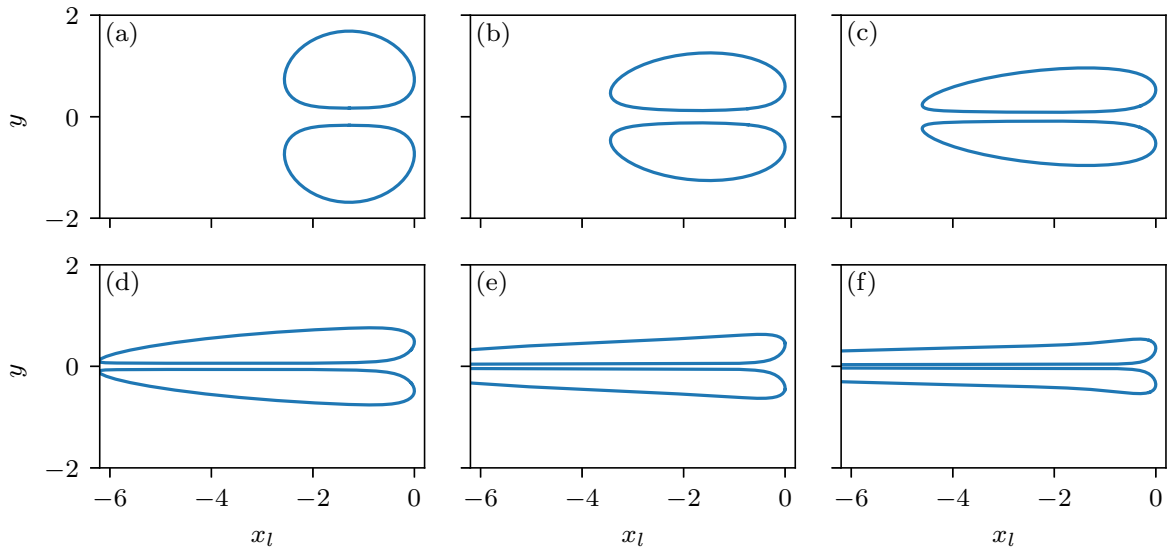

Figure 6.8: Contour evolution of a vortex dipole in a planar strain field with $\mathcal{E}_r = 0.2$. Snapshots from $t = 0$ to $t = 1.5$ at an interval of 0.3 are shown from (a) to (f), respectively. The contours at each time step are aligned at their leading edge x_l for ease of comparison.

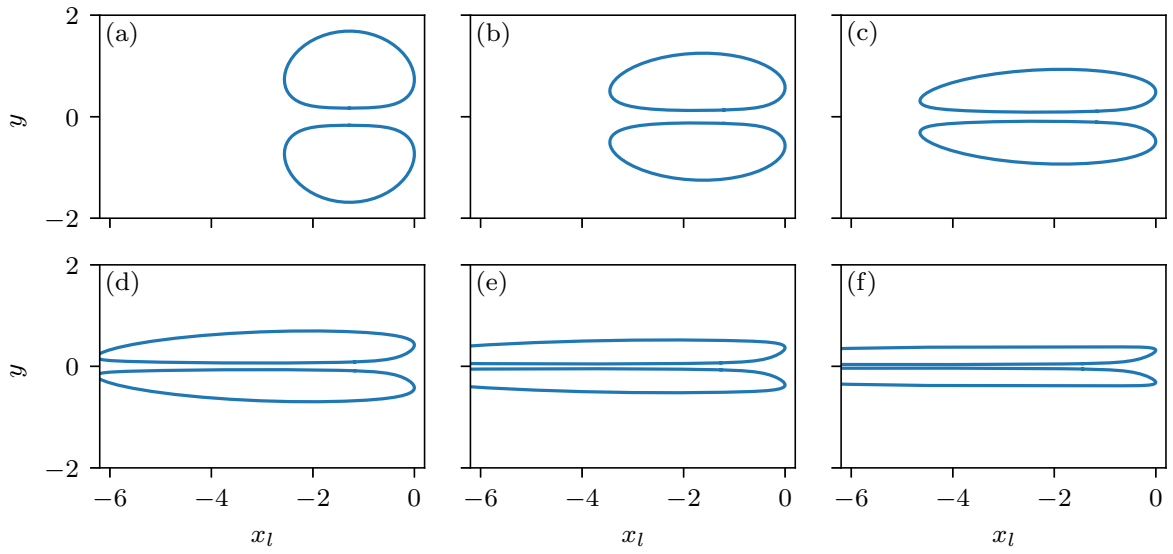

Figure 6.9: Contour evolution of a vortex dipole in a planar strain field with $\mathcal{E}_r = 0.4$. Snapshots from $t = 0$ to $t = 1.5$ at an interval of 0.3 are shown from (a) to (f), respectively. The contours at each time step are aligned at their leading edge x_l for ease of comparison.

interaction, the vortex patches are mostly symmetrical, as seen in Figure 6.9(b,c), which is an early indication of a change in the flow regime. Later, in Figure 6.9(d-f), the patches are completely flattened into sheets. At $t = 1.5$ in Figure 6.9(f), the vortex patches have near uniform thickness, with the leading edges forming a nozzle-like shape. The pairing of vortex sheets induces a planar jet that shoot out into the ambient environment instead of recirculating around the leading edge.

Recent surveys have shown that turbulent flows are composed of a self-similar hierarchy of anti-parallel pairs of vortex tubes [32, 68], for which the vortex dipole model can be considered a fundamental element. [8, 55] introduced a turbulent cascade model wherein vortices iteratively flattened into a vortex sheet then re-roll into smaller vortices. The present work has demonstrated that anti-parallel vortex pairs offer little resistance to the flattening efforts of a background strain flow, supporting the feasibility of the proposed vortex sheet turbulent cascade model.

6.3.2 Thickness

The compactness of monopoles can be easily quantified with the ratio between the principle axes of their elliptical form [43, 70], but there is no predetermined form for dipole deformation; hence, a new descriptor is required to measure the compactness of the deformed vortex dipole patches. Observing from, for example, Figure 6.8, that the deformations are always aligned with the axes of the strain field, we employ the maximum thickness $T(t)$ of the vortex patch (see Figure 6.1 to measure the compactness of the dipole patches, as a decrease in the thickness corresponds with the flattening of the vortex patches.

The temporal evolution of the maximum thickness $T(t)$ for all the planar strain field cases is illustrated in Figure 6.10(a), normalized by the initial thickness $T(0)$. Overall, there is a decreasing trend regardless of the strength of the strain field. That is, unlike the vortex monopole, the cores of the vortex dipole are not capable of retaining their compactness, even for the head-tail regime. As discussed in Section 6.2, a vortex monopole combats the strain field by a self-induced rotation that causes the principal axes alternately flatten and contract in a periodic manner. But for the vortex dipole, the pairing essentially create a slip wall that prevents each vortex patches' principal axes from rotating. As such, the axes of deformation are always aligned with the strain field, and thus the patches continually and increasingly flatten. Over at large times, we found the head-tail structure still exists since the critical parameter $\mathcal{E}_r$ remains the same for the leading dipole. That is, there is a fundamental differences in the behaviour between the two regimes. However, for the flattening regime, the leading edge eventually begins to lift up, likely an attempt to roll

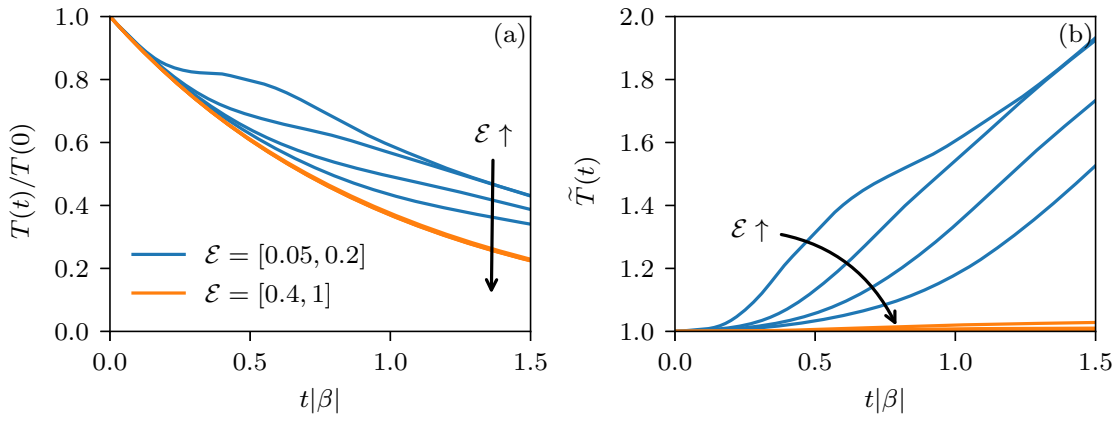

Figure 6.10: Temporal evolution of the vortex patch (a) thickness $T(t)$ and (b) normalized thickness $\widetilde{T}(t)$ for the planar strain field cases.

up, since vortex sheets are unstable. Then the problem becomes a strained vortex sheet problem, which is not a concern for this chapter.

To further isolate the effect of vorticity, we employ the normalized thickness $\widetilde{T}(t)$ (for more detail, see Figure 6.6 for the monopole case.). A value greater than one for the normalized thickness means the vorticity decelerates the strain field-induced flattening. The normalized thickness presented in Figure 6.10(b) clearly shows two trends. First, for cases $\mathcal{E} = 0.05,\ 0.1,\ 0.15,\ 0.2$, there is continuous growth of the normalized thickness. That is, the dipole thickness becomes increasingly bulkier than a simple material surface, indicating that vorticity is capable of some resistance to the strain flow. Interestingly, these cases corresponds with the head-tail regime from the contour evolution discussion in the previous sub-section. That is, the flattening resistance originates from the flow expansion at the front of the leading dipole, a unique mechanism that is absent from the monopole. We note that for the case of $\mathcal{E} = 0.05$, the rate of vortex patch flattening is faster than all other cases between $0.6 < t < 1$. This is likely due to the small tail for the dipole initially, which provides more room in the wake initially for the vorticity ejection.

For cases $\mathcal{E} = 0.4,\ 0.6,\ 0.8,\ 1.0$, the patches are flattened without any noticeable resistance to flattening. That is, the its thickness does not differ significantly to the a material surface without vorticity, as the normalized thickness flattens out with only a slight transition in the beginning, much like the monopoles cases shown in Figure 6.6. These cases correspond with the planar jet regime, where the head-tail formation is arrested by the strain flow, preventing any vorticity from collecting at the leading edges. Vorticity

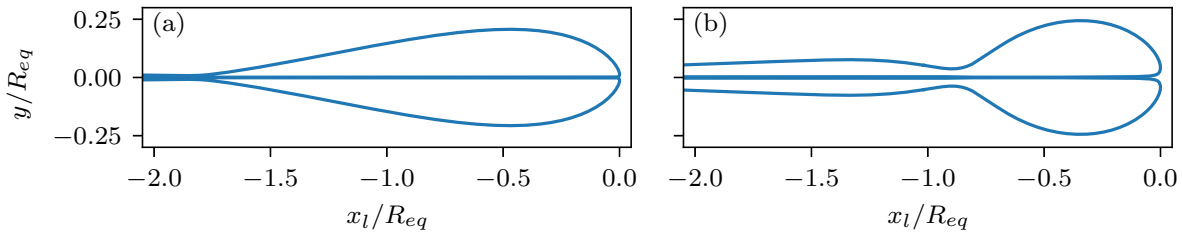

Figure 6.11: Contour snapshots of (a) $\mathcal{E}_r = 0.2$ and (b) $\mathcal{E}_r = 0.6$ at $t = 2$ for the weak axial stretching cases.

for these cases does not do anything as it flattens by the strain flow like a material surface. The rate of flattening for the planar jet regime is much faster than the monopoles under the same strain flow, since monopole self-rotation changes the relative angle of the principal axes with respect to the strain field.

6.3.3 Bi-axial strain field

Under the bi-axial stretching, which induced axial stretching by eliminating the expansion in y-axis to satisfy the continuity condition, the typical head-tail structure is observed for low values of strain-to-vorticity ratio, as shown in Figure 6.11(a). However, for a stronger bi-axial strain flow, the increased axial stretching enhances the leading dipole strength causing it to travel faster than its tail, resulting in separation between the head and tail, as shown in Figure 6.11(b). This is a key signature that can be observed during the reconnection of vortices [39, 107], which can be used to identify the type of strain flow experienced by the vortices.

The dipole will no longer be flattened post-separation, because the stretching effectively lowers the key parameter $\mathcal{E}_r$ exponentially. This is in agreement with the snapshots during vortex reconnection reported by Yao and Hussain [107], where the dipole maintained their post collision. While Yao and Hussain [107] claimed that the core flattening prevent the finite-time singularity during vortex connection, our results have shown that lost of circulation from the leading dipole is merely a transitional event upon the collision. The separation between the tail and head is an indication that $\mathcal{E}_r$ is becoming sufficiently low to prevent further flattening. Then, the lost of circulation to the tail can be accounted by a simple scalar correction at the time of collision, especially considering that the tails in their simulation are much smaller in comparison to the head. Therefore, it is questionable

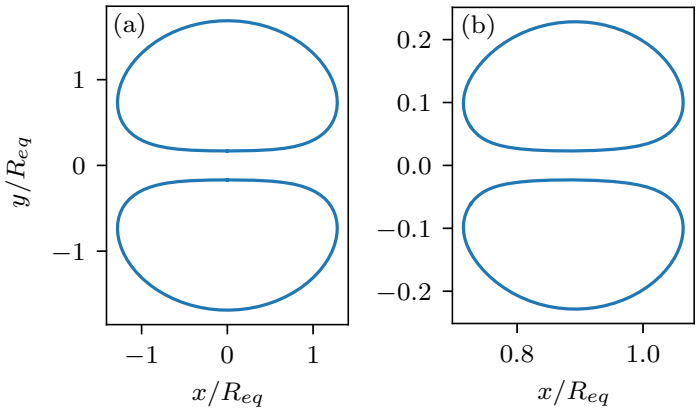

Figure 6.12: Contour snapshots of a vortex dipole in a pure axial stretching strain flow with $\mathcal{E} = 1.0$ at $t = 0$ and $t = 2$.

whether the core flattening play an actual role in the prevention of finite-time singularity considering the separation of the head-tail.

6.3.4 Pure axial strain field

Further increasing the strain flow such that the axial stretching is the only expanding strain. For this case, the dipole cores are finally able to maintain their compactness and remain as vortices, as shown by the contour snapshots in Figure 6.12.

The shape of the contours at $t = 2$ is exactly the same as the initial condition, but at an significantly reduced area due to vortex stretching. The centroid to equivalent radius remains the same as well the entire time. That is, only axial stretching flow is capable of maintaining the integrity of a vortex pair. Relating back to the discussion of finite-time singularity, the validity of the "pyramid" model by Moffatt and Kimura [62] depends on their conjecture that the vortex dipole maintains their asymptote compactness. Such condition can only be possible under the pure axial strain field as shown above, which is true for their assumptions. However, with the inclusion of the curvature induced strain, which mimics a planar type of strain field, the combined strain field (with axial stretching from the pyramid process) is likely something that resembles the bi-axial strain field. Hence, for the "pyramid" model by Moffatt and Kimura [62] to be valid, the $\mathcal{E}_r$ need to be sufficiently high such that stretching can overcomes the flattening to maintain the compactness, which the head-tail separation revealed by Yao and Hussain's simulation [107] is hinting (see our

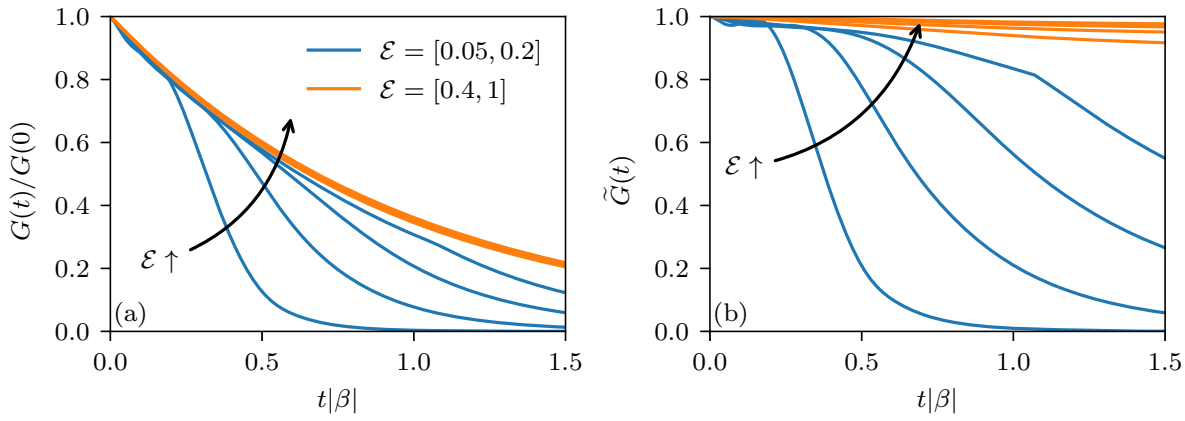

Figure 6.13: Temporal evolution of the (a) gap length $G(t)$ and (b) normalized gap length $\widetilde{G}(t)$ between the vortex patches. The head-tail regimes between $\mathcal{E} = 0.05$ to 0.2 are shown in blue, while the plane jet regimes between $\mathcal{E} = 0.4$ to 1 are shown in orange.

discussion in last sub-section). That is, the Yao and Hussain's results [107] actually aids the model of Moffatt and Kimura [62] instead of disproving it.

6.4 Enhanced mutual attraction

Contrasting the cases of $\mathcal{E} = 0.05$ and $\mathcal{E} = 0.4$ in Figures 6.7 and 6.9 suggests an interesting and counter-intuitive aspect of dipoles in a strain field, namely that a weak strain flow can force the two comprising patches together at a faster rate than can a strong strain field. For the head-tail regime in Figure 6.7(a-c), the gap between the patches closes off from tail to head, whereas the gap for the planar jet regime in Figure 6.9(b) is smaller but still noticeable.

To quantify the patch separation distance we introduce the gap length $G(t)$, defined as the minimum distance between the patches (Figure 6.1), and present it in Figure 6.13(a) for all cases. The cases with $\mathcal{E}$ between 0.05 and 0.2 exhibit a rapid decreases in gap spacing with the smallest values of the strain-to-vorticity ratio showing the most rapid approach of the vortex patches towards one another. On the other hand, the cases between $\mathcal{E} = 0.4$ to 1 still show a decrease in the gap between the patches, but at a slower rate and without any strong dependency on the strain-to-vorticity ratio.

This effect can be isolated from the influence of the strain flow, which also squeezes

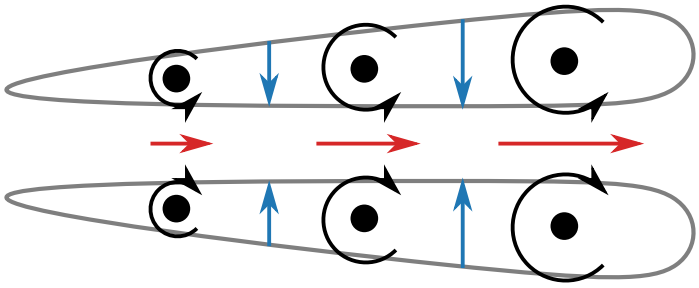

Figure 6.14: Schematic for the explanation of the enhanced mutual attraction between the cores of a strained vortex dipole.

the patches together, again by employing the normalized gap length $\widetilde{G}$, similar to the normalized thickness $\widetilde{T}$, presented in Figure 6.13(b). Under this criterion, a leveled curvature indicates that the gaps are closed under the strain flow exclusively, while any deviation is a sign of other effects at play.

The time series in Figure 6.13(b) for the cases of $\mathcal{E} = 0.05$ to $\mathcal{E} = 0.2$ deviate noticeably from one to zero, indicating that the gap is closed under the added effect of the vorticity. While for cases between $\mathcal{E} = 0.4$ to $\mathcal{E} = 1$, the curves only slightly deviate from unity, demonstrating that the patches are primarily closed under the influence of the strain flow.

As for the vorticity effect that drives the patches together, it is convenient to conclude that the leading dipole induces flow over the extended trailing edge that pushes themselves together. However, the dipole induced pinching flow behind it is a localized effect. Thus, it is difficult to explain the case of $\mathcal{E} = 0.2$ shown in Figure 6.8, which also experiences the added effect of vorticity that pushes the patches together, but without a strong leading dipole. Furthermore, the gap shown in Figure 6.8 decreases relatively uniformly in space, without any localized throat area between the patches that would hint at the role of the leading dipole.

However, we can generalized the leading dipole hypothesis to explain the added vorticity effect that pushes the patches together even without a strong leading dipole, such as the case of the $\mathcal{E} = 0.2$ shown in Figure 6.8. As illustrated by the schematic, the unevenly distributed vorticity (represented by the recirculating symbol) creates an net inward flow to compensate for the accelerating centerline velocity. The net inward flow is the cause of the self-induced motion that pushes the patches together.

In the past section, we have shown that the separation of between the dipole and its tail is an indication that the stretching have overcame the flattening for the leading vortex cores. However, the simulation results of vortex collision from Yao and Hussain

still shows no evidence of finite-time singularity. In Chapter 5, we proposed an alternative mechanism of the parallelization between the colliding vortex tubes as means of pyramid process termination, hence preventing the occurrence of finite-time singularity. The newly discovered mechanism of enhanced mutual attraction between the cores of strain dipole further strengthens our augments for the parallelization as the primary mechanism of finite-time singularity avoidance during vortex collisions.

6.5 Conclusion

In this study, we survey the evolution of a vortex dipole in an external strain flow, which behaves qualitatively and quantitatively different from the well-studied vortex monopole. Under an imposed strain flow, vortex dipoles do not maintain their compactness as a result of each vortex patch preventing the self-rotation of the other. Hence, the deformation is always aligned with the strain flow, resulting in the dipole flattening out indefinitely. By introducing axial stretching, we observed the separation of between leading dipole and its tail; a feature that can be used to identify the type of strain experienced during the collision of vortices.

Chapter 7

Closing Remarks

This thesis has explored some aspects of the vortex-structure and vortex-vortex interactions in idealized scenarios. These scenarios are created by putting vortex rings/dipoles in a control interaction to observe their evolution. A summary and future work suggestions for these topics are listed below.

- In Chapters 3 and 4, the interaction of a vortex with a sharp plate tip was investigation by meanings of collision a vortex ring with an aperture in a wall. A major finding of this work is the direct interaction of a vortex rings with a thin structure tip forces a re-spiraling of the vortex that is reminiscent of the vortex formation. As a result, the colliding vortex ring is able to entrain additional fluid from the aperture surroundings, resulting in a gain of hydrodynamic impulse. Such behaviour appears to be analogous to the jet nozzle, where the exiting jet follows experiences a gain in momentum due to reduction in jet cross-sectional area. But in the case of vortices, the gain in impulse is due to the additional mass captured by the passing vortices.
- In Chapter 5, the stretching mechanism during vortex reconnection was revisited. The results demonstrated that the collision angle between colliding anti-parallel vortices plays a critical role in determining the vortex reconnection properties though vortex stretching manipulation. The result challenges the common belief in the literature that vortex reconnection is only Reynolds number dependent with a constant scaling. Vortex reconnection is known to produce a sharp drop of the near-field pressure and a primary source of noise production [21]. Our results here open the door to mitigate some of the negatives of vortex reconnection by means of geometry manipulation of large scale vortical structures, which should be the next step of this investigation.

- In Chapter 6, the evolution of a strained dipole is examined. It was found that the pair of two vortex cores prevent the realignment of vortex cores with respect to the background strain field. As a result, the vortex cores are incapable of maintaining their compactness. For a low strength strain field relative to vorticity density, the cores are "flattened" by means of vorticity ejection to its wake (head-tail regime), while a strong strain flow can flatten a dipole like a simple material contour. Lastly, it was discovered that the core deformation creates a mutual attraction that closes the gap between an initial separated dipole cores. It is possible that the "parallelization" mechanism discussed in Chapter 5 is a result of such mutual attraction, and should be validation through numerical simulation next.

7.1 Future work suggestions

- An extension to the aperture-ring interaction study is to generalize the fluid entrainment phenomenon of passing vortices in a realistic flow condition, where the axisymmetrical condition no longer holds. Particularly, a deformable plate interacting with a vortex with a core size on the same order of the plate width, such that strong edge effects might disrupt the "vortex nozzle" effect. If "vortex nozzle" is robust to such three-dimensional disturbance, fluid entrainment from ambient vortices as a means of impulse gain could be an energy saving strategy for aquatic animals.

- A variation of the aperture-ring interaction study is the collision of a vortex ring with a disk instead of an aperture, where the structural tip is aligned in the opposite direction with respect to the vortex induced flow in comparison with the aperture counter-part. Such configuration is yet to be examined in this thesis or literature. A key area of interest is to find the critical radius ratio where the colliding vortex ring transitions from blockage (because of vortex rebound) to escape (pass around a small disk). This information could provide valuable insights into a jellyfish's ability to capture its own vortex ring to enhance its propulsion efficiency [29].

- For the angle of vortex collision, the next step is to increase the Reynolds number such that instability takes place. As demonstrated by the results in Chapter 5, the collision angle determines the degrees of parallel stretching and core flattening. At a low angle, the prominence of parallel stretching produces strong reconnection threads that are sensitive to elliptical wave instabilities [56]; while at high angles, strong core flattening was observed, which is sensitive to the development of Kelvin Helmholtz instability [55]. Therefore, I hypothesize that collision angle will also alter

the Reynolds number scaling at high Reynolds numbers because of the differences in instability mechanisms.

- For the flattening of vortex cores during vortex collision, the contour dynamics study has demonstrated that the pairing of colliding vortices results in the formation of the head-tail structure. As such, the rate of vorticity ejection in the wake depends on the strain-to-vorticity ratio. To prove definitively that core flattening plays a role in the regularization of finite-time singularity during vortex collision, a model that predicts the applied strain from local curvature needs to be developed.

References

[1] S. Alben. The attraction between a flexible filament and a point vortex. *Journal of Fluid Mechanics*, 697:481–503, 2012.

[2] J. J. Allen, Y. Jouanne, and B. N. Shashikanth. Vortex interaction with a moving sphere. *Journal of Fluid Mechanics*, 587:337–346, 2007.

[3] J. J. Allen and T. Naitoh. Experimental study of the production of vortex rings using a variable diameter orifice. *Physics of Fluids*, 17:061701, 2005.

[4] P. J. Archer, T. G. Thomas, and G. N. Coleman. The instability of a vortex ring impinging on a free surface. *Journal of Fluid Mechanics*, 642:79–94, 2010.

[5] J. Barkley Rosser. Nine-point difference solutions for Poisson's equation. *Computers & Mathematics with Applications*, 1:351–360, 1975.

[6] G. Beardsell, L. Dufresne, and G. Dumas. Investigation of the viscous reconnection phenomenon of two vortex tubes through spectral simulations. *Physics of Fluids*, 28:095103, 2016.

[7] O. N. Boratav, R. B. Pelz, and N. J. Zabusky. Reconnection in orthogonally interacting vortex tubes: Direct numerical simulations and quantifications. *Physics of Fluids A: Fluid Dynamics*, 4:581–605, 1992.

[8] M. P. Brenner, S. Hormoz, and A. Pumir. Potential singularity mechanism for the Euler equations. *Physical Review Fluids*, 1:084503, 2016.

[9] T. Brooke Benjamin. The alliance of practical and analytical insights into the nonlinear problems of fluid mechanics. In P. Germain and B. Nayroles, editors, *Applications of Methods of Functional Analysis to Problems in Mechanics. Lecture Notes in Mathematics*, volume 503, pages 8–29. Springer, Berlin, Heidelberg, 1976.

[10] D. Buaria, E. Bodenschatz, and A. Pumir. Vortex stretching and enstrophy production in high Reynolds number turbulence. *Physical Review Fluids*, 5(10):104602, 2020.

[11] J. D. Buntine and D. I. Pullin. Merger and cancellation of strained vortices. *Journal of Fluid Mechanics*, 205:263–295, 1989.

[12] J. M. Burgers. A Mathematical Model Illustrating the Theory of Turbulence. In R. Von Mises and T. Von Karman, editors, *Advances in Applied Mechanics*, volume 1, pages 171–199. Academic Press, New York, 1948.

[13] M. D. Bustamante and R. M. Kerr. 3D Euler about a 2D symmetry plane. *Physica D*, 237:1912–1920, 2008.

[14] B. J. Cantwell. Viscous starting jets. *Journal of Fluid Mechanics*, 173:159–189, 1986.

[15] C. Canuto, M. Y. Hussaini, A. Quarteroni, and T. A. Zang. *Spectral Methods in Fluid Dynamics*. Springer Berlin Heidelberg, Berlin, Heidelberg, 1988.

[16] M. Cheng, J. Lou, and L. S. Luo. Numerical study of a vortex ring impacting a flat wall. *Journal of Fluid Mechanics*, 660:430–455, 2010.

[17] C. C. Chu, C. T. Wang, and C. C. Chang. A vortex ring impinging on a solid plane surface - vortex structure and surface force. *Physics of Fluids*, 7:1391–1401, 1995.

[18] C. C. Chu, C. T. Wang, C. C. Chang, R. Y. Chang, and W. T. Chang. Head-on collision of two coaxial vortex rings: experiment and computation. *Journal of Fluid Mechanics*, 296:39–71, 1995.

[19] J. O. Dabiri. Note on the induced Lagrangian drift and added-mass of a vortex. *Journal of Fluid Mechanics*, 547:105–113, 2006.

[20] J. O. Dabiri and M. Gharib. Fluid entrainment by isolated vortex rings. *Journal of Fluid Mechanics*, 511:311–331, 2004.

[21] H. Daryan, F. Hussain, and J. P. Hickey. Aeroacoustic noise generation due to vortex reconnection. *Physical Review Fluids*, 5(6):062702, 2020.

[22] A. T. A. M. de Waele and R. G. K. M. Aarts. Route to vortex reconnection. *Physical Review Letters*, 72(4):482–485, 1994.

[23] I. Delbende and M. Rossi. The dynamics of a viscous vortex dipole. *Physics of Fluids*, 21:073605, 2009.

[24] N. Didden. On the formation of vortex rings: rolling-up and production of circulation. *Journal of Applied Mathematics and Physics*, 30:101–116, 1979.

[25] D. G. Dritschel. The nonlinear evolution of rotating configurations of uniform vorticity. *Journal of Fluid Mechanics*, 172:157–182, 1986.

[26] Brenden Epps. Review of Vortex Identification Methods. In *55th AIAA Aerospace Sciences Meeting*, Reston, Virginia, 1 2017. American Institute of Aeronautics and Astronautics.

[27] A. Etebari and P. P. Vlachos. Improvements on the accuracy of derivative estimation from DPIV velocity measurements. *Experiments in Fluids*, 39:1040–1050, 2005.

[28] L. E. Fraenkel. Examples of steady vortex rings of small cross-section in an ideal fluid. *Journal of Fluid Mechanics*, 51:119–135, 1972.

[29] B. J. Gemmell, K. T. Du Clos, S. P. Colin, K. R. Sutherland, and J. H. Costello. The most efficient metazoan swimmer creates a 'virtual wall' to enhance performance. *Proceedings of the Royal Society B: Biological Sciences*, 288:20202494, 1 2021.

[30] C. Geuzaine and J.-F. Remacle. Gmsh: A 3-D finite element mesh generator with built-in pre- and post-processing facilities. *International Journal for Numerical Methods in Engineering*, 79:1309–1331, 2009.

[31] M. Gharib, E. Rambod, and K. Shariff. A universal time scale for vortex ring formation. *Journal of Fluid Mechanics*, 360:121–140, 1998.

[32] S. Goto, Y. Saito, and G. Kawahara. Hierarchy of antiparallel vortex tubes in spatially periodic turbulence at high Reynolds numbers. *Physical Review Fluids*, 2:064603, 2017.

[33] R. S. Heeg and N. Riley. Simulations of the formation of an axisymmetric vortex ring. *Journal of Fluid Mechanics*, 339:199–211, 5 1997.

[34] R. H. Hernández and E. Monsalve. Experimental observation of the collision of three vortex rings. *Fluid Dynamics Research*, 47:035513, 2015.

[35] S. Hormoz and M. P. Brenner. Absence of singular stretching of interacting vortex filaments. *Journal of Fluid Mechanics*, 707:191–204, 2012.

[36] J. Hu, Y. Cha, M. Porfiri, and S. D. Peterson. Energy harvesting from a vortex ring impinging on an annular ionic polymer metal composite. *Smart Materials and Structures*, 23:074014, 2014.

[37] J. Hu and S. D. Peterson. Vortex ring impingement on a wall with a coaxial aperture. *Physical Review Fluids*, 3:084701, 2018.

[38] J Hu and S. D. Peterson. Hydrodynamic impulse enhancement of a vortex ring interacting with an axisymmetric co-axial aperture. *Journal of Fluid Mechanics*, 917:A34, 2021.

[39] F. Hussain and K. Duraisamy. Mechanics of viscous vortex reconnection. *Physics of Fluids*, 23:021701, 2011.

[40] P. A. Jacobs and D. I. Pullin. Coalescence of stretching vortices. *Physics of Fluids*, 28(6):1619–1625, 1985.

[41] J. Jeong and F. Hussain. On the identification of a vortex. *Journal of Fluid Mechanics*, 285:69, 1995.

[42] R. M. Kerr and F. Hussain. Simulation of vortex reconnection. *Physica D: Nonlinear Phenomena*, 37, 1989.

[43] S. Kida. Motion of an elliptic vortex in a uniform shear flow. *Journal of the Physical Society of Japan*, 50(10):3517–3520, 1981.

[44] S. Kida and H. Miura. Identification and analysis of vortical structures. *European Journal of Mechanics - B/Fluids*, 17:471–488, 1998.

[45] S. Kida and M. Takaoka. Vortex Reconnection. *Annual Review of Fluid Mechanics*, 26:169–189, 1994.

[46] S. Kida, M. Takaoka, and F. Hussain. Collision of two vortex rings. *Journal of Fluid Mechanics*, 230:583–646, 1991.

[47] S. Kida, M. Takaoka, and F. Hussein. Reconnection of two vortex rings. *Physics of Fluids A: Fluid Dynamics*, 1:630–632, 1989.

[48] D. Kim and M. Gharib. Characteristics of vortex formation and thrust performance in drag-based paddling propulsion. *Journal of Experimental Biology*, 214:2283–2291, 2011.

[49] D. Kleckner and W. T. M. Irvine. Creation and dynamics of knotted vortices. *Nature Physics*, 9(4):253–258, 2013.

[50] D. Kuchemann. Report on the I.U.T.A.M. symposium on concentrated vortex motions in fluids. *Journal of Fluid Mechanics*, 21:1–20, 1965.

[51] T. T. Lim. A note on the leapfrogging between two coaxial vortex rings at low Reynolds numbers. *Physics of Fluids*, 9:239–241, 1997.

[52] N. Masuda, J. Yoshida, B. Ito, T. Furuya, and O. Sano. Collision of a vortex ring on granular material. Part I. Interaction of the vortex ring with the granular layer. *Fluid Dynamics Research*, 44:015501, 2012.

[53] P. McGavin and D. I. Pontin. Vortex line topology during vortex tube reconnection. *Physical Review Fluids*, 3:054701, 2018.

[54] P. McGavin and D. I. Pontin. Reconnection of vortex tubes with axial flow. *Physical Review Fluids*, 4:024701, 2019.

[55] R. McKeown, R. Ostilla-Mónico, A. Pumir, M. P. Brenner, and S. M. Rubinstein. Cascade leading to the emergence of small structures in vortex ring collisions. *Physical Review Fluids*, 3:124702, 2018.

[56] R. McKeown, R. Ostilla-Mónico, A. Pumir, M. P. Brenner, and S. M. Rubinstein. Turbulence generation through an iterative cascade of the elliptical instability. *Science Advances*, 6(9):eaaz2717, 2020.

[57] M. V. Melander and F. Hussain. Cross-linking of two antiparallel vortex tubes. *Physics of Fluids A: Fluid Dynamics*, 1:633–636, 1989.

[58] V. V. Meleshko and G. J. F. van Heijst. On Chaplygin's investigations of two-dimensional vortex structures in an inviscid fluid. *Journal of Fluid Mechanics*, 272:157–182, 1994.

[59] T. Miloh and D. J. Shlien. Passage of a vortex ring through a circular aperture in an infinite-plane. *Physics of Fluids*, 20:1219–1227, 1977.

[60] T. B. Mithchell and L. F. Rossi. The evolution of Kirchhoff elliptic vortices. *Physics of Fluids*, 20(5):054103, 2008.

[61] H. K. Moffatt, S. Kida, and K. Ohkitani. Stretched vortices - the sinews of turbulence; large-Reynolds-number asymptotics. *Journal of Fluid Mechanics*, 259:241–264, 1994.

[62] H. K. Moffatt and Y. Kimura. Towards a finite-time singularity of the Navier-Stokes equations Part 1. Derivation and analysis of dynamical system. *Journal of Fluid Mechanics*, 861:930–967, 2019.

[63] H. K. Moffatt and Y. Kimura. Towards a finite-time singularity of the Navier-Stokes equations. Part 2. Vortex reconnection and singularity evasion. *Journal of Fluid Mechanics*, 870:R1, 2019.

[64] K. Mohseni and M. Gharib. A model for universal time scale of vortex ring formation. *Physics of Fluids*, 10:2436–2438, 1998.

[65] K. Mohseni, H. Ran, and T. Colonius. Numerical experiments on vortex ring formation. *Journal of Fluid Mechanics*, 430:267–282, 2001.

[66] M Mortensen and H. P. Langtangen. High performance Python for direct numerical simulations of turbulent flows. *Computer Physics Communications*, 203:53–65, 2016.

[67] B. R. Morton. The generation and decay of vorticity. *Geophysical and Astrophysical Fluid Dynamics*, 28:277–308, 1984.

[68] Y. Motoori and S. Goto. Generation mechanism of a hierarchy of vortices in a turbulent boundary layer. *Journal of Fluid Mechanics*, 865:1085–1109, 2019.

[69] C. Naaktgeboren, P. S. Krueger, and J. L. Lage. Interaction of a laminar vortex ring with a thin permeable screen. *Journal of Fluid Mechanics*, 707:260–286, 2012.

[70] J. C. Neu. The dynamics of a columnar vortex in an imposed strain. *Physics of Fluids*, 27(10):2397–2402, 1984.

[71] D. T. H. New and S. C. M. Yu. *Vortex rings and jets: recent developments in near-field dynamics*. Springer, Singapore, 2015.

[72] T. H. New, J. Long, B. Zang, and S. Shi. Collision of vortex rings upon V-walls. *Journal of Fluid Mechanics*, 899:A2, 2020.

[73] T. H. New and B. Zang. Head-on collisions of vortex rings upon round cylinders. *Journal of Fluid Mechanics*, 833:648–676, 2017.

[74] Q. Ni, F. Hussain, J. Wang, and S. Chen. Analysis of Reynolds number scaling for viscous vortex reconnection. *Physics of Fluids*, 24:105102, 2012.

[75] M. Nitsche. Deflection and trapping of a counter-rotating vortex pair by a flat plate. *Physical Review Fluids*, 2:1–22, 2017.

[76] J. Norbury. A family of steady vortex rings. *Journal of Fluid Mechanics*, 57(3):417–431, 1973.

[77] C. O'Farrell and J. O. Dabiri. Pinch-off of non-axisymmetric vortex rings. *Journal of Fluid Mechanics*, 740:61–96, 2014.

[78] J. Olsthoorn and S. B. Dalziel. Three-dimensional visualization of the interaction of a vortex ring with a stratified interface. *Journal of Fluid Mechanics*, 820:549–579, 2017.

[79] J. Olsthoorn and S. B. Dalziel. Vortex-ring-induced stratified mixing: Mixing model. *Journal of Fluid Mechanics*, 837:129–146, 2018.

[80] P. Orlandi. Vortex dipole rebound from a wall. *Physics of Fluids A: Fluid Dynamics*, 2:1429–1436, 1990.

[81] P. Orlandi and R. Verzicco. Vortex rings impinging on walls: axisymmetric and three-dimensional simulations. *Journal of Fluid Mechanics*, 256:615–646, 1993.

[82] S. D. Peterson and M. Porfiri. Interaction of a vortex pair with a flexible plate in an ideal quiescent fluid. *Journal of Intelligent Material Systems and Structures*, 23:1485–1504, 2012.

[83] S. D. Peterson and M. Porfiri. Impact of a vortex dipole with a semi-infinite rigid plate. *Physics of Fluids*, 25:093103, 2013.

[84] R. T. Pierrehumbert. A family of steady, translating vortex pairs with distributed vorticity. *Journal of Fluid Mechanics*, 99:129–144, 1980.

[85] A. Pirnia, J. Hu, S. D. Peterson, and B. D. Erath. Vortex dynamics and flow-induced vibrations arising from a vortex ring passing tangentially over a flexible plate. *Journal of Applied Physics*, 122:164901, 2017.

[86] A. Pumir and R. M. Kerr. Numerical simulation of interacting vortex tubes. *Physical Review Letters*, 58(16):1636–1639, 1987.

[87] M. Raffel, C. E. Willert, S. T. Wereley, and J. Kompenhans. *Particle image velocimetry: a practical guide*. Springer, Berlin Heidelberg New York, 2 edition, 2007.

[88] M. Rosenfeld, E. Rambod, and M. Gharib. Circulation and formation number of laminar vortex rings. *Journal of Fluid Mechanics*, 376:297–318, 1998.

[89] P. G. Saffman. The velocity of viscous vortex rings. *Studies in Applied Mathematics*, 49:371–380, 1970.

[90] P. G. Saffman. *Vortex Dynamics*. Cambridge University Press, Cambridge, UK, 1993.

[91] P. G. Saffman and S. Tanveer. The touching pair of equal and opposite uniform vortices. *Physics of Fluids*, 25:1929–1930, 1982.

[92] J. Satti and J. Peng. Leapfrogging of two thick-cored vortex rings. *Fluid Dynamics Research*, 45:035503, 2013.

[93] M. Shusser and M. Gharib. Energy and velocity of a forming vortex ring. *Physics of Fluids*, 12:618–621, 2000.

[94] I. S. Sullivan, J. J. Niemela, R. E. Hershberger, D. Bolster, and R. J. Donnelly. Dynamics of thin vortex rings. *Journal of Fluid Mechanics*, 609:319–347, 2008.

[95] J. D. Swearingen, J. D. Crouch, and R. A. Handler. Dynamics and stability of a vortex ring impacting a solid boundary. *Journal of Fluid Mechanics*, 297:1–28, 1995.

[96] A. Tinaikar, S. Advaith, and S. Basu. Understanding evolution of vortex rings in viscous fluids. *Journal of Fluid Mechanics*, 836:873–909, 2018.

[97] L. N Trefethen. *Spectral Methods in MATLAB*. SIAM, Philadelphia, 2000.

[98] R. R. Trieling, J. M.A. Van Wesenbeeck, and G. J.F. Van Heijst. Dipolar vortices in a strain flow. *Physics of Fluids*, 10:144–159, 1998.

[99] R. Verzicco and P. Orlandi. Normal and oblique collisions of a vortex ring with a wall. *Meccanica*, 29:383–391, 1994.

[100] H. Vollmers. Detection of vortices and quantitative evaluation of their main parameters from experimental velocity data. *Measurement Science and Technology*, 12:1199–1207, 2001.

[101] J. D. A. Walker, C. R. Smith, A. W. Cerra, and T. L. Doligalski. The impact of a vortex ring on a wall. *Journal of Fluid Mechanics*, 181:99–140, 1987.

[102] J. H. Williamson. Low-storage Runge-Kutta schemes. *Journal of Computational Physics*, 35:48–56, 1980.

[103] J. Z. Wu, H. Y. Ma, and M. D. Zhou. *Vorticity and Vortex Dynamics*. Springer-Verlag, Berlin, Heidelberg, New York, 2006.

[104] J. Z. Wu, H. Y. Ma, and M. D. Zhou. *Vortical flows*. Springer, Berlin, 2015.

[105] Y. Xu, J. J. Wang, L. H. Feng, G. S. He, and Z. Y. Wang. Laminar vortex rings impinging onto porous walls with a constant porosity. *Journal of Fluid Mechanics*, 837:729–764, 2018.

[106] J. Yao and F. Hussain. A physical model of turbulence cascade via vortex reconnection sequence and avalanche. *Journal of Fluid Mechanics*, 883:A51, 2020.

[107] J. Yao and F. Hussain. On singularity formation via viscous vortex reconnection. *Journal of Fluid Mechanics*, 888:R2, 2020.

[108] J. Yao and F. Hussain. Separation scaling for viscous vortex reconnection. *Journal of Fluid Mechanics*, 900:R4, 2020.

[109] N. J. Zabusky, O. N. Boratav, R. B. Pelz, M. Gao, D. Silver, and S. P. Cooper. Emergence of coherent patterns of vortex stretching during reconnection: A scattering paradigm. *Physical Review Letters*, 67(18):2469–2472, 1991.

[110] N. J. Zabusky, M. H. Hughes, and K. V. Roberts. Contour dynamics for the Euler equations in two dimensions. *Journal of Computational Physics*, 30:96–106, 1979.

[111] N. J. Zabusky and M. V. Melander. Three-dimensional vortex tube reconnection: Morphology for orthogonally-offset tubes. *Physica D: Nonlinear Phenomena*, 37:555–562, 1989.

[112] E. Zivkov, S. Yarusevych, M. Porfiri, and S. D. Peterson. Numerical investigation of the interaction of a vortex dipole with a deformable plate. *Journal of Fluids and Structures*, 58:203–215, 2015.

APPENDICES

Appendix A

Full expressions for the analytical model of the ring-aperture interaction

The full expressions of the terms in Equation (3.6) in Chapter 3 are

$$\phi_v(x,r) = -\frac{\Gamma_1 R_1}{2}\int_0^\infty e^{k(\xi-x)} J_0(kr) J_1(kR_1)\ \mathrm{d}k \tag{A.1a}$$

$$\phi_w(x,r) = -\frac{\Gamma_1 R_1}{2}\int_0^\infty e^{k(\xi+x)} J_0(kr) J_1(kR_1)\ \mathrm{d}k \tag{A.1b}$$

$$\phi_a(x,r) = \frac{\Gamma_1 R_1}{\pi}\int_0^\infty\int_0^\infty\int_0^{R_a} e^{k\xi+\lambda x} J_0(kr) J_1(kR_1) \cos(ks)\cos(\lambda s)\ \mathrm{d}s\ \mathrm{d}\lambda\ \mathrm{d}k \tag{A.1c}$$

where $J_m(\cdot)$ denotes the Bessel function of order m. The closed form expressions for the wall induced velocity component U_w and V_w are

$$U_w(\xi, R_1) = \frac{\Gamma_1 \eta}{4\pi R_1}[\mathcal{K}(\eta^2) - \mathcal{I}(\eta^2)] \tag{A.2a}$$

$$V_w(\xi, R_1) = \frac{\Gamma_1 \eta \xi}{4\pi {R_1}^2}\left[2\mathcal{K}(\eta^2) - \left(2 + {R_1}^2/\xi^2\right)\mathcal{K}(\eta^2)\right] \tag{A.2b}$$

where $\mathcal{K}(\cdot)$ and $\mathcal{I}(\cdot)$ are the complete elliptic integral of the first and second kind, and η is

$$\eta(\xi, R_1) = \frac{R_1}{\sqrt{{R_1}^2 + \xi^2}} \tag{A.2c}$$

The aperture induced velocity component U_a and V_a for the incoming vortex ring are

$$\begin{aligned} U_a(\xi, R_1) = \frac{\Gamma_1}{8\pi}\Bigg\{ & 8\sin\left(\frac{\sigma}{2}\right)\left[({R_1}^2 + \xi^2 - {R_a}^2) + 4\xi^2{R_a}^2\right]^{-\frac{1}{4}} \\ & - \frac{1}{\xi}\left[(1+\mu^2)\sin(\sigma) - \frac{(1-\mu^2)}{2}\sin(2\sigma)\right] \\ & + \frac{\mu}{\xi}\Big[\mathcal{F}\left(\sigma + \frac{\pi}{2}, \eta^2\right) - \mathcal{F}\left(\frac{\pi}{2}, \eta^2\right) \\ & + \mathcal{H}\left(\frac{\pi}{2}, \eta^2\right) - \mathcal{H}\left(\sigma + \frac{\pi}{2}, \eta^2\right)\Big] \\ & - \frac{\mu^2}{\xi}\left[1 + \frac{{R_1}^2}{\xi^2}\sin^2(\sigma)\right]^{\frac{1}{2}}\sin(\sigma) \\ & - \frac{1}{R_1}\ln\left[\frac{R_1}{\xi}\sin(\sigma) + \left(1 + \frac{{R_1}^2}{\xi^2}\sin^2(\sigma)\right)^{\frac{1}{2}}\right]\Bigg\} \end{aligned} \tag{A.3a}$$

$$\begin{aligned} V_a(\xi, R_1) = -\frac{\Gamma_1}{8\pi R_1}\Bigg\{ & 8\left[R_1\cos\left(\frac{\sigma}{2}\right) + \xi\sin\left(\frac{\sigma}{2}\right)\right] \\ & \left[({R_1}^2 + \xi^2 - {R_a}^2)^2 + 4\xi^2{R_a}^2\right]^{-\frac{1}{4}} \\ & + \eta^2\left[\sin(\sigma) + \frac{\sin(2\sigma)}{2}\right] \\ & + 2\mu\left[\mathcal{F}\left(\sigma + \frac{\pi}{2}, \eta^2\right) - \mathcal{F}\left(\frac{\pi}{2}, \eta^2\right)\right] \\ & - \frac{1+\mu^2}{\mu}\left[\mathcal{H}\left(\sigma + \frac{\pi}{2}, \eta^2\right) - \mathcal{H}\left(\frac{\pi}{2}, \eta^2\right)\right] \\ & + \eta^2\left[1 + \frac{{R_1}^2}{\xi^2}\sin^2(\sigma)\right]^{\frac{1}{2}}\sin(\sigma)\Bigg\} \end{aligned} \tag{A.3b}$$

where $\mathcal{F}(\cdot,\cdot)$ and $\mathcal{H}(\cdot,\cdot)$ are the incomplete elliptic integral of the first and second kind, and μ is

$$\mu(\xi, R_1) = \frac{\xi}{\sqrt{{R_1}^2 + \xi^2}}. \tag{A.3c}$$

Appendix B

Experiment comparison for the collision of three vortex rings

Figure B.1 illustrates the vorticity isosurfaces for the three ring case for comparison with the experimental flow visualizations in Ref. [34]. From the top view in Figure B.1(a), the vortex rings deform into a triangle shape upon contact. Subsequently, the reconnection threads expand outward due to mutual induction, forming a three-pointed star-like shape in Figure B.1(b). Eventually, the reconnection threads dissipate, leaving behind two highly distorted vortex rings. Our simulations did not capture any asymmetry disturbances that can be seen from the experimental results. However, we do not enforce any actual symmetry between the colliding vortex rings (just a set of symmetrically aligned identical vortex rings for the initial condition), thus we believe that the asymmetrical disturbances observed in experiments is a result of slight experimental imperfections. Overall, our simulation results captured all stages of the interaction observed in the experiment with excellent resemblance.

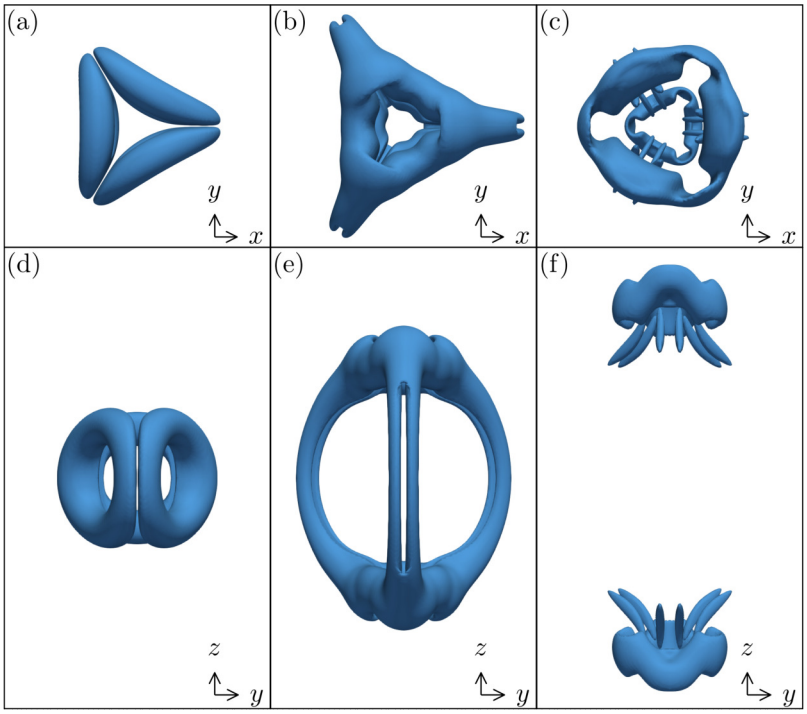

Figure B.1: Vorticity isosurfaces of $|\boldsymbol{\omega}| = 0.5$ at (a,d) $t = 6.25$, (b,e) 18.75, and (c,f) 31.25 for three vortex ring collision at Re = 500. Top and side views are shown in (a,b,c) and (d,e,f), respectively.

Appendix C

Validation of the contour dynamics algorithm

We compare our numerical contour dynamics results with three classical problems in the literature. We first compare our strain monopole numerical results with the analytical solutions from Equation (6.4) to check the accuracy of axial stretching implementation. A sample comparison with the initial conditions of $R_b/R_a = 0.5$ and $\theta = 0°$ in a weak axial strain field (see Table 6.1) of $\mathcal{E} = 0.1$ is shown in Figure C.1. The time series of the aspect

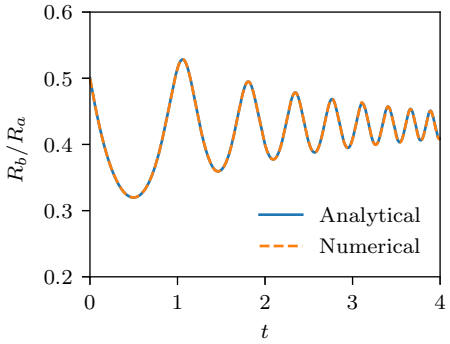

Figure C.1: Aspect ratio R_b/R_a comparison between the analytical and numerical results for a vortex monopole in a weak axial strain field of $\mathcal{E} = 0.1$.

ratio are identical between the analytical and our numerical results.

Then, we simulate the evolution of a perturbed Kirchhoff elliptical vortex [25, 60]. Particularly, a Kirchhoff vortex under an $m = 4$ perturbation generates a tail-like feature

that somewhat resembles to a dipole tail, and we wish to check if our code can produce the phenomenon accurately. The numerical results of a Kirchhoff vortex with an aspect ratio of 6 : 1, a vorticity density of $\Omega = 1$, and a $m = 4$ perturbation magnitude of 0.02 are shown in Figure C.2, which captures the double spiraling tails as expected.

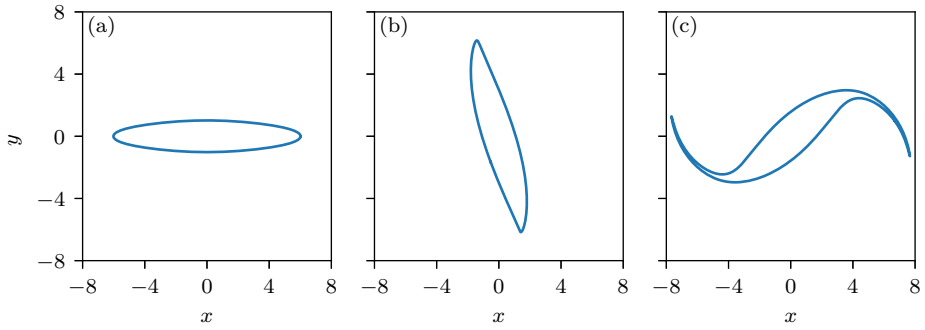

Figure C.2: Evolution of a Kirchhoff elliptical vortex with an aspect ratio of 6 : 1 and $m = 4$ perturbation. Snapshots from $t = 0$, 15, and 30 are shown from (a) to (c), respectively.

Lastly, we simulate the coalescence of two same-signed vortices to check if our codes can capture the interaction between two separated vortex patches in close proximity. Figure C.3 illustrates the results of two equal vortices with radius of $R = 1$, vorticity density of $\Omega = 1$, and separated by $3.5R$ between their centers. Our code captures the documented behaviour

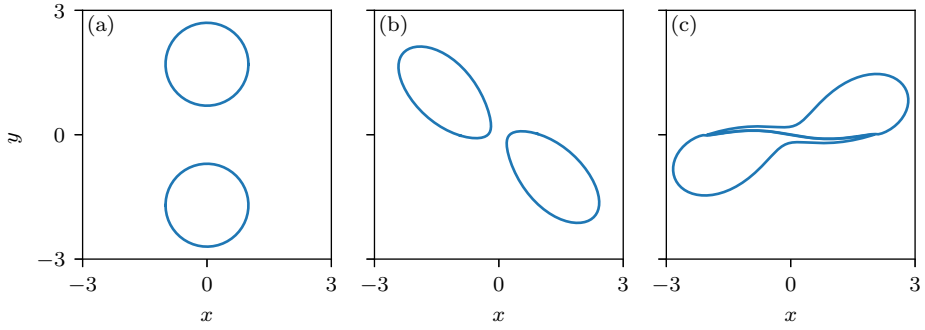

Figure C.3: Coalescence of same signed circular vortices with radius of $R = 1$ and separated by $3.5R$. Snapshots from $t = 0$, 10, and 20 are shown from (a) to (c), respectively.

in the literature, where the circular vortices are deformed into comma-like shapes as they merge in Figure C.3(c).